UNIVERSITY OF CALIFORNIA
SANTA CRUZ

THE STRUCTURE OF EVAPORATING BLACK HOLES

A dissertation submitted in partial satisfaction of the
requirements for the degree of

DOCTOR OF PHILOSOPHY

in

PHYSICS

by

Joseph Caulfield Schindler

September 2019

The Dissertation of Joseph Caulfield Schindler
is approved:

Professor Anthony Aguirre, Chair

Professor Howard Haber

Professor Michael Dine

Quentin Williams
Acting Vice Provost and Dean of Graduate Studies

Contents

List of Figures

Abstract

The structure of evaporating black holes

by

Joseph Caulfield Schindler

A detailed model is constructed for the spacetime of an evaporating black hole. This model is used to analyze some persistent questions about black hole spacetimes in general, and to discuss the mechanism of Hawking radiation. The self-consistency of the model is studied and used to illuminate some general principles in semiclassical gravity. Along the way, a unified analysis is provided for the class of "strongly spherically symmetric" spacetimes, and a method for constructing a broad class of explicit Penrose diagrams is obtained.

Acknowledgments

I am hugely grateful to my advisor Anthony Aguirre, for his support, open-mindedness, and ability to direct our focus to the most important questions. Thank you for listening to ideas ranging from good to strange, and for encouraging me to pursue research directions which some might have dismissed.

To my research group: Dominik, Amita, Ross — thank you for the many interesting discussions. The same to Cam, Mike, and Christoph, and to the many other students and faculty I've had the pleasure of interacting with at UCSC.

Thanks to the many great teachers I have had at UCSC, from whom I have learned so much. Especially Howie, whose commitment to teaching a rigorous course is unrivaled, and to George Brown, who managed to teach me a lot without ever instructing a course I took. And finally, thanks to my former advisor Fred Ellis, who taught me how to do physics in the first place.

The text of this dissertation includes reprints of the following previously published material:

- J. C. Schindler and A. Aguirre. Algorithms for the explicit computation of Penrose diagrams. *Class. Quant. Grav.*, 35(10):105019, 2018, 1802.02263.
- Joseph C. Schindler, Anthony Aguirre, and Amita Kuttner. Understanding black hole evaporation using explicitly computed Penrose diagrams. 2019, 1907.04879.

These publications are used with permission of all co-authors. The co-author A Aguirre listed in these publications directed and supervised the research which forms the basis for the dissertation. Both articles were written by J Schindler, and the research supporting both publications was conducted by J Schindler.

Chapter 1

Introduction

Black holes are common astrophysical objects, characterized by their strong gravitational field and extreme density. Recently, their existence has been confirmed by increasingly direct observations [3, 4]. But despite their being common from an observational perspective, a number of surprisingly basic theoretical and practical questions about black holes remain open to debate. For instance:

- What is the proper definition of "black hole" within general relativity?
- How should we model the spacetime structure of an evolving black hole?
- In such a model, where is the physically meaningful "horizon"?
- What happens inside a black hole? Is there any strange physics at the horizon? Can the process of black hole evaporation be understood locally? Does evaporation lead to a loss of information? And more ...

These and related questions often have textbook answers based on oversimplified considerations — namely, based on analysis of the Schwarzschild spacetime, which represents a static and eternal black hole with unperturbed spherical

symmetry and a central singularity. But when more complicated dynamics are accounted for, the standard explanations break down.

For instance, if a black hole is in theory allowed to accrete additional mass, then the globally defined "event horizon" (a black hole's most popular "horizon") has a location determined by events in the far future, and cannot be physically meaningful. Alternately, if spherical symmetry is perturbed (say by an orbiting accretion disk), then the location of the locally defined "apparent horizon" becomes ambiguous and impossible to asses. And if gravitational physics is assumed to be regulated by a Planck scale curvature cutoff, the global structure of a black hole spacetime can be drastically changed. Even the inclusion of charge and spin is enough to disrupt some of the more fragile common arguments.

Even more pernicious is the necessity of including the Hawking radiation [5] and its gravitational backreaction. This presents a difficult problem, since the phenomenon is fundamentally a quantum effect in curved spacetime. One point of view is that a full resolution can only emerge in quantum gravity, and that attempts to fully describe the evaporation in a semiclassical treatment are doomed. It's possible that this is true, but nonetheless, almost all discussions of black hole evaporation rely in some way on assumptions about a classical spacetime. Many such discussions rely on oversimplified spacetime models, which, similar to the other cases listed above, can lead to misconceptions about basic concepts.

The main point of this thesis is to analyze a more detailed, and more self-consistent, model of an evaporating black hole than has previously been considered. A major tool in this analysis (and indeed in almost every analysis of black hole structure) is a type of "causal" spacetime diagram called a "Penrose diagram." Along the way, a method for generating such diagrams is described, which greatly increases the class of explicitly known Penrose diagrams. Once the tools

are developed and the model is defined, these diagrams are used to undertake a broad discussion of the physics of evaporating black holes.

The text consists of two main chapters, each based on a published article. The second chapter, "Algorithms for the explicit computation of Penrose diagrams," is based on Reference [1], which was published in 2018. The third chapter, "Understanding black hole evaporation using explicitly computed Penrose diagrams," is based on Reference [2], which is currently in review for publication.

The first of these two articles provides an introduction to the fundamental concepts and methods applied in the second. Specifically, a broad class of spacetimes is constructed which includes a class of evaporating black hole models, and an elementary analysis of this class of spacetimes is undetaken. Penrose diagrams are defined in general at a basic level, and then constructed explicitly for the class of spacetimes under consideration.

The second article provides an introduction to the problem of modeling black hole evaporation, and constructs a set of explicit models and diagrams using the methods described earlier. The new models and diagrams are then used to analyze the physics of black hole evaporation.

Due to the comprehensive and self-contained nature of these articles, background material and conclusions are provided within each chapter.

In addition to the contents of this thesis, my doctoral research has touched on some related issues, including:

- Structure of rotating nonsingular ("regular") black holes.
- Spacelike propagation and energy condition violations in quantum fields.
- Local field visualizations of quantum scalar fields.
- New foundations for differential geometry using geometric algebra.

Publications related to these topics are expected to be forthcoming shortly.

Chapter 2

Algorithms for the explicit computation of Penrose diagrams

This chapter is based on the article "Algorithms for the explicit computation of Penrose diagrams" by Joseph Schindler and Anthony Aguirre [1].

Abstract

An algorithm is given for explicitly computing Penrose diagrams for spacetimes of the form $ds^2 = -f(r)\,dt^2 + f(r)^{-1}\,dr^2 + r^2\,d\Omega^2$. The resulting diagram coordinates are shown to extend the metric continuously and nondegenerately across an arbitrary number of horizons. The method is extended to include piecewise approximations to dynamically evolving spacetimes using a standard hypersurface junction procedure. Examples generated by an implementation of the algorithm are shown for standard and new cases. In the appendix, this algorithm is compared to existing methods.

2.1 Introduction

Visualizing the causal structure of curved spacetime is among the basic tasks of relativistic physics. A useful tool in this pursuit, the technique now known as Penrose diagram analysis, in which finite coordinate diagrams of conformally transformed spacetimes are used to visualize global structure, was first introduced by Penrose in 1964 [6, 7]. The same technique was soon implemented by Carter [8], who was first to provide such diagrams in a recognizably modern form. An important systematic analysis was later given by Walker in 1970 [9]. The significance of these techniques as a tool to study asympototic infinities in spacetime was quickly recognized [10].

It is surprising, given the importance of Penrose diagrams, that one rarely sees a "real" one. They are almost always hand-drawn — in fact, it is rare even to find a computer-generated Penrose diagram of Minkowski space. There are some exceptions to this rule, including a number of especially nice diagrams due to Hamilton [11], and some others from Griffiths and Podolskỳ [12]. However, no general method for the numerical computation of diagrams across a broad and interesting class of metrics has been given. To do so is the goal of this article.

An algorithm will be given for constructing and numerically generating Penrose diagrams for spacetimes in two classes:

(A) Maximally extended completions of spacetimes which locally have the form $ds^2 = -f(r)\,dt^2 + f(r)^{-1}\,dr^2 + r^2\,d\Omega^2$. (We refer to these spacetimes as *strongly spherically symmetric* (SSS), see section 2.4).

(B) Piecewise-SSS spacetimes with null-shell junctions. These are constructed by joining pieces of spacetimes of class (A) across null shells of matter. These may have an arbitrary finite number of shells and piecewise regions.

This is achieved by adopting a global contour integral definition of the tortoise coordinate (see section 2.5), and making a careful choice of the function that squishes the local double-null coordinates (see sections 2.4 and 2.5) into the global coordinate patch. The result is a *global* double-null patch of "Penrose" coordinates (see section 2.2) in which the metric is continuous and non-degenerate at the horizons.

The new techniques we describe are similar in most respects to those used by Carter, Walker, and others. Our technique differs, however, by achieving simultaneous global coordinates for an arbitrary number of blocks across an arbitrary number of horizons, being numerically computable with weak restrictions on the metric function $f(r)$, and yielding diagrams whose lines of constant radius take on an intuitive shape. For a detailed comparison of the new and existing methods, see 2.9.

There are a few reasons why Penrose diagrams have continued to be hand-drawn in the computer age, which is to say, why this algorithm has not been given sooner. Most importantly, the outline and qualitative appearance of Penrose diagrams for SSS spacetimes can be determined by the block diagram method of Walker [9]. When the diagram is being constructed primarily for analysis at infinity, the interior structure is irrelevant, and so the qualitative block diagram method is sufficient. Moreover, most known Penrose diagrams represent either vacuum spacetimes, or spacetimes with a homogeneous distribution of matter, making interior analysis rather dull. In contrast to these historical precedents, we wish to study diagrams for spacetimes which have nontrivial matter distributions, and which are dynamically evolving in nontrivial ways. The detailed interior appearance of such diagrams is not obvious from the standard qualitative analysis.

In particular, a major motivation for this endeavor is the desire to produce a

detailed Penrose diagram for the process of black hole formation and evaporation, such that the distribution and flow of matter can be clearly and explicitly tracked. Fortunately, since class (B) above includes piecewise approximations to many interesting dynamically evolving geometries (e.g. Vaidya metric [12], forming and evaporating Hayward black hole [13], and stellar-collapse black hole models), the algorithms presented in this article will make that goal accessible.

An outline of the article is as follows.

Sections 2.2-2.4 serve two purposes. First, to review the well-known theory of Penrose diagrams in general and as applied to strongly spherically symmetric spacetimes. And second, to establish a clear and modern formalism in which to state the results of later sections. We hope that this formalism helps distill the key features of standard Penrose diagram analysis, and that these sections might be used as a pedagogical introduction to the subject for students with a strong background in differential geometry.

Sections 2.5-2.6 present new techniques for the practical construction of Penrose diagrams, while Section 2.7 describes an implementation of these techniques, and gives examples generated by the implementation. 2.9 gives a detailed comparison between existing methods and the new methods.

Some of the appendices may be of general interest. Readers interested in the symmetry of manifolds may enjoy 2.11, which shows how spherical symmetry about a particular rotation axis can be defined, even when the symmetry axis is not itself a part of the manifold. 2.10 describes a useful unit convention for tensor components in relativity. And 2.13 collects a variety of useful geometric information about SSS spacetimes, including discussions of their trapped surfaces, physical singularities, and energy condition violations. The other appendices cover details particular to the text.

For those wishing to quickly see the practical algorithms we employ, the most direct route is to read section 2.5.4 followed by 2.6.2. The examples in figures 2.15 – 2.18, and the comparison to other methods in 2.9, should also be consulted. Additionally, scanning figure 2.2 will help clarify the SSS spacetime terminology. This quick path through the paper is mostly, but not entirely, self-contained.

2.2 Penrose diagrams in two and more dimensions

We begin by reviewing the general theory of Penrose diagrams, and establishing a formalism commensurate with standard practices.

In general, the term "Penrose diagram" refers to a broad class of spacetime diagrams from which the causal structure of a spacetime can be easily read off. In particular, a Penrose diagram should make evident (i) the lightcone structure, and (ii) the causal structure of conformal infinity (defined below). This is typically achieved by covering a two-dimensional slice of a spacetime with a finite patch of double-null coordinates. Although most authors need not bother to have a rigorous definition of Penrose diagram in mind, it is possible to give a precise definition which is in line with typical use. We do so now for the case of two dimensions, and then discuss the generalization to higher dimensions.

2.2.1 Rigorous definition in two dimensions

Consider a two dimensional spacetime M, and an open set $U \subset M$. Let $\varphi : U \to \mathbb{R}^2$ be a chart on M, with coordinates $\varphi(p) = (u, v)$ for $p \in U$. Let $\overline{U}$ denote the closure of U, and let $\varphi(U)$ denote the image of U in $\mathbb{R}^2$. Then φ

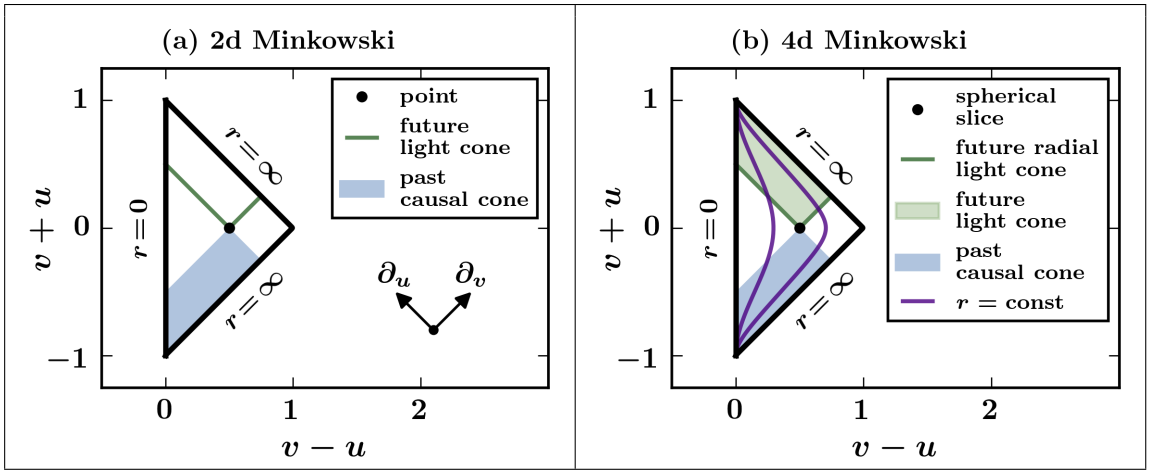

Figure 2.1: (Color online). Penrose diagrams for flat spacetimes in (a) two and (b) four dimensions. See text at the end of section 2.2.2 for details.

may be called a *Penrose chart* if it satisfies three conditions: (I) $\overline{U} = M$; (II) there exists a compact $V \subset \mathbb{R}^2$ such that $\varphi(U) \subset V$; (III) in coordinates (u, v) the metric takes the form $ds^2 = -g(u, v)\, du\, dv$, such that $g(u, v) > 0$ and ∂_u, ∂_v are both future-directed. When φ is a Penrose chart the coordinates (u, v) may be called *Penrose coordinates*, and the boundary of the closure of $\varphi(U)$ is called the *conformal boundary* of M. Any plot of M in Penrose coordinates is called a *Penrose diagram*.

Condition (I) ensures[1] that the diagram includes all of M, while allowing some points to be left out to avoid technical difficulties (such as polar coordinate singularities) associated with attempting to cover all of M in a single chart. Condition (II) ensures that the coordinate patch is finite, which allows the entirety of M to be represented in a finite diagram, and allows analysis of the conformal boundary.

[1]Sometimes M has a periodic structure, in which case this condition can be weakened. Suppose M consists of a periodic arrangement of regions isometric to N. Then it suffices to require of a Penrose chart only that (I') $\overline{U} = N$, so long as we specify how the regions N are connected. This information is, of course, equivalent to knowing the global causal structure. Standard examples of the periodic case are the maximally extended Reissner-Nordstrom and Kerr (on axis) spacetimes [10].

And condition (III) ensures that the Penrose coordinates are double-null, making it trivial to identify lightcones and causal cones in the coordinates. Indeed, for any parameterized null curve $\dot{u}\dot{v} = 0$, which implies that the curve follows lines of constant u or v (where dot represents a derivative with respect to curve parameter). This determines the lightcone at each point. The causal interior of the lightcone may then be determined by the condition $\dot{u}\dot{v} > 0$ for timelike curves. Because of these restrictions on the lightcones, a Penrose diagram is typically plotted with x-axis $(v-u)$ and y-axis $(v+u)$. In such a case the lightcone is formed by rays at 45° angles to the axes, with the top wedge being the future causal cone and the bottom wedge being the past causal cone (see Figure 2.1).

The conformal boundary B of M under φ, as defined above, plays a key role in understanding global causal structure because it allows the analysis of causal structure at "infinity". The existence of a nonempty B under a Penrose chart φ is guaranteed by condition (II) above. In general, points $b \in B$ may be one of several types: (i) b may represent points at "infinity"; (ii) if M is incomplete at a curvature singularity, b may represent the singularity; (iii) if M is incomplete without curvature singularity, b may represent a boundary where "missing" parts of M are simply left out. When working in more dimensions (see below), there is an additional possibility that (iv) b represents a coordinate boundary of the projection (e.g. $r = 0$). In practice it is usually easy to distinguish between the various possibilities, and to identify the boundary set $\mathcal{I} \subset B$ representing infinity. This set $\mathcal{I}$ is called *conformal infinity*. Our definition of conformal boundary is similar to that originally set forth by Penrose [7]. The more common definition in terms of terminal indecomposable sets [14] is more general but less easily applicable when a Penrose chart exists.

In two dimensions, the Penrose chart φ describes a conformal isometry of U

into a subset of Minkowski space, when the coordinate space is equipped with metric $ds^2 = -\,du\,dv$. This allows the geometry of the boundary to be studied in the conformal Minkowski space, and is the reason for the term "conformal" boundary. Since conformal isometries preserve causal structure, studying $\mathcal{I}$ in the conformal space determines the causal structure at infinity in M. Determining this structure is one of the main goals of constructing a Penrose diagram for M.

Practically speaking, the effort of constructing the Penrose diagram comes in two parts: (i) obtaining local double null coordinates; and (ii) manipulating the local patches to achieve a global double null coordinate system in which the metric is well-behaved (in the sense of condition (III)). Once (ii) has been achieved, it is trivial to (if necessary) squish and flip the global coordinates so as to attain Penrose coordinates. In sections 2.4 - 2.5 we will show for a certain class of spacetimes that (i) is trivial, and describe a method for resolving (ii). This method results immediately in Penrose coordinates.

2.2.2 Generalization to higher dimensions

How does this definition extend to higher dimesions? In the case of spherical symmetry, the theory goes through nearly unchanged. In this section, let M have $D = 2 + n$ spacetime dimensions.

When spherical symmetry is present, a Penrose chart should be defined analogously to the two dimensional case, with the modification that for $p \in U$, $\varphi(p) = (u, v, \Omega)$ with $ds^2 = -\,g(u,v)\,du\,dv + r(u,v)^2\,d\Omega^2$. Here Ω represents a collection of angular coordinates, and $d\Omega^2$ the metric of an n-sphere. The diagram is then constructed by defining the *projective Penrose chart* $\tilde{\varphi}$ by $\tilde{\varphi}(p) = (u, v)$ and the *projective metric* $d\tilde{s}^2 = -\,g(u,v)\,du\,dv$. In this way, one essentially creates

a Penrose diagram of the two dimensional spacetime transverse to the angular directions. Each point on the diagram represents a sphere of areal radius $r(u, v)$. It is important not to discard the radial information, as only by retaining the function $r(u, v)$ can the geometry at each point of the diagram be specified.

But even in case of spherical symmetry, the theory is slightly modified. The interpretation of the conformal space is no longer strict, since the coordinate Minkowski space is only conformal to $d\tilde{s}^2$ after projection into two dimensions. The projection into two dimensions also has the effect that the appearance of lightcones in the diagram is qualitatively altered. Null curves in D dimensions obey $\dot{u}\dot{v} = g(u, v)^{-1} r^2 \dot{\Omega}^2 \geq 0$, while timelike curves obey $\dot{u}\dot{v} > g(u, v)^{-1} r^2 \dot{\Omega}^2 \geq 0$. Thus, two-dimensional null curves in the confomal Minkowski space now represent only the radial null curves in M, while D-dimensional null curves with angular momentum in M appear timelike in the conformal space. The D-dimensional lightcones of M, therefore, fill the interior of the two-dimensional causal cones in the conformal space. Despite these several modifications to the interpretation of the conformal space, the conformal method for studying infinity remains useful, and the name conformal boundary is retained.

For most of our purposes it will be convenient to deal with spherically symmetric shells and particles constrained to move in the (u, v) plane. It is therefore useful to identify the *radial lightcones*, defined by $\dot{u}\dot{v} = 0$, which are the effective lightcones for such objects. The D-dimensional radial lightcones are equivalent to the two-dimensional conformal lightcones. *Radial causal cones* can be defined similarly. This concludes the extension from two dimensions to spherical symmetry in D dimensions.

In some cases the spherically symmetric formalism can be generalized further. Let A be a two-dimensional Lorentzian manifold with line element dA^2, and let

$h(a)^2$ be a positive real scalar function on A. Let B be an n-dimensional homogeneous Riemannian manifold with line element dB^2. If there exist such an A and B for which a dense open submanifold $U \subset M$ is isometric to the product $A \times B$ with metric $ds^2 = dA^2 + h(a)^2\, dB^2$, then a formalism directly analogous to that for spherical symmetry can be used (although if B is not compact, condition (II) should be modified to apply only to the projective chart $\tilde{\varphi}$, and one should be careful in interpretation). This includes cases of planar, hyperbolic, and spherical symmetry, among others. The above condition implies that M has at least n spacelike Killing vector fields, and is essentially equivalent to the condition that M can be acted on by an n-dimensional group of spacelike isometries.

When M lacks sufficient symmetry for analogous methods to be applied, by having nontrivial geometry in more than two dimensions, one must resort to piecing together the structure by observing various two-dimensional projections. This case is less common due to its complexity, and the theory of projection diagrams due to Chruściel *et. al.*should be consulted [15].

Figure 2.1 illustrates the basic features of a Penrose diagram in two and four dimensions using the simple case of flat spacetime. In this example, the two-dimensional spacetime is defined by $ds^2 = -dt^2 + dr^2$ on the coordinate patch $r \in (0, \infty)$ and $t \in (-\infty, \infty)$, while the four-dimensional spacetime is defined by $ds^2 = -dt^2 + dr^2 + r^2\, d\Omega^2$ on the same coordinate patch. In both cases, the Penrose coordinates are given by $u = \pi^{-1} \tan^{-1}(t - r)$ and $v = \pi^{-1} \tan^{-1}(t + r)$. The resulting metrics are

$$ds^2 = -\pi^2 \sec^2(\pi u)\, \sec^2(\pi v)\, du\, dv$$

and

$$ds^2 = -\pi^2 \sec^2(\pi u)\, \sec^2(\pi v)\, du\, dv + r^2\, d\Omega^2,$$

where, in four dimensions, the areal radius at each point is given by $r = r(u, v) = (\tan \pi v - \tan \pi u)/2$. Note that the two-dimensional example, which is half of a two-dimensional Minkowski space, is incomplete at $r = 0$ by construction so as to more closely parallel the four-dimensional case.

2.3 A note about units

A detailed review of our unit conventions and their justification is given in 2.10. In short: *all coordinates, parameters, tensor components, and lengths appearing in the article are unitless.* Proper units are restored by establishing an overall length scale, which can be propagated through all quantities. For details, please see the appendix.

To make the convention as clear as possible, consider the example

$$ds^2 = -(1 - R/r)\, dt^2 + (1 - R/r)^{-1}\, dr^2 + r^2\, d\Omega^2\ . \tag{2.1}$$

The radius r, the coordinates (t, r, Ω), the parameter R, the one-forms $(dt, dr, d\Omega)$, and the line element ds^2 should all be regarded as unitless. To relate this to a physical metric, one would establish an overall length scale l. Then the physical coordinates $(lt, lr, l\Omega)$ and physical line element $d\bar{s}^2 = l^2 ds^2$ would all have units of length, and other quantities would inherit units as appropriate.

2.4 Strongly spherically symmetric spacetimes and their maximal extensions

The class of spacetimes with metric of the form

$$ds^2 = -f(r)\,dt^2 + f(r)^{-1}\,dr^2 + r^2\,d\Omega^2 \tag{2.2}$$

(where $d\Omega^2$ signifies the metric on a unit n-sphere) is of great historical and practical significance: common examples include the Schwarzschild, Reissner-Nordstrom, de Sitter, Anti de Sitter, and Minkowski solutions of GR, among numerous others. Strangely, given their ubiquity, this class of spacetimes lacks a standard name. We introduce some new terminology, and review some properties of these spaces, below.

In particular, we will see that every spacetime which locally has the metric (2.2) can be isometrically embedded into a spacetime of a larger class, which we will call the "strongly spherically symmetric" (SSS) spacetimes. In this section we develop a detailed geometrical description of such spacetimes.

Historically, our "strongly spherically symmetric" spacetimes have sometimes been called "static spherically symmetric" [16]. But when $f(r) \leq 0$ they are not static (do not have a timelike Killing vector field), so the term is not apt. The new name seems more fitting: the symmetry is "strong" in the sense that, in addition to the spherical symmetries, there exists a Killing vector field normal to the angular directions, which allows the metric components to be expressed as functions of the radius only.

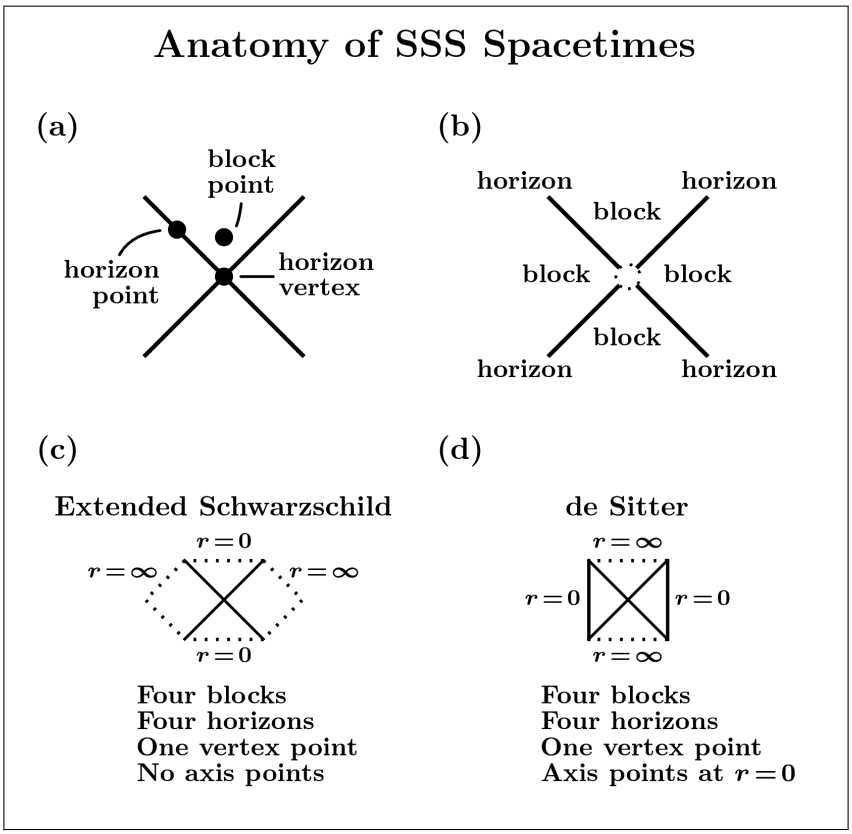

Figure 2.2: Illustration of the anatomy of SSS spacetimes. (a) The classification of points is given in section 2.4.3. (b) The definition of blocks and horizons is given in section 2.4.4. In this image the vertex point is omitted to clarify that four disconnected horizons are present. (c,d) Block diagrams are discussed in section 2.4.6. In these two block diagrams conformal boundary points which are not in M are dotted (which is not our standard convention). The extended Schwarzschild solution has metric function $f(r) = 1 - R/r$, and has no axis points since the singularity at $r = 0$ is excluded from the spacetime. In de Sitter space, with metric function $f(r) = 1 - (r/l)^2$, every point at $r = 0$ is an axis point. In all cases, radii are measured by defining orbits of a rotation group, as discussed in section 2.4.1.

2.4.1 Spacetimes with spherical symmetry about a fixed origin

To properly describe strong spherical symmetry requires the concept of spherical symmetry about a fixed origin. Since manifolds need not contain their symmetry axes, this requires a little bit of finagling. In 2.11 it is shown that for any spherically symmetric spacetime M, one can specify the origin of spherical symmetry by selecting a particular algebra σ of Killing vector fields satisfying certain assumptions. This choice determines spherical orbits of a rotation group; the curvature of these orbits is used to define the radius at each point.

Once the "origin of symmetry" has been fixed by choosing σ, the areal radius $r = r_\sigma(p)$ is an intrinsic property of each point $p \in M$, independent of coordinate system. M is foliated by spheres (lying tangent to σ) with intrinsic metric $ds^2 = r_\sigma(p)^2\, d\Omega^2$, except on the axis of symmetry where $r_\sigma(p) = 0$ by definition. Everywhere except on the axis, there is a local coordinate system respecting this foliation, in terms of which the metric is (2.35).

In our treatment of strong spherical symmetry, we will assume that M is spherically symmetric, and that the origin of symmetry has been fixed by selecting a particular σ. This ensures that local SSS patches all have symmetry about the same origin.

2.4.2 Coordinate naming conventions

Up to now, our convention has been to denote Penrose coordinates by (u, v). Hereafter, Penrose coordinates will usually be denoted by $(\tilde{u}, \tilde{v})$, while coordinates (u, v) will be reserved for the usual local double-null coordinates with metric (2.7) below. Coordinates (t, r) refer of course to standard Schwarzschild-like coordinates

with metric (2.2). And coordinates (w, r) will denote the Eddington-Finklestein (EF) coordinates with the metric (2.3) below, such that the EF time w may be either advanced or retarded depending on a parameter $\epsilon = \pm 1$ and a choice of time-orientation. In either case, the vector field ∂_w is locally equivalent (up to a global normalization) to ∂_t wherever the latter is defined. For reasons that will become clear below, we will define strong spherical symmetry in terms of the EF coordinate system (w, r), and its associated Killing vector field ∂_w.

At times it is convenient to refer ambiguously to one of the double-null coordinates (u, v), without specifying which one. When this is necessary we will utilize the placeholders (x, y), where it is understood that either $(x, y) \equiv (u, v)$ or $(y, x) \equiv (u, v)$. The same placeholder convention extends to $(\tilde{u}, \tilde{v})$.

2.4.3 Spacetimes with strong spherical symmetry

Suppose M is a spacetime of dimension $D = 2+n$, and that M is n-spherically symmetric with axis fixed by σ (see section 2.4.1). Then M will be said to have *strong spherical symmetry (about axis σ) with metric function $f(r)$* if every open set $U \subset M$ has an open subset $V \subset U$ isometric to[2]

$$ds^2 = -f(r)\, dw^2 - 2\epsilon\, dw\, dr + r^2\, d\Omega^2 \qquad (\epsilon = \pm 1)\ , \tag{2.3}$$

in coordinates (w, r, Ω), such that $r(p) = r_\sigma(p)$ and σ lies tangent to Ω. Those last bits ensure that all points have a strong spherical symmetry about the same origin. In practice we always define σ in terms of this metric, so these technicalities become trivial. Assumptions on the function $f(r)$ are given below, near the end

[2]Here and later we abuse terminology by omitting the full statement "isometric to an open subset of $\mathbb{R}^D$ on which the metric ds^2 is defined", which should be obvious from context. This is equivalent to saying there exists a coordinate patch on M in which the metric takes this form.

of this section.

The definition implies that the set

$$X = \{p \in M \,|\, p \text{ has a neighborhood isometric to (2.3)}\} \tag{2.4}$$

is open and dense in M. Using the Eddington-Finkelstein (EF) form (2.3) of the metric allows X to contain points where $f(r) = 0$, and implies that M is locally isometric to $ds^2 = -f(r)\,dt^2 + f(r)^{-1}\,dr^2 + r^2\,d\Omega^2$ at points in X where $f(r) \neq 0$.

The spherical symmetry is called "strong" due to the presence of a Killing vector field normal to the angular directions, which allows the metric components to be expressed as functions of the radius only. Indeed, by definition, the metric is independent of coordinate w, and so ∂_w is a local Killing vector field. It is easily seen from the metric that ∂_w is null wherever $f(r) = 0$, and that ∂_w is always normal to the angular directions.

In general, SSS spacetimes can contain four distinct types of points:

1. points not in X at which $r = 0$ (*axis points*)
2. points in X at which $f(r) \neq 0$ (*block points*)
3. points in X at which $f(r) = 0$ (*horizon points*)
4. points not in X at which $r \neq 0$ (*horizon vertices*)

The reason for these names will become clear later. The isometry associated with flow along ∂_w preserves this classification, and has the horizon vertices as fixed points. Moreover, every point in X has a neighborhood where ∂_w is an everywhere-nonzero Killing vector field tangent to lines of constant radius. For an illustration of the different types of points, see figure 2.2.

It is now appropriate to explain the need for fixing the symmetry axis. Without doing so, the presence of additional symmetries can make it impossible to geometrically distinguish points in M. Take, for example, the de Sitter spacetime, with metric function $f(r) = 1 - (r/l)^2$. Since de Sitter is homogeneous, every point is geometrically indistinguishable. In particular, every point may be described as lying on a cosmological horizon. From the point of view where we consider de Sitter an SSS spacetime, the additional freedom to choose the origin of symmetry is superfluous (though by no means unimportant). By fixing the origin, we allow points and regions to be classified as above. Additionally, fixing the origin allows us to refer to the radius of a point without reference to any particular system of coordinates.

We typically describe a particular strongly spherically symmetric spacetime by specifying its metric function $f(r)$ on the interval $r \in (0, \infty)$. For simplicity, we assume that $f(r)$ always has the following properties: (I) $f(r)$ is continuous and once differentiable; (II) $f(r)$ has a finite number N of zeroes; (III) $f(r)$ is analytic at its zeroes; (IV) all zeroes of $f(r)$ are isolated and simple (linear); and (V) $\lim_{r\to 0} f(r) \neq 0$.

The assumption that $f(r)$ is analytic at its zeroes allows the use of a concise contour integral definition of the tortoise coordinate (see section 2.5.1); since $f(r)$ need not be analytic globally, the assumption is fairly weak. Note that $f(0)$ need not be defined. And moreover, the assumption that $f(r)$ does not approach zero in the $r \to 0$ limit is not strictly necessary; it conveniently avoids the treatment of certain edge cases, but can be relaxed with no serious consequences.

It is useful to define a consistent notation for critical values of the radius, in order to partition the radial coordinate into intervals separated by horizon radii. The endpoints of these intervals occur at $r = 0$, at the N horizon locations where

$f(r) = 0$, and at $r = \infty$. We therefore let $r_0 = 0$, denote the zeroes of $f(r)$ by r_i for $i = 1, 2, \ldots, N$, and let $r_{N+1} = \infty$. Then the radius values r_j, for $j = 0, 1, \ldots, N$, partition the radial coordinate into intervals $I_j = (r_j, r_{j+1})$, and in each interval I_j the sign of $f(r)$ is constant. In this context we reserve the subscript i to refer only to the zeroes of $f(r)$, while expressions with subscript j additionally include r_0 and r_{N+1}.

In what follows, a parameter k_j will control coordinate transformations in the vicinity of each critical value r_j of the radius. Near each zero r_i of $f(r)$ it must have a particular value, equal to the slope of $f(r)$ at r_i, in order for the metric to extend continuously across the corresponding horizon. Where no horizon matching is needed, however, it may be set to zero, yielding a simplified coordinate transformation. In accordance with these requirements, we define $k_0 = 0$ at $r_0 = 0$, $k_i = f'(r_i)$ at the N zeroes of $f(r)$, and $k_{N+1} = 0$ at $r_{N+1} = \infty$. This ensures matching at all horizons, while providing the simplest possible transformations near $r = 0$ and $r = \infty$, where no matching is needed.

Specifying the metric function determines the local structure of M, by insisting that (2.3) holds for the fixed function $f(r)$. Some ambiguity remains in the global structure. We will see in section 2.4.6 below that in fact such an M might be any subset of a maximally extended M' corresponding to $f(r)$. This is the class of spacetimes intended by (A) in section 2.1.

For the remainder of this section, let M denote a strongly spherically symmetric spacetime with metric function $f(r)$.

2.4.4 Horizons and blocks

It is useful to think of M as being partitioned into "blocks" separated by "horizons".

First let us mention the horizons. A connected hypersurface consisting of horizon points in M, on which $r = \text{const}$ and $f(r) = 0$, is called a *horizon*. Correspondingly, the values r_i where $f(r) = 0$ may be called *horizon radii*. Every horizon is a null hypersurface, being normal to the (locally) null vector ∂_w. Moreover, horizons are always Killing horizons, and often trapping horizons (see [17, 18] for definitions). The Killing horizon property is immediate, since the Killing vector field ∂_w is null at a horizon. The trapping property we will return to shortly. Now let us move on to the blocks.

A *block* is a region of M, consisting of a connected set of block points, which corresponds to a single interval I_j over which the metric function is nonzero. Each block can be covered by the metric (2.2) defined on a coordinate patch $r \in I_j$ and $t \in (-\infty, \infty)$. Note that this metric may approach a coordinate singularity at the boundaries of the patch. There is a one-to-one correspondence between the intervals I_j and the *types* of blocks in M. However, M may contain many blocks of the same type, each corresponding to the same interval I_j. We will often label blocks by their corresponding interval, which indicates their type.

To construct Penrose coordinates for a single block is straightforward. To begin, choose an arbitrary point $a \in I_j$. Define the *tortoise coordinate* r_* and *tortoise function* $F(r)$ by

$$r_* = F(r) = \int_a^r \frac{dr'}{f(r')} \,. \tag{2.5}$$

The tortoise function obeys $dF/dr = f(r)^{-1}$, and is monotonic over I_j since $f(r)$

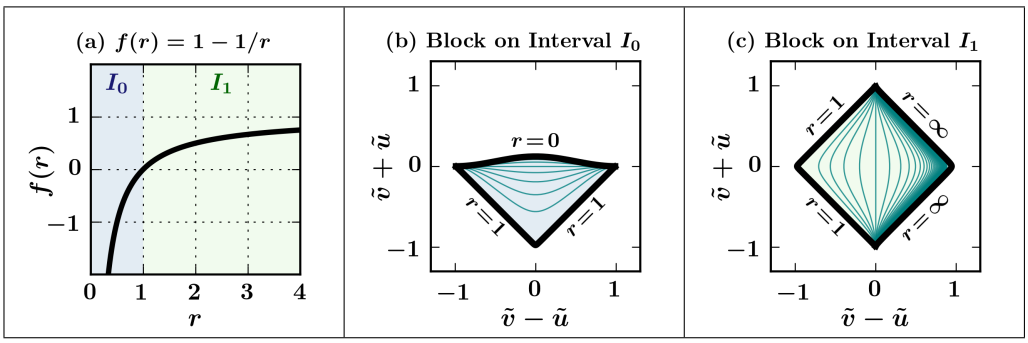

Figure 2.3: (Color online). Penrose diagrams for some individual blocks of an SSS spacetime with $f(r) = 1 - 1/r$. We have employed the methods of secion 2.4.4, with integration points $a_1 = 0.5$ and $a_2 = 1.5$, integration constants $c_0 = c_1 = 0$, and squishing functions $\tilde{u}_0(u) = -\tilde{u}_1(u) = -\pi^{-1}\tan^{-1}(u)$ and $\tilde{v}_0(v) = \tilde{v}_1(v) = \pi^{-1}\tan^{-1}(v)$, in regions corresponding to the intervals $I_0 = (0, 1)$ and $I_1 = (1, \infty)$. Lines of constant areal radius $r = const$ (teal) are depicted in the diagram at intervals $dr = 0.1$, and the radius at any diagram point can be determined numerically by (2.10). Heavy black lines denote the conformal boundary of each block. The causal shapes are triangle for I_0 and diamond for I_1, and the block I_0 is a trapped region containing future-trapped surfaces. Each block is bordered on one side by two horizons (and a horizon vertex) at $r = 1$. Although the blocks can in principle be joined continuously at the matching horizon, this individual-block method doesn't give a way to do so.

is continuous and nonzero there. Thus $F(r)$ is invertible on I_j, and we denote the inverse function by $r = F^{-1}(r_*)$. The arbitrary choice of $a \in I_j$ amounts to an arbitrary additive constant in $F(r)$, which we later absorb into a choice of double null coordinates. The range of r_* depends on the behavior of $f(r)$ near the endpoints of I_j; the value becomes infinite in magnitude near each simple zero of $f(r)$.

Next a set of double null coordinates for the block, with a parameter $c \in \mathbb{R}$ absorbing the tortoise function's free additive constant, is defined by

$$u = t - r_* + c\,, \qquad v = t + r_* - c\,, \tag{2.6}$$

in terms of which the metric becomes

$$ds^2 = -f(r)\,du\,dv + r^2\,d\Omega^2\,, \tag{2.7}$$

with $r = F^{-1}\left((v-u)/2 + c\right)$.

Finally, one chooses two invertible monotonic functions $\tilde{u}(u)$ and $\tilde{v}(v)$, called the *squishing functions*, each with domain $\mathbb{R}$ and finite range, such that

$$f(r)\,\frac{du}{d\tilde{u}}\,\frac{dv}{d\tilde{v}} > 0 \qquad \text{for} \qquad (r \in I_j), \tag{2.8}$$

and such that $\partial_{\tilde{u}}$ and $\partial_{\tilde{v}}$ are both future directed.

The resulting metric reads

$$ds^2 = -f(r)\frac{du}{d\tilde{u}}\frac{dv}{d\tilde{v}}\,d\tilde{u}\,d\tilde{v} + r^2\,d\Omega^2\,, \tag{2.9}$$

where

$$r = r(\tilde{u}, \tilde{v}) = F^{-1}\left(\frac{v(\tilde{v}) - u(\tilde{u})}{2} + c\right), \tag{2.10}$$

and $(\tilde{u}, \tilde{v}, \Omega)$ are Penrose coordinates for the block.

Any block bounded by simple zeroes of $f(r)$ admits the full range of coordinates $u \in (-\infty, \infty)$ and $v \in (-\infty, \infty)$, and therefore covers a diamond in the Penrose diagram. Blocks admitting a smaller range of (u, v) lie inside this diamond (when the same squishing functions are used).

The freedom involved in obtaining Penrose coordinates according to the above process is less than it may at first seem. First of all, note that the squishing functions should be chosen for simplicity and convenience. Once some squishing functions have been chosen, there is always the possibility to rescale by monotonic increasing functions in the u and v direction. This basically amounts to a freedom to mess up a nice-looking block, without making any structurally meaningful changes. Therefore let us focus on the choice of r_*, u, v. As seen already, the tortoise function $F(r)$ implicitly contains an arbitrary constant, which was absorbed into u, v by the free constant c. In light of this fact and the freedoms to translate u, v, t without disturbing the metric, one is tempted to write $(u - u_0) = (t - t_0) - (r_* - c)$ and $(v - v_0) = (t - t_0) + (r_* - c)$. These may be rearranged, however, to yield $u = (t - t_0') - (r_* - c')$ and $v = (t - t_0') + (r_* - c')$. But translations of t, being isometries of the block which preserve the range of t values (since $t \in (-\infty, \infty)$), are entirely nonphysical and have no effect on the appearance of Penrose diagrams. The equations (2.6) are therefore sufficiently general to exhibit all relevant freedoms in the process. Like with the squishing functions, changing the parameter c does not cause any important changes to the diagram; it simply alters the appearance, and may be chosen for convenience. Al-

though c is free in each block individually, we will see in section 2.5 that in order to construct global Penrose coordinates for many blocks, the values of c in each block must be carefully coordinated, and only a global additive constant remains.

Having now constructed Penrose coordinates for each block, let us use them to investigate the properties of these blocks more deeply.

The appearance of a block in the diagram is largely determined by the limits of the function $F(r)$ on the interval I_j. In general, each block is bounded by conformal boundaries corresponding to r_j and r_{j+1}. When $|F(r_j)|$ is finite, the block fails to fill its diamond near r_j, and the corresponding boundary is either timelike or spacelike. When $|F(r_j)|$ is infinite, the block fills a corner of the diamond, and the corresponding conformal boundary is null: it consists of two null horizons joined at a vertex (see figure 2.4). This makes sense, since whenever r_j is a horizon radius, the line of constant r_j is necessarily null, and the value $|F(r_j)|$ is necessarily infinite.

As determined by the above-stated dependence on $F(r)$, each block has a *causal shape* corresponding to its shape in the Penrose diagram. There are three possibilities; we denote them "diamond", "triangle", and "slug". When the conformal boundaries at r_j and r_{j+1} both are null, the shape is *diamond*. When one is null and the other either timelike or spacelike, the shape is *triangle*. When either both are timelike, or both are spacelike, the shape is *slug*. All blocks except the first and last necessarily have a diamond shape, and slugs are only possible when $f(r)$ has no zeroes. A block's causal shape is an intrinsic property of the type of block; it is the same in any Penrose diagram of the block, and for all blocks corresponding to the same I_j. Indeed, the tortoise function alone determines causal shape. The orientation of a block in the diagram, however, depends on the sign of $f(r)$ in the block, and on the block's time-orientation.

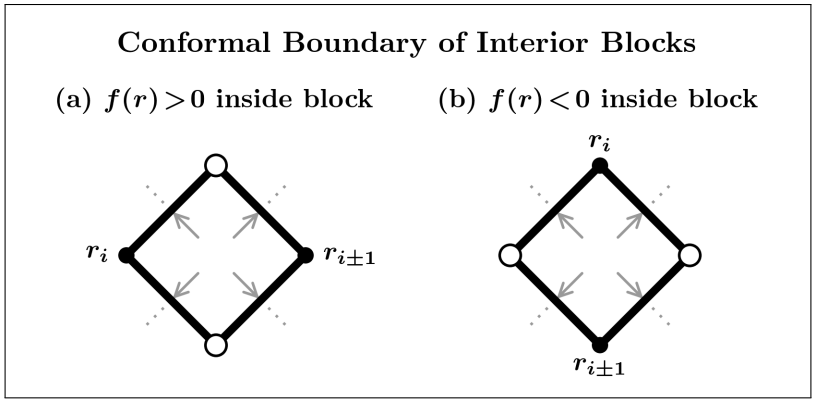

Figure 2.4: The conformal boundary of a block corresponding to interval $I_j = (r_j, r_{j+1})$ can be decomposed into boundaries corresponding to r_j and r_{j+1}. Additionally, there are two points (empty circles) on the boundary which do not correspond to any point in M, and do not have a well defined radius. Each illustration above shows an "interior" block, which is bounded by horizon radii (zeroes of $f(r)$) on both sides. For such a block, the pieces of the boundary associated with r_j and r_{j+1} each correspond to two horizons (bold lines) joined at a horizon vertex (solid circles). All interior blocks have four classes of incomplete radial null geodesics (gray arrows), each exiting the block through a different horizon. These classes can be classified as past or future directed and normal to ∂_u ($\nwarrow$) or ∂_v ($\nearrow$).

Every non-slug block, on its own, is extendible (geodesically incomplete without singularity) at its horizons. Indeed, to each horizon radius bounding I_j are associated two classes of incomplete null geodesics: either future-directed and past-directed, or left-going and right-going. These correspond to null rays exiting the two horizons making up the block's conformal boundary at that radius. It follows that each block bounded by two horizon radii (these are necessarily diamonds) has four such classes of incomplete null geodesics, while each block bounded by one horizon radius (these may be triangles or diamonds) has two such classes. Counting classes of extendible null geodesics suggests how many neighbors a block can have.

We now return to the question of trapping. In 2.13, it is shown that a sphere of constant (r, t) is a trapped surface if and only if $f(r) < 0$. It follows that within a

block with $f(r) < 0$, every point intersects a trapped surface. In light of this fact, blocks on which $f(r) < 0$ may sometimes be referred to as *trapped blocks*, and a union of trapped blocks is a *trapped region* (more generally, trapped regions are open sets on which every point intersects a trapped surface [19]). Trapped regions are important: an appealingly pragmatic definition of nonsingular black hole is "a future-trapped region terminating in a region of extreme density". There are various technical notions describing the horizon associated with a trapped region. Suffice it to say that under certain conditions, the boundary of the trapped region can be called a trapping horizon and/or apparent horizon [18].

Figure 2.3 exhibits Penrose diagrams for some individual blocks of an SSS spacetime with $f(r) = 1 - 1/r$. Note that there remains a freedom to invert the blocks by $(\tilde{u}, \tilde{v}) \to (-\tilde{u}, -\tilde{v})$, since no physical criteria has been given to establish a time-orientation. Parameters for the diagram construction are given in the caption.

Figure 2.4 illustrates the conformal boundary structure of blocks bounded by two horizon radii.

2.4.5 Ingoing/outgoing regions, Kruskal quad-blocks, and horizon vertices

Having observed that M is built from blocks, the next step is to see how these blocks can be joined together. There are two useful constructions that make this clear: Eddington-Finklestein (EF) regions, and Kruskal "quad-block" regions. As this section will demonstrate, each of these units highlights an important aspect of how blocks may be joined. In particular, the EF regions show how a chain of blocks can be linked to cover the entire range of radii. Meanwhile, the Kruskal

"quad-block" regions show how four blocks can be joined at a horizon radius by four horizons and a vertex. These constructions demonstrate that each block admits either zero, two, or four neighbors. These regions can be visualized using the block diagrams (see section 2.4.6) of figure 2.6.

First, we introduce the Eddington-Finklestein regions (figure 2.6a). A *full Eddington-Finklestein region* (*EF region*) is a subset of M which has the metric (2.3) everywhere on a coordinate patch $r \in (0, \infty)$ and $w \in (-\infty, \infty)$. Note that there is no coordinate singularity in this patch. When an EF region is time-oriented such that $-\partial_r$ is future (past) directed, it is called an *ingoing EF region* (*outgoing EF region*). EF regions are the smallest regions of M containing a point at every radius, and thereby are the smallest regions exhibiting the global function $f(r)$. They contain one of each type of block for M, with the blocks joined naturally across the horizons. The connectivity of the blocks is exactly the connectivity of the intervals I_j. Nonetheless, EF regions are, in general, extendible.

Every block of M can be isometrically embedded into two distinct EF regions, corresponding to the choice $\epsilon = \pm 1$ in (2.3), by using the transformation $w = t \mp r_*$ (see section 2.4.4 for definition of r_*) to obtain the coordinates (w, r) from the (t, r) in (2.2). The difference between these two regions is that different sets of incomplete null geodesics are extended. These two instances exhaust the block's extendible null geodesics, indicating that each block naturally has two neighbors for each horizon-radius bounding I_j. Within a given EF region, half of these possible neighbors are realized.

Next we will introduce the Kruskal quad-blocks (figure 2.6b). The classic example of this structure is the Kruskal diagram for extended Schwarzschild spacetime, with metric function $f(r) = 1 - 1/r$. In this case the Kruskal coordinates are usually constructed by defining (u, v) using the tortoise function

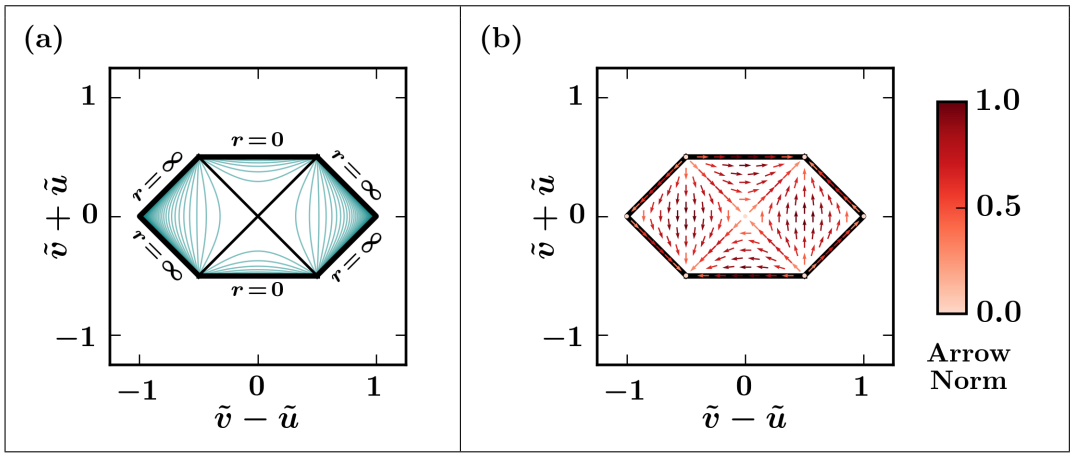

Figure 2.5: (Color online). Penrose diagram for the classic Kruskal extension of a Schwarzschild black hole, with metric function $f(r) = 1 - 1/r$, and tortoise function $\hat{F}(r) = r + \ln|r-1|$, according to the methods of section 2.4.5. Panel (a) shows lines of constant radius (teal) with spacing $dr = 0.1$. Interior black lines in (a) represent the horizons and vertex at $r = 1$. Panel (b) shows a global Killing vector field which is locally ∂_w (also locally ∂_t, see section 2.4.2), pushed forward into Penrose coordinates. In (b), the depicted unit vectors (arrows) must be multiplied by a scale factor (arrow norm color scale) to obtain the components of the Killing vector field. Note that the Killing vector field lies everywhere tangent to lines of constant radius. Apparent reflection symmetry within blocks in the Kruskal method is related to a curious identity: the function $\tan^{-1}(e^x) - \pi/4$ is odd. Since the Schwarzschild metric function has just one zero, the extended Schwarzschild spacetime has only one quad-block. Other SSS spacetimes may have many such regions, in which case the Kruskal extension method does not achieve a global coordinate system for all blocks simultaneously.

$\hat{F}(r) = r + \ln|r-1|$. Exponential transformations are then applied to (u, v) to attain the Kruskal coordinates, and the resulting metric is shown to be nondegenerate at the horizons. Because this tortoise function is defined analytically, it is easy to miss its key property: that $\hat{F}(r) - \ln|r-1| \to 1$ as $r \to 1$ from both the left and right. This did not have to be the case, as different constants could be added on either side of the discontinuity at $r = 1$ without messing up the derivative. This would be quite unnatural to do when $\hat{F}(r)$ is defined analytically, but is perfectly natural when it is defined by a definite integral (e.g. equation (2.5) above, which would in this case be applied on each side of $r = 1$). The limit obtained by subtracting out the logarithmic infinity may take any value (a global constant is allowed), but if the left and right limits were different, the metric would be undefined at the horizons.

The issues associated with defining a well-matched tortoise function are described in detail in section 2.5.1 below. In the present case, it suffices to take a simple generalization of the above observations: to construct a Kruskal quad-block centered at r_i in the general case, a tortoise function $\hat{F}(r)$ must be defined spanning both intervals I_{i-1} and I_i, such that $\lim_{r\to r_i}(\hat{F}(r) - \frac{1}{k_i}\ln|r-r_i|) = c$, where $k_i = f'(r_i)$, for some $c \in R$. This function exists and is unique due to our assumptions (section 2.4.3) on $f(r)$, and the indeterminate form $|f(r)|\, e^{-k_i\hat{F}(r)}$ is analytic at $r = r_i$ with the limit $|k_i|\, e^{-k_i c}$ (see section 2.5.1). The desired definition may now proceed.

A *Kruskal quad-block region* is centered on a horizon vertex at $r = r_i$ where $f(r_i) = 0$. It contains two types of blocks, corresponding to I_{i-1} and I_i, and the tortoise function must be defined as in the preceding paragraph above. A *Kruskal quad-block centered at* r_i has the metric $ds^2 = 4\,k_i^{-2}\,|f(r)|\, e^{-k_i\hat{F}(r)}\, d\hat{u}d\hat{v} + r^2\, d\Omega^2$, in coordinates $(\hat{u}, \hat{v}, \Omega)$, where $|\hat{u}\hat{v}| = e^{k_i\hat{F}(r)}$. The metric is defined on a coordinate

patch $min < \hat{u}\hat{v} < max$, where the max and min values depend on $f(r)$ and r_i. The patch is always nonempty and includes $\hat{u}\hat{v} = 0$. The point $\hat{u} = \hat{v} = 0$ is a horizon vertex; it has no neighborhood isometric to (2.3) because if it did there would be a smooth everywhere-nonzero vector field tangent to lines of constant radius in that neighborhood. The rest of $\hat{u}\hat{v} = 0$ consists of horizon points at $r = r_i$. In case of the traditional Kruskal region with $f(r) = 1 - R/r$ and $\hat{F}(r) = r + R \ln |r/R - 1|$, one immediately obtains $4\, k_i^{-2}\, |f(r)|\, e^{-k_i \hat{F}(r)} = 4R^3 r^{-1} e^{-r/R}$, which is the usual form of the prefactor in the traditional Kruskal metric.

Each quadrant of the Kruskal region is isometric to a single block of M. To make this evident, take the transformations $\hat{u} = \pm e^{-k_i u/2}$ and $\hat{v} = \pm e^{k_i v/2}$, followed by $u = t - \hat{F}(r)$ and $v = t + \hat{F}(r)$, yielding the usual block metric (2.2). Since every open set in the Kruskal region contains an open patch of an individual quadrant, this also proves that the region has strong spherical symmetry. In these coordinates the action of the Killing vector field ∂_w looks similar to a boost, and has the vertex as a fixed point. Penrose coordinates for the Kruskal region can be obtained by applying arbitrary squishing functions. Figure 2.5 shows a Penrose diagram for one Kruskal region.

Having exhibited the EF and Kruskal regions, the possible arrangements of joined blocks should be qualitatively clear. These arrangements are shown in figure 2.6. Figure 2.6a and 2.6b show the EF and Kruskal quad-block building blocks. Figure 2.6c shows how these can be combined to form larger structures. In figure 2.6c, each block is a part of two EF regions, and one or two quad-block regions.

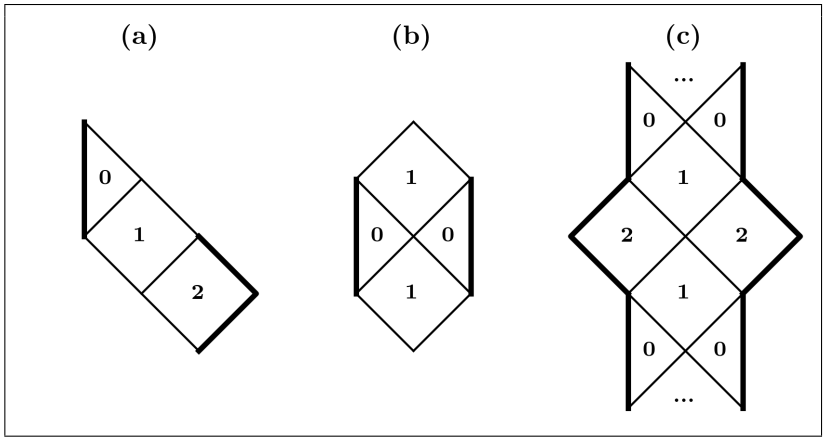

Figure 2.6: Block diagrams for an SSS spacetime with metric function $f(r) = 1 - 2r^2/(1 + r^3)$. The metric function has two zeroes. Shown are (a) an ingoing EF region, (b) a "quad-block" region, and (c) a piece of a maximal extension. Bold lines indicate conformal boundaries where $r = 0$ or $r = \infty$. Thin lines represent horizons at $r = 1$ and $r \approx 1.62$. Each block is labelled according to its interval I_j.

2.4.6 Block diagrams and maximal extension

Since we already know how each individual block looks in a Penrose diagram, and we now know how the blocks can be connected, it makes sense to draw a schematic *block diagram* of M. In such a diagram each block is drawn with the appropriate causal shape and orientation, and connected blocks are drawn sharing the relevant horizon. In this way, the global causal structure and topology of M can be accurately presented without need for a global Penrose diagram. Examples of block diagrams are given in figure 2.6.

Although a block diagram shares the qualitative appearance of its corresponding Penrose diagram, it lacks a global coordinate system. This has no effect on its usefulness as a tool for studying the global causal structure and topology. It does, however, stop us from accurately identifying the lines of constant radius, or plotting scalar functions of spacetime (e.g. the local density or local WEC inequality violation) on the digaram. For detailed analysis of dynamically evolving

piecewise-SSS spacetimes, we need these more advanced tools at our disposal.

To wrap up discussion of the global structure of SSS spacetimes, let us introduce the concept of maximal extension. Technically speaking, a (connected) manifold M' is *maximally extended* if it can't be isometrically embedded into a proper subset of another (connected) manifold M'' of the same number of dimensions [10]. In practice, it is often true that a spacetime is maximally extended when all geodesics are either complete or approach a physical singularity. In the context of SSS spacetimes, what we usually mean is that the block diagram for M leaves no open horizons. Block diagrams allow maximal extensions of SSS spacetimes to be described pictorially.

For any metric function $f(r)$, there is a maximally extended M' with the metric function $f(r)$ everywhere. The structure of such an an M' depends on the number N of zeroes of the metric function. For $N = 0$ every block is already maximally extended on its own. For $N = 1$, the maximal extension is unique and consists of a single quad-block region. For $N = 2$, maximal extensions may have a finite or infinite number of blocks, with a simple periodic structure similar to that seen in figure 2.6c. A finite number of blocks is possible (but only in the case $f(0)<0$) because of a topological ambiguity: torus-like boundary conditions can be allowed so long as closed timelike curves are avoided. Therefore maximal extensions in the case $N = 2$ are not always unique, but do always have a unique simply-connected cover. For $N > 2$, maximal extensions are constructed from an infinite chain of quad-block regions, and are not easily represented in a two dimensional block diagram. These necessarily have an infinite number of blocks, and suffer a similar topological ambiguity as the $N = 2$ case. When analyzing maximal extensions in the case $N > 2$, it is easiest to represent spacetime by a lattice of horizon vertices, rather than by a set of blocks. However, that method

is pursued no further here.

2.4.7 Boundary points with undefined radius

Points where $t \to \pm\infty$ on the conformal boundary of an SSS spacetime have a slight defect: their radius can't be well defined. This is obvious, since the same $t \to \pm\infty$ boundary point can be approached along lines of constant radius for a continuum of r values. For this reason, it is best to think of these points as representing an entire continuum of boundary points, each corresponding to a unique radius. Nonetheless, this continuum is represented in Penrose diagrams by a single point. Figure 2.7 highlights these defective points in two examples.

The undefined radius points impose a fundamental, but minor, limitation on the possibility of constructing global Penrose coordinates for SSS spacetimes: in any Penrose diagram of an SSS spacetime, each undefined radius point on the conformal boundary has a neighborhood in which the metric may be discontinuous (continuity occurs as a special case but not in general). The affected neighborhoods may be made arbitrarily small by choice of how the diagram is constructed. The red patches in figure 2.7 are meant to schematically represent the affected neighborhoods.

Since the neighborhoods where the metric is discontinuous can be made arbitrarily small, the problem imposed by these points is inconsequential. For any subset of M, or any worldline contained in M, the neighborhoods in which the metric is discontinuous can be "moved far enough out to infinity" so as not to effect the physical problem. In our construction of Penrose coordinates in section 2.5, a parameter s_0 will directly control the size of the affected neighborhoods, such that the neighborhoods become arbitrarily small as $s_0 \to \infty$.

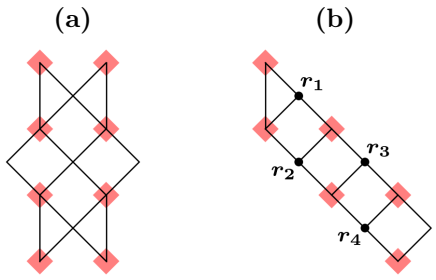

Figure 2.7: (Color online). Conformal boundary points where $t \to \pm\infty$ are highlighted in red. At each highlighted boundary point, no radius can be defined. Panel (a) shows a maximally extended region with $N = 2$ horizon radii, and panel (b) shows an EF region with $N = 4$ horizon radii. In panel (b), horizon vertices are dotted (solid black circles) and labeled by radius. Due to a fundamental limitation, the metric will be discontinuous in some (arbitrarily small) neighborhood of the undefined radius points, in any Penrose diagram of an SSS spacetime. See section 2.4.7.

Fundamentally, the issue is caused by the fact that a single undefined radius point on the conformal boundary may correspond to many different horizon radius values, in many different blocks, at the same time. The technical problem with this may be understood by observing the point between r_2 and r_4 on the bottom edge of figure 2.7b. Heuristically speaking, the metric will only be continuous at this point if the same coordinate transformation is applied on both sides. But on either side individually, a transformation must be carefully selected to make the metric continuous at the appropriate horizon (supposing more blocks are added to continue the region through the relevant horizons). Using the same transformation on both sides is, in general, incompatible with choosing the correct transformation on both sides. But since one only needs to be picky about transformations in a small neighborhood of the horizons, the problem can be pushed out into the corner.

The issue of undefined radius points is of a fundamental nature, and is not an artifact of any particular method for constructing diagrams. When there are more than two horizon radii (i.e. $N > 2$ zeroes of $f(r)$), the problem cannot be avoided.

On the other hand, in cases where $N = 0$ or $N = 1$, there are not enough horizon radii to force a discontinuity in the metric. In the case $N = 2$ there are enough horizons to cause a problem, but the discontinuity can be removed by a special choice of transformations. However, the procedure to do so is rather unnatural. Instead, in the method of section 2.5 we will leave the discontinuities, in order to use more natural transformations, and to keep the treatment unified.

2.4.8 True Penrose diagrams

We have seen that M can be partitioned into blocks, each with a well-defined causal shape. Moreover, we have seen how these blocks can be joined together across horizons in a regular way, and collections of blocks can be represented in a schematic block diagram. Lacking, so far, is a method for joining an arbitrary number of blocks, explicitly, in double-null coordinates.

This goal can be achieved in two key steps:

1. taking a global contour integral definition of the tortoise function; and

2. using a particular form of the squishing functions for each block.

Applying these steps results immediately in Penrose coordinates for M, in which the metric extends continuously and nondegenerately across all horizons. This will be the subject of section 2.5.

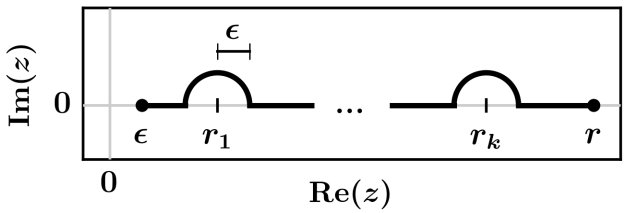

Figure 2.8: The contour $C_{r,\epsilon}$ used to define the global tortoise function. The contour avoids each pole of $f(r)^{-1}$ using a semicircle of radius ϵ in the upper half plane.

2.5 Explicitly computing Penrose diagrams for SSS spacetimes

This section provides the recipe for explicitly constructing Penrose coordinates for SSS spacetimes. First, a global tortoise function is defined using a contour integral. Then a useful choice of the squishing function for each block is defined. Finally, the algorithm for generating Penrose coordinates is stated in full, and the resulting metric is shown to be nondegenerate.

We continue to assume that $f(r)$ satisfies the criteria laid out at the end of section 2.4.3. In particular $f(r)$ has simple zeroes at $r = r_i$ (for $i = 1, 2, \ldots, N$) such that $f'(r_i) \neq 0$, and $f(r)$ is analytic at each of its zeroes. We denote $r_0 = 0$ and $r_{N+1} = \infty$, and the intervals $I_j = (r_j, r_j + 1)$ are defined for $j = 0, 1, \ldots, N$. The parameters k_j are defined by $k_0 = k_{N+1} = 0$ where no matching is needed, and by $k_i = f'(r_i)$ at the horizons.

2.5.1 Global tortoise function

A tortoise function is by definition an antiderivative of $f(r)^{-1}$. This leaves an arbitrary integration constant in each block. These must be coordinated such that, when the logarithmic infinities at the zeroes of $f(r)$ are subtracted out, what

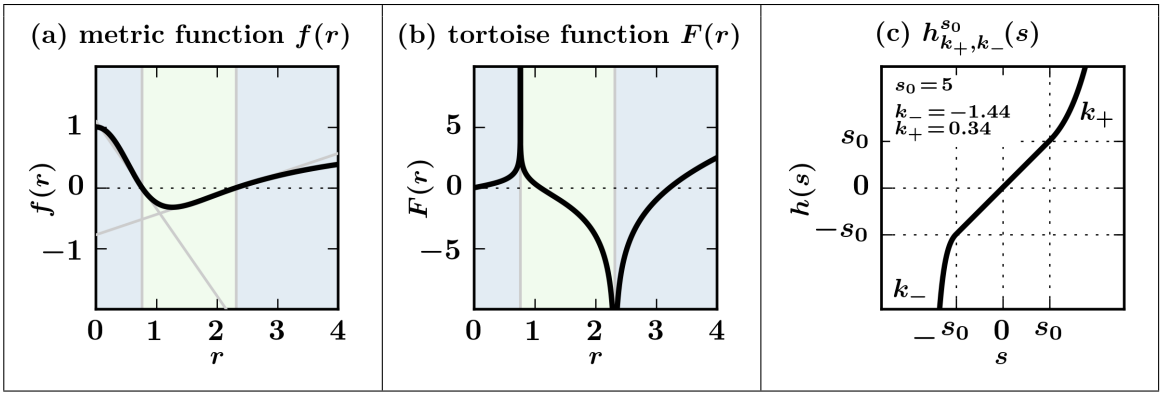

Figure 2.9: (Color online). Functions used to construct the Penrose diagram for an SSS spacetime with metric function $f(r) = 1 - 2.5\,r^2/(1+r^3)$. Panel (a) shows the metric function $f(r)$. Zeroes of $f(r)$ (vertical gray lines), which define horizon radii, are located at $r_1 \approx 0.758$ and $r_2 \approx 2.313$. Tangent lines (gray) to $f(r)$ at its zeroes have slopes $k_1 \approx -1.44$ and $k_2 \approx 0.34$ respectively. Panel (b) shows the corresponding global tortoise function $F(r)$, as defined by section 2.5.1. Note that near the "stronger" horizon with greater $|k_i|$, the logarithmic infinity of $F(r)$ appears "tighter". Panel (c) shows the pre-squishing function $h(s)$, as defined in section 2.5.2, corresponding to the interior interval $I_1 = (r_1, r_2)$ (light green), with the linear window parameter set to $s_0 = 5$. The exponential growth parameters are $k_+ = k_2 \geq 0$ and $k_- = k_1 \leq 0$, as appropriate for this interval. Note that positive (negative) values of s are associated with the positive (negative) parameter k_+ (k_-), and that the linear segment where $h(s) = s$ connects once-differentiably to the exponential tails.

remains is continuous. We adopt a definition for such a global function which is both analytically useful and numerically approximable. The only free parameter in this definition is a global additive constant, which has been absorbed into the definitions of (u, v).

Let $C_{r,\epsilon}$ denote a contour in the complex plane which begins at $z = \epsilon$, ends at $z = r$, and follows the real axis except for avoiding zeroes of $f(r)$ using semicircles of radius ϵ in the upper half plane. Since $f(r)$ is assumed analytic at its zeroes, $f(z)$ is well-defined on the contour for sufficiently small ϵ. This contour is depicted in figure 2.8.

The *global tortoise coordinate* r_* and *global tortoise function* $F(r)$ are defined

by

$$r_* = F(r) = \mathrm{Re} \lim_{\epsilon \to 0} \int_{C_{r,\epsilon}} \frac{dz'}{f(z')} \ . \tag{2.11}$$

Clearly this definition obeys the defining relation $F'(r) = f(r)^{-1}$. Within each interval I_j the tortoise function is monotonic and invertible, and we denote the inverse functions by $r = F_j^{-1}(r_*)$. The semi-circular contours each contribute the purely imaginary value $i\pi/k_i$ in the small ϵ limit. Thus $F(r_i + \epsilon') \approx F(r_i - \epsilon')$ for sufficiently small ϵ'.

It follows from the above considerations that (2.11) is approximated by

$$F(r) = \int_\epsilon^r \frac{dr'}{f(r')} \qquad\qquad (r \in I_0) \tag{2.12}$$

$$F(r) \approx F(r_j - \epsilon) + \int_{r_j+\epsilon}^r \frac{dr'}{f(r')} \qquad (r \in I_j) \ (j > 0) \tag{2.13}$$

with a small parameter $\epsilon > 0$. This form can be computed on a dense spacing of points by numerical integration. The forward and inverse functions can then both be approximated by linear interpolation. For improved numerical precision, it may be best to implement these formulae by integrating from some less extremal point in the interval, and matching boundary terms with additive constants. An example of the global tortoise function thus defined is given in figure 2.9.

By assumption, $f(r)$ is analytic and linear at each of its zeroes. This fact, in tandem with the definition (2.11), gives the global tortoise function two key properties. Most importantly, the expression

$$|f(r)| \, e^{-k_i F(r)} \tag{2.14}$$

is analytic and strictly positive in a neighborhood of $r = r_i$. This fact is essential

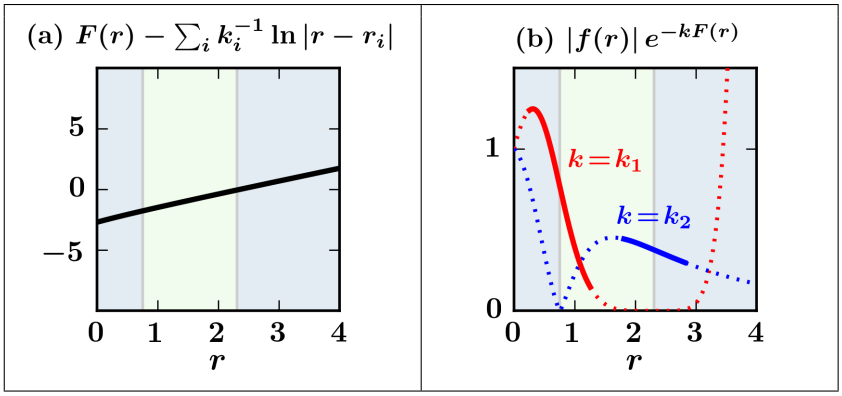

Figure 2.10: (Color online). Properties of the global tortoise function $F(r)$, for the same metric function $f(r) = 1 - 2.5\, r^2/(1 + r^3)$ shown in figure 2.9 above. (a) When the appropriate logarithmic infinities are subtracted out, a continuous function remains. (b) The function $|f(r)|\, e^{-k_i F(r)}$, which appears in the Penrose coordinate metric (2.23), is continuous and analytic at $r = r_i$. See section 2.5.1 for details.

for establishing that the metric is nondegenerate and continuous at the horizons; we will find that (2.14) appears explicitly in the Penrose coordinate metric (2.23). And secondly, the expression

$$F(r) - \tfrac{1}{k_i} \ln|r - r_i| \tag{2.15}$$

is analytic in a neighborhood of $r = r_i$. This result is of mainly conceptual importance, and relates closely to the first. These two properties can be understood by simple heuristic arguments in the real domain, and are also proved more rigorously in 2.12; they are demonstrated by example in figure 2.10.

Having defined the global tortoise function and determined its properties, the transformation to global Penrose coordinates can be undertaken.

2.5.2 Double-null and Penrose coordinates

The global tortoise function makes it possible to define Penrose coordinates $(\tilde{u}, \tilde{v})$ in which the metric is non-degenerate at the horizons. But to do so still requires that the coordinates be defined just right.

The approach given here differs in philosophy from the more well-known Kruskal method. There, the blocks are joined first and then all jointly squished. Here, instead, each block is squished individually, and the squished blocks are placed next to each other. This type of technique was pioneered by Carter [8]. The transformation in each block relies on an exquisite balance between arctangent compression and exponential expansion; when done right, a seemingly miraculous cancellation at the block boundaries renders the metric continuous.

First, the transformation to double-null block coordinates (u, v) proceeds in the standard way, utilizing the global tortoise function. In particular,

$$u = t - F(r) + c \,, \qquad v = t + F(r) - c \,. \tag{2.16}$$

The global parameter $c \in \mathbb{R}$ absorbs the global integration constant left in the tortoise function, and must be the same in every block. For the same reasons explained in section 2.4.4, the definition of (u, v) should have only the parameter c, and cannot be made more general by including other parameters.

The transformation from block to Penrose coordinates is then defined by

$$\tan \pi \, (\tilde{u} - \tilde{c}_u) = \epsilon_u \, h(u/2) \,, \qquad \tan \pi \, (\tilde{v} - \tilde{c}_v) = -\epsilon_v \, h(-v/2) \,. \tag{2.17}$$

The constants $\tilde{c}_u \in \mathbb{R}$ and $\tilde{c}_v \in \mathbb{R}$ locate the center of the block. The constants

$\epsilon_u = \pm 1$ and $\epsilon_v = \pm 1$ determine the block's orientation, and must obey

$$\epsilon_u \, \epsilon_v = \mathrm{sgn}(f). \tag{2.18}$$

The function h must be chosen carefully in each block, and is defined below. For notational purposes, h will be written as $h(s)$, with s a generic argument of no physical significance. The function $h(s)$ is referred to as the *pre-squishing function*, since it is applied to block coordinates before arctangent squishing functions are applied.

All that remains is to define the function $h(s)$ in each block. There is some amount of freedom in this definition, as discussed in more detail below. We take the definition

$$h(s) = h^{s_0}_{k_+,k_-}(s) = \begin{cases} -s_0 + H_{k_-}(s + s_0), & s < -s_0 \\ s, & |s| \leq s_0 \\ s_0 + H_{k_+}(s - s_0), & s > s_0 \end{cases}, \tag{2.19}$$

where

$$H_k(s) = \begin{cases} (e^{ks} - 1)/k & k \neq 0 \\ s & k = 0 \end{cases}, \tag{2.20}$$

with $s_0 \geq 0$ a parameter of the diagram construction, and with $k_+ \in \mathbb{R}$ and $k_- \in \mathbb{R}$ parameters determined by the metric function in the block. In particular, for a block on radius interval $I_j = (r_j, r_{j+1})$, the parameters are

$$k_- = \min(k_j, k_{j+1}), \qquad k_+ = \max(k_j, k_{j+1}), \tag{2.21}$$

where $k_0 = k_{N+1} = 0$ at $r_0 = 0$ and $r_{N+1} = \infty$, and $k_i = f'(r_i)$ at horizons (see

second half of section 2.4.3). Since by this prescription $k_- \leq 0 \leq k_+$, it is always true that $h(s)$ is continuous, differentiable, monotonic increasing, and unbounded as $|s| \to \infty$. Figure 2.9c shows an example of $h(s)$ for a particular block.

The parameters $k_\pm$ control the exponential behavior at the tails of $h(s)$. This behavior is essential to obtaining a continuous metric at the horizons. The setup is such that near each horizon radius r_i, the corresponding slope k_i controls the exponential transformation. Near $r = 0$ and $r = \infty$ there is no need to match the metric; recalling that, by definition, $k_0 = 0$ at $r_0 = 0$ and $k_{N+1} = 0$ at $r = \infty$ (end of section 2.4.3), one can see that $h(s)$ remains linear at these locations. Although the definitions ensure that $h(s)$ is everywhere continuous and once-differentiable, large values of $|k_\pm|$ cause a rapid exponential turn-on that appears similar to (but is not) a kink in the first derivative.

Whereas $k_\pm$ control the form of the exponential regions of $h(s)$, the parameter $s_0 \geq 0$ controls the location of the exponential regions in the diagram. As $s_0 \to \infty$, the exponential turn-ons are pushed arbitrarily far up against the horizons and into the corners of the diagram. As discussed in section 2.4.7, as $|t| \to \infty$ there must always be a neighborhood where the metric may be mismatched. The parameter s_0 controls the size of these neighborhoods: the metric is never discontinuous unless both $|u/2| > s_0$ and $|v/2| > s_0$. We typically choose s_0 such that the exponential regions are visible but not overwhelming in the diagram.

There is some amount of freedom to choose an $h(s)$. Only the monotonicity and asymptotic behavior at $s \to \pm\infty$ are absolutely essential. But choosing the function poorly can lead to difficult calculations and very ugly diagrams. The choice above is based on several additional criteria: (i) the function is continuous and once differentiable; (ii) lines of constant radius in the resulting diagram look natural; (iii) the function has a closed-form inverse; (iv) metric calculations are

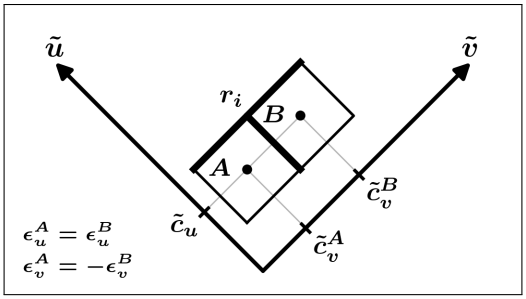

Figure 2.11: Illustration of the setup for joining neighboring blocks in the Penrose coordinates. See section 2.5.3. In the case depicted here, $x \equiv u$ and $y \equiv v$, so that the blocks are joined on a line of constant $\tilde{v}$. The bold boundary indicates horizons at the joining radius $r = r_i$.

relatively simple; and (v) issues near the points $|t| \to \infty$ are minimized.

Thus have the Penrose coordinates been constructed. The resulting metric is given in section 2.5.4. It remains only to show how the blocks should be matched up such that the Penrose metric is continuous and non-degenerate at horizons.

2.5.3 Joining blocks in Penrose coordinates

Two blocks can be joined along a horizon at $r = r_i$ if and only if the two blocks correspond to I_{i-1} and I_i. Let two such blocks be denoted B_A and B_B, respectively. The necessary parameter constraints for matching are determined by simple considerations. The setup is depicted in figure 2.11.

In order that the blocks be squarely aligned, it is necessary that either $\tilde{c}_u^B = \tilde{c}_u^A$ or $\tilde{c}_v^B = \tilde{c}_v^A$. For the horizons to intersect, the pair which is not equal must obey $|\tilde{c}_y^B - \tilde{c}_y^A| = 1$ (where y represents either u or v). We can therefore say that the blocks are shifted in the coordinate y, and aligned in the other coordinate x. The matched horizon then traces out a line of constant $\tilde{y}$ in the diagram. In order that the orientation of this horizon be preserved, it is necessary that $\epsilon_x^B = \epsilon_x^A$. But since the metric function switches sign in subsequent intervals, one obtains

the further requirement $\epsilon_u^B \epsilon_v^B = -\epsilon_u^A \epsilon_v^A$. This implies that $\epsilon_y^B = -\epsilon_y^A$ along the shifted coordinate. The only remaining parameter freedom is the sign of the above translation. In order to avoid introducing a time-orientation, this can be handled by simply stating that the matched horizons must be at an equal radius. This condition can be easily checked.

These requirements may be summarized as follows. Let B_A and B_B be blocks corresponding to I_{i-1} and I_i. The two blocks may be joined either along a line of constant $\tilde{u}$, or along a line of constant $\tilde{v}$. In order to treat both cases simultaneously, fix the symbols (x, y) to mean either (u, v) or (v, u) (see section 2.4.2). The blocks will be joined along a line of constant $\tilde{y}$. Then the blocks are properly matched at $r = r_i$ if:

(i) $\tilde{c}_x^A = \tilde{c}_x^B$ and $\epsilon_x^A = \epsilon_x^B$;

(ii) $\epsilon_y^A = -\epsilon_y^B$;

(iii) $|\tilde{c}_y^A - \tilde{c}_y^B| = 1$;

(iv) both intersecting horizons have the same radius $r = r_i$.

For a fixed orientation of B_A, this yields exactly two ways to attach B_B, corresponding to the choice of (x, y). In 2.12, it will be shown that these conditions suffice to ensure non-degeneracy of the metric.

2.5.4 Enumeration of the algorithm

All the ingredients are in place. In this section, we concisely summarize and enumerate the algorithm that has been presented for generating global Penrose coordinates $(\tilde{u}, \tilde{v})$ for an SSS spacetime with metric function $f(r)$.

Suppose M is an SSS spacetime with metric locally of the form

$$ds^2 = -f(r)\,dt^2 + f(r)^{-1}\,dr^2 + r^2\,d\Omega^2\ . \tag{2.22}$$

Assume the metric function $f(r)$ is once-differentiable, has a finite number N of zeroes on the interval $r \in (0, \infty)$, and that $\lim_{r\to 0} f(r) \neq 0$. Further, assume that $f(r)$ is analytic at each of its zeroes, although it may not be analytic globally, and that each zero is isolated and simple (linear).

The zeroes of $f(r)$ are denoted r_i for $i = 1, 2, \ldots, N$, and at each zero there is a slope $k_i = f'(r_i) \neq 0$. Additionally, denote $r_0 = 0$ and $r_{N+1} = \infty$, along with $k_0 = k_{N+1} = 0$. Then the radius values r_j, for $j = 0, 1, \ldots, N$, partition the radial coordinate into intervals $I_j = (r_j, r_{j+1})$, and in each interval I_j the sign of $f(r)$ is constant. Note that unlike k_i at the zeroes of $f(r)$, the values k_0 and k_{N+1} do not correspond to slopes, but are zero by fiat. This is because at r_0 and r_{N+1}, no horizon matching is needed.

First one must choose several global parameters associated with choices in the diagram construction. These control the appearance of the diagram. Additionally, the tortoise function $F(r)$, which determines the transformation into double null coordinates, must be defined globally in the correct way.

(i) Choose the global parameters $c \in \mathbb{R}$ and $s_0 \geq 0$.

(ii) Define the global tortoise function $F(r)$ by (2.11) as approximated by (2.12–2.13).

The parameter c absorbs an integration constant in the tortoise function and acts as a translation in the double null block coordinates. The parameter s_0 determines the location of exponential turn-ons in the piecewise function $h(s)$

below. Increasing s_0 pushes certain details into the corners of each block.

A block is specified by its interval $I_j = (r_j, r_{j+1})$. For each block in the diagram, appropriate block parameters must be chosen for the transformation to Penrose coordinates. For each block:

(iii) Let $k_- = \min(k_j, k_{j+1}) \leq 0$.

Let $k_+ = \max(k_j, k_{j+1}) \geq 0$.

(Recall that $k_i = f'(r_i)$ for $1 \leq i \leq N$ and $k_0 = k_{N+1} = 0$).

(iv) Choose block parameters $\tilde{c}_u, \tilde{c}_v \in \mathbb{R}$ and $\epsilon_u, \epsilon_v \in \pm 1$.

Ensure these are chosen such that $\epsilon_u \, \epsilon_v = \text{sgn}(f)$.

These control the location and orientation of a block.

Having set the parameters in each block, the transformation to double null coordinates (u, v), then to Penrose coordinates $(\tilde{u}, \tilde{v})$, can be defined. For each block:

(v) Let $h(s) = h^{s_0}_{k_+,k_-}(s)$ as defined by (2.19).

(vi) Let $u = t - F(r) + c$.

Let $v = t + F(r) - c$.

(vii) Let $\tan \pi \, (\tilde{u} - \tilde{c}_u) = \epsilon_u \, h(u/2)$.

Let $\tan \pi \, (\tilde{v} - \tilde{c}_v) = -\epsilon_v \, h(-v/2)$.

The coordinates $(\tilde{u}, \tilde{v})$ are now Penrose coordinates for each block by the definition of section 2.2. In order to ensure that the Penrose coordinates are global, parameters in each block must be compared.

(viii) Check that all adjacent blocks are properly matched according to the criteria listed at the end of section 2.5.3.

These conditions ensure that all blocks overlap only on the appropriate horizons, and that relative block orientations are correct.

The resulting metric in Penrose coordinates $(\tilde{u}, \tilde{v})$ is implicitly defined in terms of (u, v) and r by

$$ds^2 = -\left(\frac{4\pi^2}{e^{-kc}}\right) \frac{|f(r)|}{e^{kF(r)}}\ G_u(u,k)\ G_v(v,k)\ d\tilde{u}\, d\tilde{v} + r^2\ d\Omega^2 \tag{2.23}$$

where we have introduced a free parameter $k \in \mathbb{R}$, and

$$G_u(u,k) = e^{-ku/2}\ \frac{1 + h(u/2)^2}{h'(u/2)}, \tag{2.24}$$

$$G_v(v,k) = e^{kv/2}\ \frac{1 + h(-v/2)^2}{h'(-v/2)}\ . \tag{2.25}$$

The areal radius is given in each block by

$$r = r(\tilde{u}, \tilde{v}) = F_j^{-1}\left(\frac{v(\tilde{v}) - u(\tilde{u})}{2} + c\right)\ . \tag{2.26}$$

The metric (2.23) is independent of the free parameter k, which cancels out entirely when G_u and G_v are substituted back into the metric. Thus (2.23) holds for every $k \in \mathbb{R}$. The purpose of introducing artificial dependence on k is to make it easy to evaluate limits at each $r \to r_j$ by setting $k = k_j$. This trick works on both sides of every r_i (i.e. approaching r_i from blocks on I_i or I_{i+1}), due to the piecewise definition of $h(s)$ in each block. Note that with the appropriate substitution for k, the explicit function of radius appearing in the metric is equivalent to (2.14).

In the above form, all metric coefficients of $-d\tilde{u}d\tilde{v}$ and of $d\Omega^2$ are explicitly non-negative everywhere, and explicitly positive at all block points. In can be shown that these coefficients are also positive at horizon and horizon vertex points.

In 2.12 it is shown that this metric is continuous and nonzero everywhere, except along the polar coordinate singularity at $r = 0$, and except possibly in arbitrarily small corners of the diagram where $|u/2| > s_0$, $|v/2| > s_0$, and $|t| \to \infty$ (as discussed in section 2.4.7). Thus, the metric extends continuously and without degeneracy across all horizons and horizon vertices.

This form of the metric depends upon the Penrose coordinates only implicitly, through its dependence on (u, v) and r. This leaves the freedom to translate and flip blocks in the Penrose coordinates without a meaningful disturbance of the metric. Once the diagram is set and the blocks are matched, arbitrary monotonic functions $\tilde{u}'(\tilde{u})$ and $\tilde{v}'(\tilde{v})$ can be applied without compromising the Penrose coordinates; this usually just makes the diagram look worse, but is necessary in section 2.6.

2.6 Extension to piecewise-SSS spacetimes with null-shell junctions

In the astrophysical universe, spacetime is not strongly spherically symmetric – it is constantly, dynamically, evolving. Fortunately, many dynamical phenomena can be approximately modeled by spacetimes which are piecewise-SSS. Basic examples include stellar radiation, stellar collapse to a black hole, and the emission of Hawking radiation from a black hole.

The class of spacetimes treated in this section, which we refer to as *piecewise-SSS spacetimes with null-shell junctions*, is defined by having a finite number of SSS components, each joined together along null junction hypersurfaces. The junction hypersurfaces correspond to thin null shells of matter. These junctions

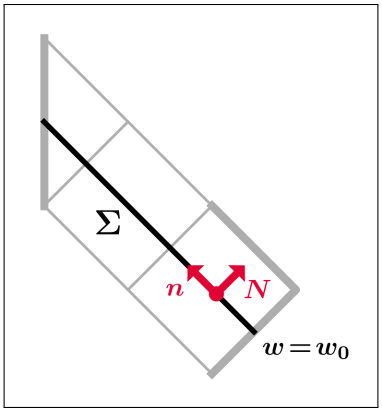

Figure 2.12: (Color online). Illustration of a radial null slice in SSS spacetime. The hypersurface Σ (black) lies on a surface of constant $w = w_0$. The vector n^a (red) is both normal and tangent to Σ, while the vector N^a (red) is transverse to Σ.

may have either the geometry of a single null shell (figure 2.13b), or of two null shells colliding at a corner (figure 2.13a). The full metric and other tensors are defined distributionally on the piecewise spacetime.

In this section we state the procedure necessary to construct piecewise-SSS spacetimes, making use of the Penrose coordinates previously identified. This immediately yields Penrose coordinates for the piecewise spacetime. First, we present the procedure for shell and corner junctions under the minimal requirement that junction shells have well-defined intrinsic geometry. Then, we determine the matter content of junction shells and discuss the conservation of energy.

This section is largely informed by the classic exposition of Barrabès and Israel [20], which is the standard reference for the analysis of thin shells and piecewise-defined spacetimes.

2.6.1 Geometry of a radial null slice in SSS spacetime

Consider an EF patch of an SSS spacetime, covered by the coordinates and metric (2.3). As usual, $\epsilon = \pm 1$ is the parameter appearing in the EF metric. Assume, without loss of generality, that ∂_w is future-directed. (This is general because $w \to -w$ with $\epsilon \to -\epsilon$ is an isometry of the EF patch.) With this convention, it follows that

$$\epsilon = 1 \quad \Longleftrightarrow \quad \partial_r \quad \text{future-directed}, \tag{2.27}$$

$$\epsilon = -1 \quad \Longleftrightarrow \quad \partial_r \quad \text{past-directed}, \tag{2.28}$$

and that $(\epsilon\, \partial_r)$ is always future-directed. This convention applies throughout section 2.6.

With this setup, a radial null slice Σ of the patch is defined as a hypersurface of constant $w = w_0$, as depicted in figure 2.12. Such a hypersurface is parameterized by the coordinates $x^i = (r, \Omega)$, and obtains the induced metric

$$ds^2 = r^2\, d\Omega^2 \tag{2.29}$$

in the coordinate basis.

A normal vector n^a and transverse null vector N^a to Σ can be defined (in the abstract index notation for spacetime tensors) by

$$n^a = \epsilon\, (\partial_r)^a\ , \qquad N^a = (\partial_w)^a - \tfrac{1}{2}\, \epsilon\, f(r)\, (\partial_r)^a\ , \tag{2.30}$$

such that $n_a n^a = N_a N^a = 0$ and $n_a N^a = -1$. Note that n^a and N^a are both future-directed. As usual for a null hypersurface, the normal vector is tangent to

Σ, and is a degenerate vector of $T_p\Sigma$ in the induced metric. This implies, as usual, that Σ has a geometrical dimension $D-2$ one less than its topological dimension $D-1$.

Before moving on, it worth noting that the normal and transverse vectors to Σ are eigenvectors of the stress tensor on the EF patch. At block points in the patch, the stress tensor $T^a{}_b = (1/8\pi)\, G^a{}_b$ is given in an ortho-normalized Schwarzschild coordinate basis by (2.62) of the appendix. This stress tensor has two degenerate eigenspaces. Using this fact, one can note without calculation that, at block points,

$$T^a{}_b\, n^b = -\rho\, n^a, \qquad T^a{}_b\, N^b = -\rho\, N^a\ , \tag{2.31}$$

since both n^a and N^a lie entirely in the (∂_t, ∂_r) plane. Direct calculation in the EF coordinates reveals that these same eigenvalue relations hold also at horizon points, and thus everywhere throughout the EF patch.

2.6.2 Algorithm for implementing corner and shell junctions

Four SSS (or piecewise-SSS) spacetimes can be joined together at a corner, which represents a pair of colliding null shells. The basic restriction for such a junction is that every point have a well-defined radius, so that the induced metric on the junction hypersurfaces is well-defined. Here we present a method for attaining a junction under this minimal condition. Later, more detailed conditions for energy conservation are given. For the sake of simplicity, in this treatment the corner junction point is always located at a block point. Although it is possible to locate the corner junction at a horizon or vertex point, to do so requires a separate treatment. Keep in mind that, despite the similarity in their schematic

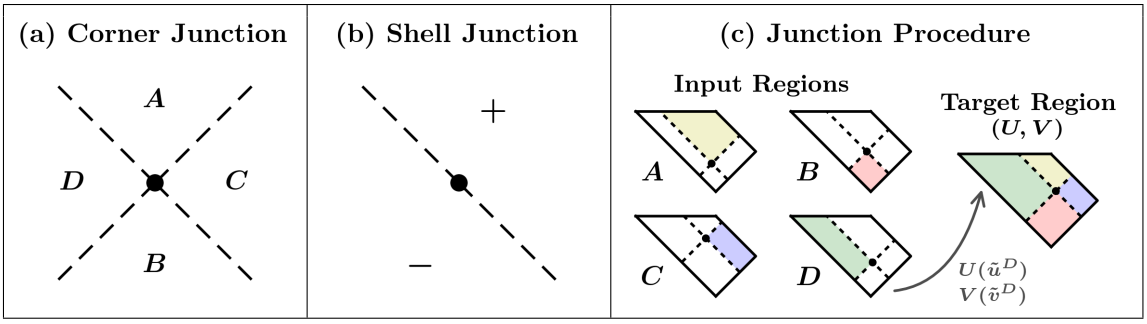

Figure 2.13: (Color online). Schematic depiction of corner and shell junctions. (a) The collision of two null shells at a corner point separates four SSS regions at a piecewise junction. In each of the four regions, the metric function $f(r)$ may be different. The corner point (black circle) has a well-defined radius, $r = r_0$, called the "corner radius". Note that, despite the similar schematic appearance, a corner point is *not* the same thing as a horizon vertex. (b) A null shell separates a past region ($-$) from a future region ($+$) at a piecewise junction. The shell junction is a special case of the more general corner junction. (c) Illustration of the procedure for creating properly matched junctions. Coordinates in the target region are denoted (U, V), and each input region has its own Penrose coordinate system $(\tilde{u}, \tilde{v})$. The appropriate subset of each input region is mapped into the target space by null transformations $U(\tilde{u})$ and $V(\tilde{v})$. These mappings must be self-consistent, such that every point on the junction hypersurfaces (dashed lines) has a well-defined radius. Compare to figure 2.18 for an implemented example.

illustrations, a corner junction point is *not* the same thing as a horizon vertex. Once the algorithm for corner junctions is established, the procedure for shell junctions follows as a special case.

Consider four SSS (or piecewise-SSS) regions, labelled A, B, C, D, and called the *input regions*, to be combined into a piecewise unit. Let each input region have Penrose coordinates $(\tilde{u}, \tilde{v}, \Omega)$. The input regions will be mapped into a *target space* representing the joint spacetime, as in figure 2.13. The coordinates of the target space we call (U, V, Ω). For each input region, the transformations $U(\tilde{u})$ and $V(\tilde{v})$ into the target space must be specified.

The procedure by which the input regions are joined can be stated simply: each input region must be sliced along null junction surfaces in the u and v directions,

then stretched and shifted in the u and v directions such that the radii at junction surfaces are all matched up. This procedure is illustrated schematically in figure 2.13c. A precise formulation of the procedure is as follows.

First, one must choose null slices in each input region to act as the junction hypersurfaces. This amounts to choosing values $\tilde{u}_0$ and $\tilde{v}_0$ in each (the values in each region may be distinct). Junction slices are then located at $\tilde{u} = \tilde{u}_0$ and $\tilde{v} = \tilde{v}_0$, with the corner point located at the intersection $(\tilde{u}_0, \tilde{v}_0)$. The values must be chosen consistently, such that the corner points for each input region have the same radius $r_0 = r(\tilde{u}_0, \tilde{v}_0)$. We call this shared radius the *corner radius*.

With the junction hypersurfaces consistently defined in the input regions, one is free to define an arbitrary radial parameterization of the junction hypersurfaces in target coordinates. This is done by specifying two arbitrary monotonic functions $U_0(r)$ and $V_0(r)$. Each input region will be mapped into the target region so that the radii match these functions on the junction surfaces. The corner point will therefore attain the coordinates $(U_0(r_0), V_0(r_0))$ in target coordinates.

Having achieved this setup, the transformation of each input region into target space coordinates is given by

$$U(\tilde{u}) = U_0\Big(r(\tilde{u}, \tilde{v}_0)\Big), \qquad V(\tilde{v}) = V_0\Big(r(\tilde{u}_0, \tilde{v})\Big). \tag{2.32}$$

When junction slices cover less than the entire domain of $\tilde{u}, \tilde{v}$ values, the above transformations may be extended by an arbitrary monotonic extrapolation. The transformations ensure that the radii $r(U, V_0(r_0))$ and $r(U_0(r_0), V)$ are well-defined regardless of the region of evaluation. Moreover, a simple chain rule calculation leveraging the results of sections 2.5.1 and 2.5.2 reveals that when the input regions are SSS, the junction slice radii $r(\tilde{u}, \tilde{v}_0)$ and $r(\tilde{u}_0, \tilde{v})$ are monotonic functions. This

implies that whenever $U_0(r)$ and $V_0(r)$ are monotonic, the target-space metric components for each input region are regular and nonzero. This ensures that the transformations (2.32) will yield Penrose coordinates for the joint spacetime. Furthermore, it follows from the chain rule that $r(U, V_0(r_0))$ and $r(U_0(r_0), V)$ are monotonic functions in the target coordinates. Thus even when the input regions are themselves piecewise-SSS, the above procedure yields Penrose coordinates in the target space.

The full metric of the joint spacetime is defined piecewise in terms of the input region target-space metrics; it can be written distributionally using Heaviside Θ-functions. The arrangement is depicted in figure 2.13a. With this setup, the induced metric on the junction hypersurfaces is $ds^2 = r^2\, d\Omega^2$. Since the radii at these hypersurfaces has been properly matched, the geometry of the joint spacetime is well-defined and non-degenerate. The coordinates (U, V, Ω) are Penrose coordinates, and our theory of corner junctions is complete.

A shell junction can be regarded as a special case of the corner junction, in which two pairs of the input spacetimes are identical. In such a case, all the above considerations remain valid. Additionally, for a shell, radius matching in either the U or V direction becomes trivial (depending on the direction of the shell), so that one of the transformations in (2.32) can be replaced by $U(\tilde{u}) = \tilde{u}$ or $V(\tilde{v}) = \tilde{v}$, or some other monotonic function, if desired.

This procedure achieves our goal of constructing a composite spacetime under the minimal junction condition.

2.6.3 Matter content at shell junctions

In order to analyze the matter content at a shell junction generated by the above algorithm, it is easiest to work in local EF coordinates of the type set up in section 2.6.1, rather than in the Penrose coordinates of the previous section. Suppose we focus on a local patch M_0, which is separated into a past region M_- and future region M_+ by the null junction hypersurface Σ, with the metric functions $f_\pm(r)$ in the two regions. Each of $M_\pm$ can be expressed in terms of EF coordinates, with metric of the form (2.3), such that Σ lies on a line of $w = const$ in each region, and such that $\epsilon_+ = \epsilon_-$. It is therefore possible to choose a joint coordinate system (w, r, Ω) on M_0, such that Σ is defined by the level set $\Phi = w = 0$, and such that the metric is (2.3) with metric function $f(r) = f_\pm(r)$ in the appropriate regions. In accordance with section 2.6.1 and the requirements of [20], the metric parameter $\epsilon = \pm 1$ indicates the future-/past- directedness of ∂_r, the normal and transverse vectors n^a and N^a are future-directed, and the level set function $\Phi = w$ increases toward the future.

In order to conveniently express the stress tensor, let us define the mass function $m(r)$ by $f(r) = 1 - 2\,m(r)/r$, and define the mass jump $[m(r)] = m_+(r) - m_-(r)$. Note that no restriction on $m(r)$ is implied — it is simply a useful way to write the metric function. Then, in the joint EF coordinate system described above, the stress tensor associated with the junction shell may be read off from [20, (s. II, IV)]. In the abstract index notation for spacetime tensors (as opposed to the notation convention of [20], which uses latin indices for hypersurface coordinates), it reads

$$T^{ab}_\Sigma = \sigma\, n^a n^b\, \delta(w), \qquad \sigma = (-\epsilon)\, \frac{[m(r)]}{4\pi r^2}\,, \tag{2.33}$$

where $n^a = \epsilon\,(\partial_r)^a$ is both normal and tangent to the shell, the metric parameter $\epsilon = \pm 1$ indicates an outgoing $(+)$ or ingoing $(-)$ shell (see sec 2.6.1), and $\delta(w)$ is the Dirac δ-distribution.

The coefficient σ may be thought of as the surface energy density of the shell, up to an arbitrary normalization factor associated with the null vector n^a. A more physical quantity is the surface energy density relative to an observer with future-directed timelike tangent vector t^a, which is given by $\sigma_t = (n_a t^a)^2\ \sigma$. Evidently the sign of σ is physically meaningful: timelike observers measure a positive energy density if and only if $\sigma > 0$. Indeed, one can show that when $\sigma < 0$ the null, weak, and dominant energy conditions are violated, and the energy flux vector (relative to a future-directed timelike observer) is past-directed null. It is therefore sensible to say that shells with $\sigma < 0$ have *negative mass*, while shells with $\sigma > 0$ have *positive mass*. The sign of σ is a local property, and in principle (in physically unusual cases) a single shell may have positive and negative mass at different points.

For the junction of two patches of Schwarzschild spacetime, the mass jump is a constant value Δm; the positive mass shell scenarios ($\sigma > 0$) for this case are depicted schematically in figure 2.14. If the inequalities in the figure were reversed, the junction would yield a shell with negative mass.

2.6.4 Energy conservation at shell and corner junctions

Local conservation of energy and momentum in General Relativity is expressed by the relation $\nabla_a T^{ab} = 0$. For any smooth metric, the contracted Bianchi identities provide $\nabla_a G^{ab} = 0$, ensuring energy conservation by way of Einstein's equation. When the metric is not differentiable, the standard derivation of the

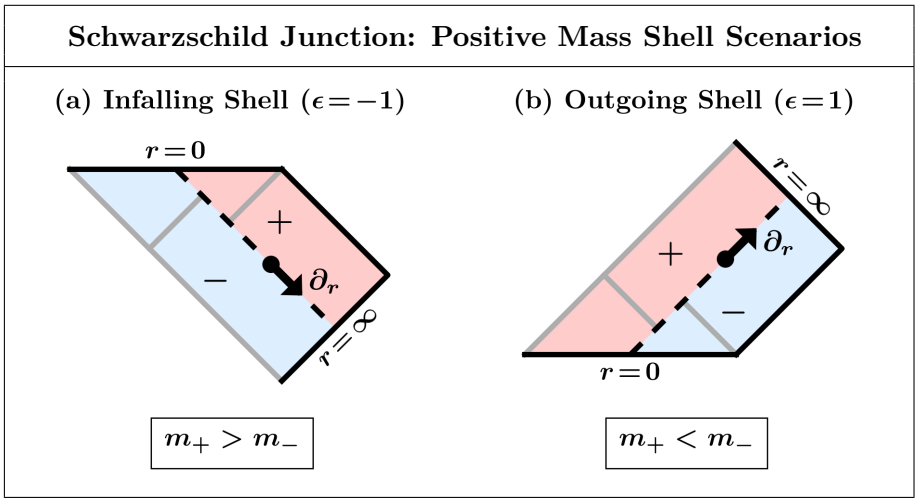

Figure 2.14: (Color online). Illustration of the possible scenarios for joining two Schwarzschild spacetimes across a positive-mass shell (i.e. a shell with $\sigma > 0$, see section 2.6.3). The junction shell Σ (dashed black line) separates the joint spacetime into future (red fill, labelled "+") and past (light-blue fill, labelled "−") regions. The parameter $\epsilon = \pm 1$ is determined by the future-/past- directedness of ∂_r, while the normal vector $n^a = \epsilon\,(\partial_r)^a$ (not shown) is always future-directed. As expected, an infalling (outgoing) positive-mass shell necessarily increases (decreases) the mass m_+ of the future region. This change is reflected by a shift in the horizons (gray lines) at $r = 2m$ in each region.

Bianchi identities does not hold up. So the question remains: for the piecewise case, does local energy conservation hold everywhere as a distributional identity?

For the case of shell junctions, it has been shown by Barrabès and Israel [20, (eqns. A10 - A13)] that $\nabla_a G^{ab} = 0$ does indeed hold as a distributional identity. It is therefore true that, without any further constraints, the joint spacetime produced by our junction algorithm is automatically energy conserving at all shell junctions. In context of our junction algorithm, every junction is locally a shell junction except at the corner points $(U_0(r_0), V_0(r_0))$ in the target coordinates. So the only remaining question is that of energy conservation at the corner points.

At corner points, the question of energy conservation is slightly more complicated, but there is nonetheless a well-established theory [20, 21, 22, 23]. In order that conservation hold at a corner point with radius r_0, the metric functions of the four input regions must satisfy the DTR (Dray - 't Hooft - Redmount) relation [23]

$$f_A(r_0)\, f_B(r_0) = f_C(r_0)\, f_D(r_0)\ , \tag{2.34}$$

with the region labels defined by figure 2.13a. This formula encodes a relativistic version of conservation of mass in the shell collision. Note that when shell junctions are regarded as a special case of corner junctions, the DTR relation is satisfied trivially. It is well known that the DTR relation is necessary for energy to be conserved, and general consensus of the standard treatments of shell collision (cited above) suggests that the relation is also sufficient. However, the authors are not aware of an explicit proof that the distributional equation $\nabla_a G^{ab} = 0$ holds at corner points when DTR is satisfied.

2.7 Implementation and examples

The methods described in this article have been implemented in a package called `xhorizon` for Python 2.7. Source code for the implementation is available from the authors.

Examples generated by the implementation are given in figures 2.15–2.18 (located after the end of the text but before the appendix). Figure 2.15 depicts example diagrams for SSS spacetimes. Figure 2.16 shows a detailed zoom view of a particular diagram. Figure 2.17 helps elucidate generic features of the diagrams resulting from these methods. And figure 2.18 gives example diagrams for piecewise-SSS spacetimes resulting from null shell junctions.

Features of the examples and implementation are described in captions of the example figures, since they are best understood in context of the results. Just a few further comments are in order here.

The first comment regards the SSS diagrams. Comparison between the extended Schwarzschild diagram in figure 2.15b and the Reissner-Nordstrom (R-N) diagram in figure 2.15d is immediately striking: for all lines of constant radius on the length scale of the outer horizon radius, the two diagrams are nearly identical. They differ only at length scales on the order of the R-N inner horizon radius. The R-N diagram appears, in fact, as a Schwarzschild diagram with the $r = 0$ singularity "rigidly pulled up" to become timelike. This is consistent with the generic effects of "bunching" and "repelling" described in figure 2.17. Due to the large value of $|k_i|$ at the inner horizon, the upper square (between green bunches) of the R-N diagram is almost all located at the inner horizon radius plus or minus "epsilon", while all reasonably spaced lines of constant radius are bunched at the edges. When the R-N spacetime becomes highly charged (nearly extremal), as in

figure 2.15c, these effects are mitigated.

The second regards energy conservation in the piecewise-SSS diagrams. Notably, there is no obviously visible difference between the energy conserving junction in figure 2.18a–b and the energy non-conserving junction in figure 2.18c–d. The DTR relation must be independently verified. Moreover, energy conservation by the DTR relation is not always intuitive; even in the energy conserving Schwarzschild example of figure 2.18a–b, the total incoming and outgoing shell masses do not add up in the naive way. Heuristically, this is because the DTR formula must take gravitational potential energy into account [23].

For more general remarks, see the captions of figures 2.15–2.18.

2.8 Concluding remarks

We have given a complete analysis of the theory of Penrose diagrams as applied to strongly spherically symmetric spacetimes and their piecewise-SSS cousins. Having set down the rules, these methods may be used to analyze causal structure in a broad class of spacetimes. In a forthcoming publication, these methods will be applied to the case of a black hole which forms from stellar collapse and subsequently evaporates by emitting Hawking radiation.

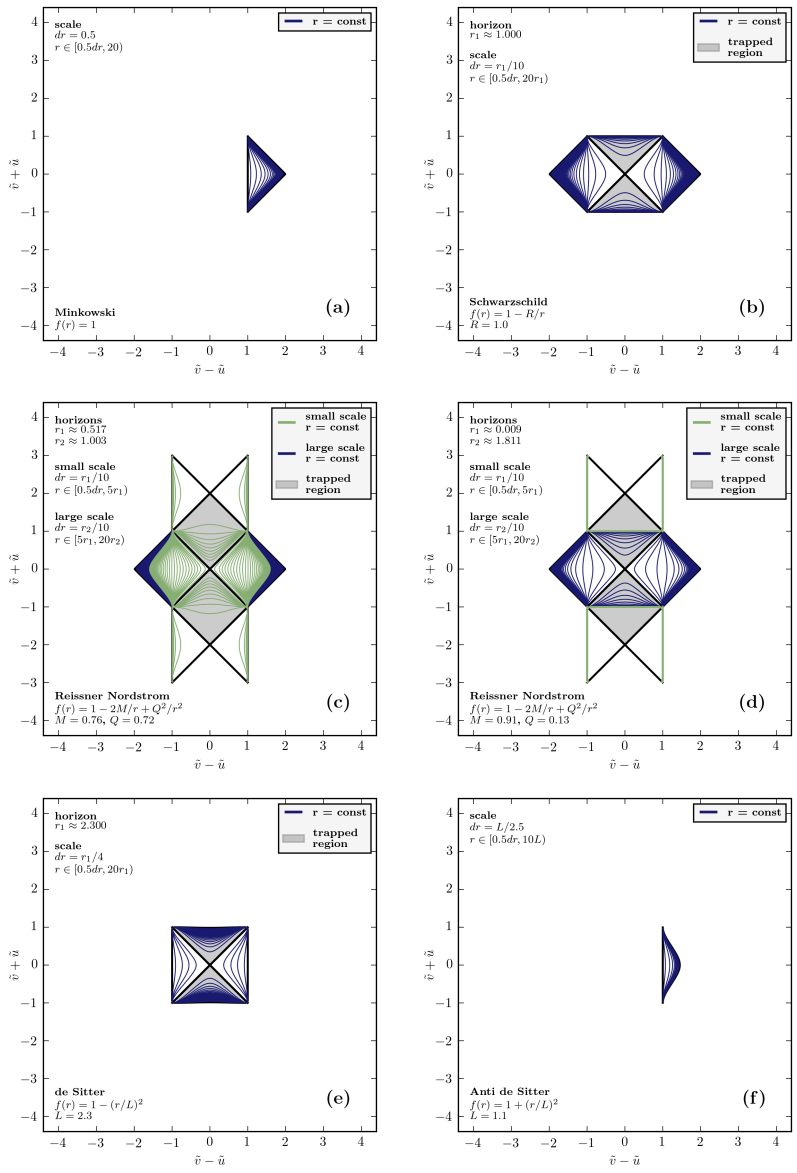

Figure 2.15: (Color online). Example SSS diagrams generated by an implementation of the methods described in this article. For each diagram, lines of constant radius are given at various length scales. For parameters and line spacing scales see diagram annotations. All these diagrams utilize the global diagram constants $c = 0$ and $s_0 = 10$ (see section 2.5). (a) Minkowski spacetime. (b) Schwarzschild black hole. (c) Highly charged (nearly extremal) Reissner-Nordstrom black hole. (d) Reissner-Nordstrom black hole with small charge. (e) de Sitter spacetime. (f) Anti de Sitter spacetime.

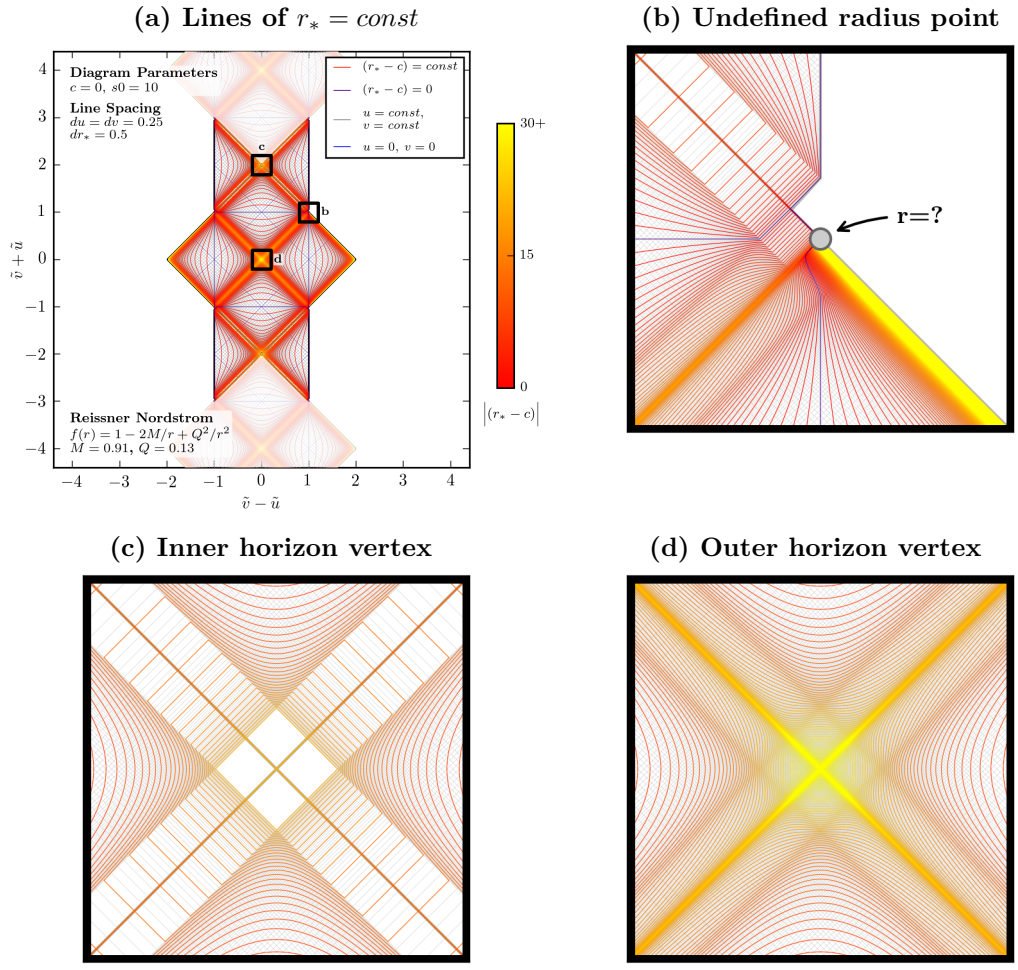

Figure 2.16: (Color online). Diagram and detail views of the same Reissner-Nordstrom spacetime from figure 2.15d above. Evenly spaced lines of constant tortoise coordinate $r_* = const$ (orange color scale) provide a different perspective from the previously shown lines of constant radius. Each of the panels (b,c,d) provides a zoom view of the corresponding labeled box in (a). A periodic continuation of the central region is shown in faded color in panel (a), but in full color in the zoom panel (c). Some curves in the detail views may appear to have discontinuities or numerical precision jumps, but this is not the case. In fact, all the visible curves are once-differentiable, numerically accurate, and numerically well-resolved. Apparent kinks and discontinuities are due to turn-on of exponential behavior in the piecewise function $h(s)$ (see section 2.5.2); these turn-ons occur when $|u/2| > s_0$ and when $|v/2| > s_0$. Near the inner horizon in panel (c), all reasonably spaced lines of $r_* = const$ in the exponential region are squished against the horizons and into the corner, due to the large magnitude of the slope $k_i = f'(r_i)$ at the inner horizon radius. [Caption continued on next page...]

Figure 2.16: [...Caption continued from previous page.] More gradual deformations near the outer horizon in panel (d) correspond to a less extreme value of the slope. Near the undefined radius point in panel (b), the Penrose coordinate metric is discontinuous across the horizon within the diamond defined by $|u/2| > s_0$ and $|v/2| > s_0$ (see section 2.4.7). Changing the parameter s_0 moves the location of the exponential turn-ons. As $s_0 \to \infty$, these features are pushed arbitrarily far against the horizons and into the corners.

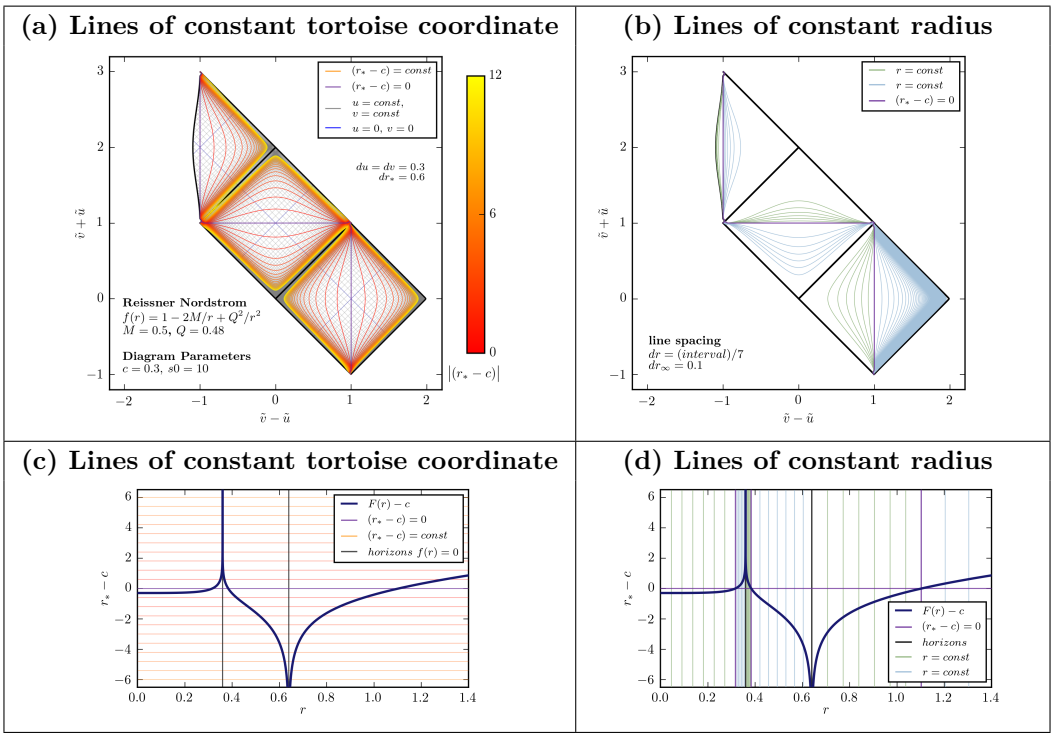

Figure 2.17: (Color online). Generic features of these diagrams can be understood by inspecting the relationship between lines of constant radius r and lines of constant tortoise coordinate $r_* = F(r)$. In this example, all four panels correspond to an EF patch of a Reissner Nordstrom spacetime, with parameters as given in panel (a). Panels (a) and (b) respectively show lines of constant r_* and r in the diagram. Panels (c) and (d) depict the same lines against graphs of $F(r)$. The interval boundaries in (b,d) occur wherever either $f(r) = 0$ or $F(r) - c = 0$, and there are six equally spaced lines of constant radius in each interval (except in the last interval where $dr = 0.1$ as $r \to \infty$). Observing panel (a) highlights some features which are generic to the method: the line $F(r) - c = 0$ always runs straight through the middle of each block, and the lines of $r_* - c = const$ have a regular and predictable spacing in the diagram. These may be used as a regularly spaced reference for sketching block boundaries and lines of constant radius. Comparing to the graph of $F(r)$ in panel (c), one observes that within each interval, most radius values lie in a small range of r_* values, with most of the range of r_* lying arbitrarily close to a horizon. [Caption continued on next page...]

Figure 2.17: [...Caption continued from previous page.] This property is generic when horizons are present, and leads to a "bunching up" of lines of constant radius, since sampled values of radius generally lie in a small interval of r_*. This bunching is visible in panels (b,d), where lines of constant radius are evenly spaced within each individual interval, but remain bunched in the diagram nonetheless. Less carefully sampled radius values will generally be even more bunched than these, and bunching is stronger near horizons with large $|k_i|$. Horizons with large $|k_i|$ thereby "repel" lines of $r = const$ and take up a large effective space in the diagram. Changing the parameter c moves all bundles simultaneously while maintaining relative positions. Note also the location of the block boundary at $r = 0$ (top left boundary). Since $F(0) = 0$ always, when $c = 0$ this boundary will be a straight line at $F(r) - c = 0$. In the present case $c > 0$, and the boundary is pushed out to the left of vertical.

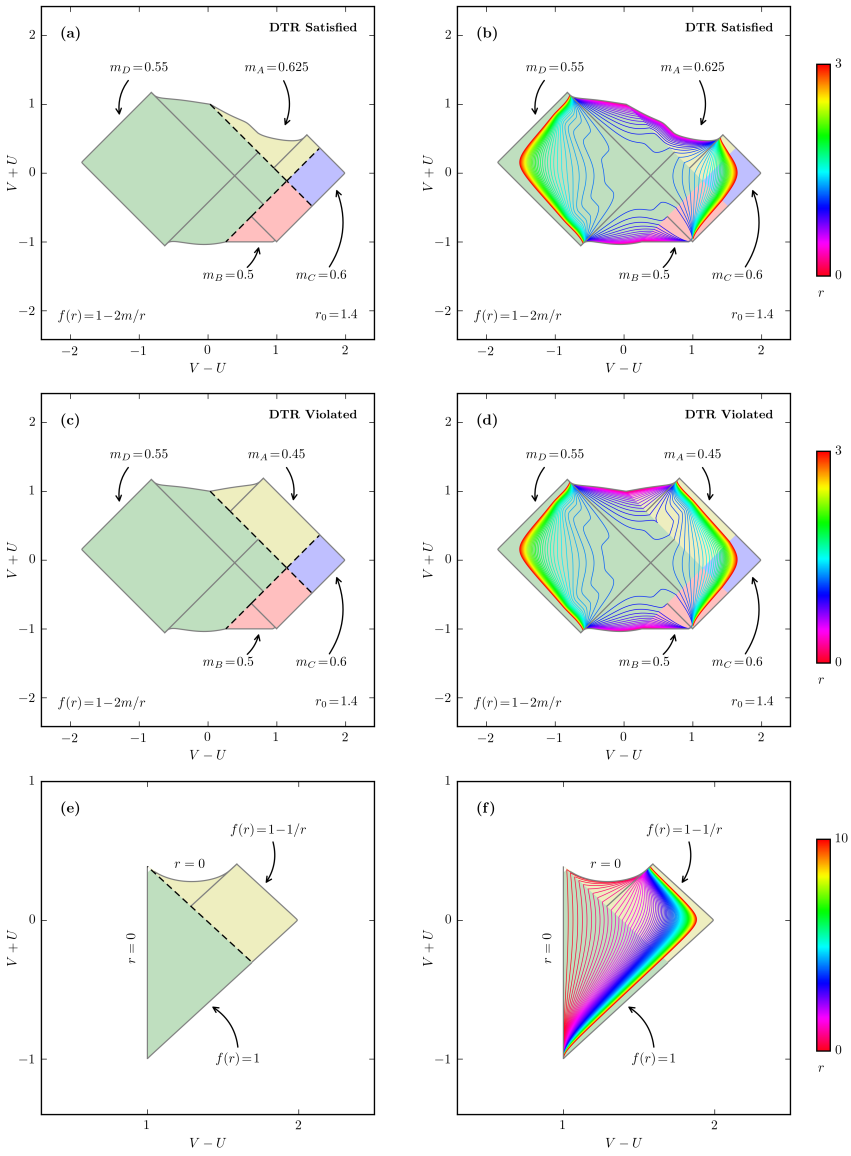

Figure 2.18: (Color online). Example piecewise-SSS diagrams generated by an implementation of the methods described in this article. Diagram constants set to $c = 0$ and $s_0 = 10$. In each row, left and right panels show the same example with different features. Left panels show conformal boundaries (gray lines), horizons (gray lines), and junction hypersurfaces (black dashed lines). Right panels show lines of constant radius (color scale). Each line of constant radius is continuous at all junctions, and obtains an unusual wiggly appearance from the junction matching transformations. Panels (a,b) show four SSS regions joined at an energy-conserving corner junction. Panels (c,d) are similar to (a,b), but with DTR violated (energy not conserved). Panels (e,f) show a Schwarzschild black hole forming from shell collapse in Minkowski space.

2.9 Appendix: Comparison to existing methods

The method described in this article generalizes and unifies techniques from various sources. In order to provide the proper context, we conduct here a brief review of the methods historically used to create similar diagrams.

The problem of generating causal diagrams for SSS spacetimes has previously been tackled in two fundamental ways: the method of block diagrams and the method of global Penrose coordinates. The block diagram method provides explicit global Penrose coordinates only when the metric function has one or zero horizon radii (locations where $f(r) = 0$). When many horizons are present, the block diagram method allows qualitative analysis by the identification of overlapping blocks in neighboring quad-block regions (see section 2.4), but does not define a self-consistent system of global coordinates in the area of overlap.

The more well known of the two methods is that of block diagrams, in which the causal structure of spacetime is pieced together from quad-block units. This method was first applied to the special case of Schwarzschild spacetime by Kruskal [24]. Maximally extended Schwarzschild spacetime, with its one horizon radius, consists of a single quad-block, and so in this case global Penrose coordinates were also achieved. Kruskal's method was then generalized by Walker to the method of block diagrams [9]. In Walker's treatment, quad-blocks could be constructed so long as the metric function took a special form, with the tortoise function defined by an indefinite integral (although definite integrals were implemented to generate the tortoise function within individual blocks). Later, however, Brill and Hayward [25] used a definite integral formulation to extend Walker's method to the case of an arbitrary metric function, in a manner equivalent to the results of section 2.4.5. In this way, the question of constructing

arbitrary block diagrams (but not Penrose diagrams) for SSS spacetimes has long since been settled.

The less well known set of methods is that in which global Penrose coordinates are explicitly constructed. The most important progress in this direction was made by Carter [8], who found global Penrose coordinates for special cases with two horizons. Although Carter's method relied on the ability to determine the tortoise function by an indefinite integral, and assumed the existence of exactly two horizons, it is in fact easily generalizable, and was the most important contribution to the present methods. In fact, when the indefinite integral form of the tortoise function is known, Carter's two-horizon method is essentially equivalent to the method of section 2.5, but with the substitution $h^{s_0}_{k_+,k_-}(s) = e^{2k_+ s} - e^{-2k_- s}$ in every block. The original Carter method does have several drawbacks. One is that the exponential form of $h(s)$ yields very strange-looking lines of constant radius (see figure 2.19). Additionally, applied to a case with more than two horizons, this method would suffer from major problems near the undefined radius points (see section 2.4.7), and need to be modified. The results of section 2.5 can be thought of as a generalization of the methods of Carter; the key new additions are the introduction of the global tortoise function and the new form of the function $h^{s_0}_{k_+,k_-}(s)$. These additions allow the method to be extended to an arbitrary metric function with an arbitrary number of horizons, while simultaneously rendering the diagram more readable.

In order to understand the advantages of the present method, it is useful to compare the known methods for constructing Penrose diagrams in the case of two horizons. Such a comparison is depicted in figure 2.19. Once the tortoise function $F(r)$ is set and the double-null coordinates (u, v) are defined in each block, there are several known methods of obtaining the diagram coordinates.

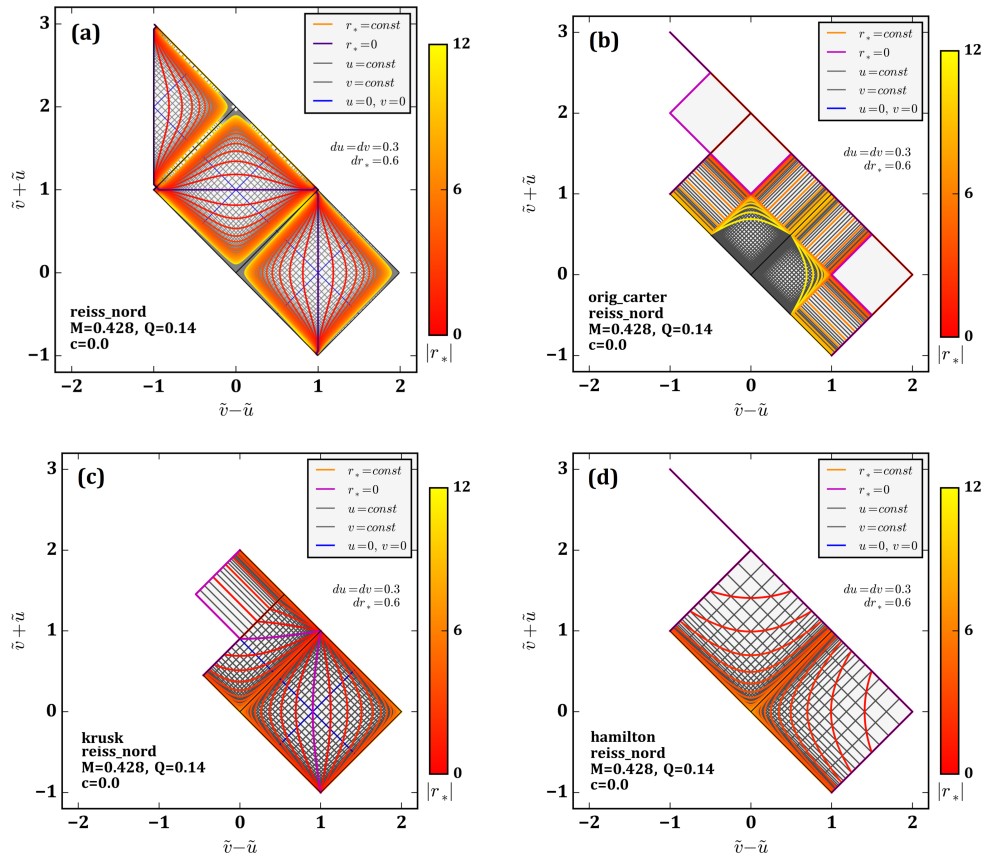

Figure 2.19: (Color online). An EF region for a Reissner-Nordstrom black hole, generated according to four different methods. In order to emphasize the effects of each transformation, lines of constant tortoise coordinate r_*, rather than constant radius, are shown. (a) The algorithm of section 2.5, with $s_0 = 10$. (b) The method described by Carter in 1966 [8]. (c) A method which is adapted from the Kruskal method to allow two horizons. (d) A method due to Hamilton [11]. In all cases the preliminary transformation to double null coordinates (u, v) utilizes the constant $c = 0$.

First, of course, there is the method of section 2.5. Second, there is the original method of Carter [8]. Both have been described above. A third method has been used by Hamilton [11]; this method could potentially also be generalized, but is less theoretically appealing than Carter's method. Finally, it is possible to define a two-horizon extension of the Kruskal method such that the diagram matches the standard Kruskal diagram outside of some inner limit; this two-horizon Kruskal-like method cannot be extended to more horizons, however, and so although it is shown for comparison, we omit its exact formulation. In figure 2.19, diagrams featuring lines of constant tortoise coordinate r_* are shown for each of these four methods. Showing the tortoise coordinate instead of radius isolates the effect of the different coordinates systems, eliminating distortion due to $F(r)$.

2.10 Appendix: Unit conventions

A major goal of the techniques described in this article is to realize Penrose diagrams of physically relevant spacetimes. As such, we must clarify the status of units in these calculations. First of all, note that we utilize standard conventions for geometrized units, such that $G = c = 1$, in accordance with [26, (Appendix F)]. The tricky issue of units in the coordinates, metric components, and Penrose diagrams is discussed below.

In GR the units of the line element are necessarily $[ds^2] = [\text{length}]^2$. Units for other geometric quantities depend on a choice of convention. Among the possible conventions, there is a unique simplest choice: all metric components $g_{\mu\nu}$ should be unitless, while all coordinates carry units of length. This convention has several benefits. All components of a tensor have the same units. The components of an even-rank tensor have the same units as its scalar contractions. And for

any given tensor, the covariant, contravariant, and mixed varieties all have the same units. In particular the Ricci curvature components and Ricci scalar obey $[R^{\mu}{}_{\nu}] = [R_{\mu\nu}] = [R^{\mu\nu}] = [R] = [\text{length}]^{-2}$, and after conversion to SI units by $\bar{T}_{\mu\nu} = (c^4/G)\, T_{\mu\nu} = (c^4/8\pi G)\, G_{\mu\nu}$ all components of the stress-energy tensor have units $[\bar{T}_{\mu\nu}] = [\text{energy}]\,[\text{length}]^{-(D-1)}$ (where D is the number of spacetime dimensions). There are other standard unit conventions in which these need not hold. For example in the standard Euclidean spherical coordinates $(\bar{r}, \theta, \phi)$ where $[\bar{r}] = [\text{length}]$ and $[\theta] = [\phi] = [1]$, the components $T_{\mu\nu}$ do not even all have the same units.

We achieve this simplest convention while maintaining notational simplicity by factoring out and suppressing a universal length scale. Let the physical line element $d\bar{s}^2 = \bar{g}_{\mu\nu}\, d\bar{x}^{\mu} d\bar{x}^{\nu}$ have any arbitrary unit convention such that $[d\bar{s}^2] = [\text{length}]^2$. Let l be an arbitrary length scale. It is always possible to nondimensionalize the coordinates and metric components to obtain $d\bar{s}^2 = l^2\, ds^2$ with $ds^2 = g_{\mu\nu}\, dx^{\mu}\, dx^{\nu}$, where $[ds^2] = [g_{\mu\nu}] = [dx^{\mu}] = [x^{\mu}] = [1]$. Then the physical line element can always be expressed as $d\bar{s}^2 = g_{\mu\nu}\, d(lx^{\mu})\, d(lx^{\nu})$ in terms of the unitful coordinates (lx^{μ}) and the unitless metric. This form of the physical line element satisfies the desired convention.

We will always write the unitless line element ds^2 in the unitless coordinates x^{μ} as a shorthand for the true line element $d\bar{s}^2 = l^2\, ds^2 = g_{\mu\nu}\, d(lx^{\mu})\, d(lx^{\nu})$ in the unitful coordinates (lx^{μ}), never making the arbitrary length scale explicit. Note that derivatives $\partial_{lx^{\mu}} = l^{-1}\, \partial_{x^{\mu}}$ pick up an extra factor of the length scale when calculating in the shorthand. By keeping track of these and similar factors, one can easily relate geometric quantities in the unitful geometry to those in the unitless geometry.

Additionally, all parameters in the metric components are by convention unit-

less. Any physical, unitful, parameters must be obtained by studying the resultant geometry of the physical metric $d\bar{s}^2$.

Consider the demonstrative example of three dimensional Euclidean flat space in spherical coordinates. We write this geometry in the unitless shorthand coordinates (r, θ, ϕ), with line element $ds^2 = dr^2 + r^2\,(d\theta^2 + \sin^2\theta\, d\phi^2)$. This serves as shorthand for the the unitful coordinates $\bar{x}^\mu = (lr, l\theta, l\phi)$, and the unitful metric $d\bar{s}^2 = d(lr)^2 + (lr/l)^2\,(d(l\theta)^2 + \sin^2(l\theta/l)\, d(l\phi)^2)$, with $l\theta \in (0, \pi l)$ and $l\phi \in (0, 2\pi l)$.

Moreover, to see how parameters in the metric correspond to physical parameters, consider for example the Schwarzschild metric $ds^2 = -(1 - R/r)\, dt^2 + (1 - R/r)^{-1}\, dr^2 + r^2\, d\Omega^2$, as expressed here in the unitless shorthand coordinates. The parameter R is unitless. By inspection of the geometry $d\bar{s}^2$, one finds that the physical Schwarzschild radius is $\bar{R} = Rl$, and the physical Schwarzschild mass in SI units is $\bar{M} = Rlc^2/2G$.

The Penrose diagrams we construct are for the unitless metric ds^2. The Penrose coordinates are unitless, and in all examples no absolute length scale appears in the metric components. Consequently, the appearance of the Penrose diagrams never depends on the arbitrary length scale factor. To return to units, one simply notes that if (u, v) are Penrose coordinates for ds^2, then (lu, lv) are Penrose coordinates for $d\bar{s}^2 = l^2 ds^2$. Once the length scale l is set, all lengths are defined in units, and other geometrical quantities must be calculated in units as described above.

2.11 Appendix: Spherical symmetry with a fixed origin

To properly describe SSS spacetimes requires the concept of spherical symmetry about a fixed origin. Since manifolds need not contain their symmetry axes, this requires a bit of extra work.

To set the stage, let us recall some facts about the symmetry of psuedo-Riemannian manifolds (i.e. metric manifolds of arbitrary signature). Such a D-dimensional manifold M usually has a continuous (Lie) group $\mathcal{G}$ of isometries. Continuous isometries are generated by flow along Killing vector fields, which satisfy $\nabla_{(a}k_{b)} = 0$. The set of Killing vector fields, under the Lie bracket operation, form a Lie algebra equivalent to that of $\mathcal{G}$. The maximum number of independent Killing vector fields (maximum dimension of $\mathcal{G}$) is always $D\,(D+1)/2$. Spaces saturating this maximum are maximally symmetric, have constant curvature, and are homogenous and isotropic, at least locally [27]. In particular the k-sphere $\mathbb{S}^k$, with metric induced from Euclidean space, is a maximally symmetric space of positive curvature. The isometry group of $\mathbb{S}^{k-1}$ is the orthogonal group $O(k)$, defined as the Lie group of real orthogonal $k \times k$ matrices. The corresponding Lie algebra $\mathfrak{so}(k)$, defined as the real algebra of real antisymmetric $k \times k$ matrices, has dimension $k\,(k-1)/2$. It is by analogy with this symmetry algebra that we define spherical symmetry in spacetime.

Let M be a spacetime of dimension D. M is called *n-spherically symmetric* if (i) the Lie algebra of Killing vector fields of M has a spacelike subalgebra σ isomorphic to $\mathfrak{so}(n+1)$, such that (ii) the local dimension of σ as a subspace of T_pM is either 0 or n at each point $p \in M$. In general there may be many such subalgebras σ, each corresponding to a different symmetry axis. Therefore we will

call a choice of one specific σ a *choice of the origin of spherical symmetry*, and the pair (M, σ) an *n-spherically symmetric spacetime with fixed origin* (but we will abuse notation and simply refer to M, with σ implied).

Now suppose M is n-spherically symmetric with origin fixed by σ. Points where the local dimension of σ is 0 are fixed points of the spherical symmetry; we call the set of all such points the *axis* A_σ. The axis may be empty or nonempty. When nonempty, it is typically a $D-(n+1)$ dimensional submanifold of M. The complement of the axis we shall denote B_σ. By assumption, σ has local dimension n on B_σ. Thus by Frobenius's theorem [28], B_σ is foliated by n-dimensional integral submanifolds of σ corresponding to isometric flows along σ. Each point $p \in B_\sigma$ is contained in exactly one such submanifold, called its *orbit* and denoted $\mathrm{Orb}_\sigma(p)$.

We wish to show that each of these orbits has the intrinsic geometry of a sphere (its intrinsic geometry being induced by the metric on M). We do so by determining Killing vectors of the orbits. Each Killing flow generates an isometry of M, which in turn induces an isometry on the invariant subspace $\mathrm{Orb}_\sigma(p)$. Since additionally σ is tangent to the orbits, $\bar{\sigma} = \sigma\big|_{\mathrm{Orb}_\sigma(p)}$ is an algebra of Killing vector fields on the orbit, and the vector field commutators of σ are preserved by the restriction. One could imagine, however, that when restricted to the orbit, σ may no longer have the same number of independent generators (i.e. if two linearly independent fields, when restricted, became linearly dependent). This possibility is mostly (i.e. for $n \neq 3$) ruled out by the group theoretic considerations of [29]. A more concise proof follows from the algebraic approach, as follows. The restriction $\sigma \to \bar{\sigma}$, being both linear and commutator-preserving, defines a Lie algebra homomorphism. The kernel of the homomorphism must be an ideal. But since simple Lie algebras have no nontrivial proper ideals, and since our

assumption on the local dimension of σ implies that $\dim \bar{\sigma} \geq n$, simplicity of σ implies that $\dim \bar{\sigma} = \dim \sigma$. Thus, $\dim \bar{\sigma} = n(n+1)/2$ whenever $\mathfrak{so}(n+1)$ is simple, leaving only the cases $n = 1$ and $n = 3$ [30]. The same dimensionality holds for the case $n = 1$, since in that case $n(n+1)/2 = n$ already. Let us assume the case $n = 3$ causes no problems.

The above reasoning shows that σ restricts to a spacelike $n(n+1)/2$ dimensional algebra of Killing vector fields on the n-dimensional orbits, so it follows that each orbit is a maximally symmetric Riemannian manifold with symmetry algebra isomorphic to $\mathfrak{so}(n+1)$. This implies that each orbit must be locally isometric to the sphere $\mathbb{S}^n$ with metric $ds^2 = (r_{\mathrm{Orb}})^2\, d\Omega^2$. It is therefore justified to define the *areal radius (relative to σ)* at each point $p \in B_\sigma$ by $r_\sigma(p) = r_{\mathrm{Orb}_\sigma(p)}$. Correspondingly, for points $p \in A_\sigma$ on the symmetry axis we define $r_\sigma(p) = 0$. In this way the areal radius is defined for all points in M.

At every point not on the symmetry axis, there exists a local coordinate system exhibiting the foliation by spheres. Let $p \in B_\sigma \subset M$. Then p has a neighborhood with coordinates (a^λ, Ω^k), in which the metric reads

$$ds^2 = h_{\mu\nu}(a^\lambda)\, da^\mu\, da^\nu + r(a^\lambda)^2\, d\Omega^2\,, \tag{2.35}$$

where $h_{\mu\nu}(a^\lambda)$ is a $(D-n)$-dimensional Lorentzian metric depending only on a^λ, the coordinates Ω^k parameterize a σ-orbit for fixed a^λ, and $r(a^\lambda)$ is the areal radius of such an orbit. For each point q with coordinates (a^λ, Ω^k) in this patch, $r(a^\lambda) = r_\sigma(q)$. That such a coordinate system exists can be shown by construction of surface-orthogonal geodesic coordinates [31]; another proof is given by [32, (s. 13-5)].

Let it be emphasized: once an origin of spherical symmetry is fixed by choosing

σ, the areal radius $r = r_\sigma(p)$ is an intrinsic property of each point $p \in M$, independent of coordinate system. M is foliated by spheres (lying tangent to σ) with intrinsic metric $ds^2 = r_\sigma(p)^2\, d\Omega^2$, except on the axis of symmetry where $r_\sigma(p) = 0$ by definition. Everywhere except on the axis, there is a local coordinate system respecting this foliation, in terms of which the metric is (2.35).

2.12 Appendix: Proof of regularity at the horizons

Here we prove that the Penrose-coordinate metric coefficients are continuous and nonzero at all horizons and horizon vertices in Penrose diagrams obtained by the methods of section 2.5. The only exception is that the metric is sometimes discontinuous at horizon points in a small neighborhood near $|t| \to \infty$, in non-vertex corners of the diagram, as described in section 2.4.7. Before proceeding, properties of the global tortoise function of section 2.5 are proved, and some useful identities are developed.

Properties of the Global Tortoise Function

The identities (2.14) and (2.15) are proved by showing that for each zero r_i of $f(r)$ there exists a cut punctured disk D_{cut} about the origin in the complex plane, and a function $D(z)$ analytic at $z = 0$, such that for $z = x$ on the real axis in D_{cut},

$$F(r_i + x) = k_i^{-1} \ln|x| + D(x)\,. \tag{2.36}$$

It follows that the complex function $F(r_i + z) - k_i^{-1} \ln|z| = D(z)$ is analytic at $z = 0$, which, as seen below, quickly implies the desired results.

The proof of (2.36) runs as follows. Denote $F(r) = \operatorname{Re} F_c(r)$, where $F_c(r)$ is the defining integral in (2.11) with the real part sign removed. Evaluation of the semicircular contours in the small ϵ limit shows that $\operatorname{Im} F_c(r) = \pi \sum_{i=1}^{N} k_i^{-1} \Theta(r - r_i)$. By assumption, $f(r_i + z)$ is complex analytic at $z = 0$ with $f(r_i) = 0$ and $f'(r_i) = k_i$. Power series arguments show that there exists a D_{cut} (as above) on which

$$f(r_i + z) = k_i \, z \, (1 + A(z)) \,, \tag{2.37}$$

with $A(z)$ analytic at $z = 0$ and $A(0) = 0$, and on which $f(r_i + z)^{-1}$ is analytic with analytic antiderivative

$$\tilde{F}(r_i + z) = k_i^{-1} \log(z) + B(z) + C \,, \tag{2.38}$$

where $B(z)$ is also analytic at $z = 0$. $F_c(r_i + z)$, which can be written as a constant plus an integral contained in D_{cut}, analytically extends to the antiderivative $\tilde{F}(r_i + z)$ for a suitable constant. Comparing imaginary parts in $F_c(r_i + z) = \tilde{F}(r_i + z)$ for $z = x$ on the real axis shows that $B(z) + C = D(z) + i\pi(k_1^{-1} + \ldots + k_i^{-1})$ with $\operatorname{Im} D(x) = 0$. Thus $F(r_i + x) = \operatorname{Re} F_c(r_i + x) = k_i^{-1} \ln |x| + \operatorname{Re} D(x) = k_i^{-1} \ln |x| + D(x)$.

From (2.36), property (2.15) follows directly. Then, using (2.36) and (2.37), one finds

$$|f(r_i + z)| \, e^{-k_i F(r_i + z)} = |k_i| (1 + A(z)) \, e^{-k_i D(z)} \,. \tag{2.39}$$

Near $z = 0$, we define this formula by its right hand side, which is analytic and positive at $z = 0$, and obtain the property (2.14) by restricting to the real axis. This yields the limit $|f(r_i)| \, e^{-k_i F(r_i)} = |k_i| \, e^{-k_i D(0)}$ at $z = 0$.

Useful identities

Here we collect some useful identities for the functions $h(s)$ and $H_k(s)$, and the coordinate transformations $\tilde{u}(u)$ and $\tilde{v}(v)$, of section 2.5.2. The identities below include some inverse functions, which are useful for determining radii of points in the diagram, and some derivative identities, which are useful for analysis of the metric.

First of all, there are the inverse functions

$$H_k^{-1}(s) = \begin{cases} \frac{1}{k}\ln(1+ks) & k \neq 0 \\ s & k = 0 \end{cases}, \tag{2.40}$$

$$(h^{s_0}_{k_+,k_-})^{-1}(s) = \begin{cases} -s_0 + H_{k_-}^{-1}(s+s_0), & s < -s_0 \\ s, & |s| \leq s_0 \\ s_0 + H_{k_+}^{-1}(s-s_0), & s > s_0 \end{cases}, \tag{2.41}$$

which must be used to determine radii of points in the diagram.

Meanwhile, the derivatives we want are

$$H_k{}'(s) = \begin{cases} e^{ks} & k \neq 0 \\ 1 & k = 0 \end{cases}, \tag{2.42}$$

$$(h^{s_0}_{k_+,k_-})'(s) = \begin{cases} H_{k_-}{}'(s+s_0), & s < -s_0 \\ 1, & |s| \leq s_0 \\ H_{k_+}{}'(s-s_0), & s > s_0 \end{cases}. \tag{2.43}$$

From the derivatives one observes that $H_k{}'(s) = 1 + kH_k(s)$.

Now denote $h(s) = h^{s_0}_{k_+,k_-}(s)$. Due to the piecewise nature of this function, it

is useful to also define the piecewise constant

$$\kappa(s) \equiv \begin{cases} k_-, & s < -s_0 \\ 0, & |s| \le s_0 \\ k_+, & s > s_0 \end{cases} \quad . \tag{2.44}$$

In this notation (and suppressing the argument), one can write the simple expressions

$$\kappa\, h(s) = -1 + |\kappa|\, s_0 + e^{-|\kappa| s_0}\, e^{\kappa s} \ , \tag{2.45}$$

$$h'(s) = e^{-|\kappa| s_0}\, e^{\kappa s} \ , \tag{2.46}$$

$$h'(s) = 1 - |\kappa|\, s_0 + \kappa\, h(s) \ . \tag{2.47}$$

Let $\tilde{x}(x)$ be a joint notation for $\tilde{u}(u)$ and $\tilde{v}(v)$. For both u and v, the transformation from block to Penrose coordinates has the general form

$$\tan\, \pi\, (\tilde{x} - \tilde{c}) = a\, h(bx) \ , \tag{2.48}$$

for real constants a, b, c, where $h(s)$ is monotonic increasing. It follows that $\tilde{x}(x)$ is monotonic and invertible, and the derivative is

$$\frac{dx}{d\tilde{x}} = \left(\frac{\pi}{ab}\right) \left(\frac{1 + a^2\, h(bx)^2}{h'(bx)}\right) \ . \tag{2.49}$$

Applying (2.46) and (2.47) with (2.48) and (2.49), one obtains

$$\frac{dx}{d\tilde{x}} = \left(\frac{\pi}{ab}\right) \left(\frac{e^{-|\kappa| s_0}}{e^{-\kappa bx}}\right) \frac{1 + \cot^2 \pi(\tilde{x} - \tilde{c})}{\left[\kappa\, a^{-1} + (1 - |\kappa| s_0) \cot \pi(\tilde{x} - \tilde{c})\right]^2} \tag{2.50}$$

with $\kappa = \kappa(bx)$, wherever $\tilde{x} - \tilde{c} \neq 0$ (and again, x represents either u or v).

All necessary identities are now in hand.

Proof of regularity

We shall demonstrate that, in the Penrose coordinates $(\tilde{u}, \tilde{v})$, the metric coefficients are continuous and nonzero in the coordinate basis at horizons and horizon vertices, except possibly in arbitrarily small corners of the diagram where $|u/2| > s_0$, $|v/2| > s_0$, and $|t| \to \infty$. The proof proceeds by direct calculation of the metric components in a neighborhood of horizon points.

As usual (see section 2.4.2), suppose that (x, y) is a shorthand representing either (u, v) or (v, u). Begin with metric coefficients written in the form (2.23). In order to evaluate the metric at $r = r_i$, one sets the free parameter $k = k_i$. The function (2.14), which carries the explicit radial dependence, was already shown to be analytic (and thus continuous) and positive at r_i. All that is left is to evaluate the functions $G_x(x, k)$ and $G_y(y, k)$ in the appropriate limits. The details run as follows.

In light of (2.50), the metric coefficients (2.24-2.25) in each block can be rewritten

$$G_u(u,k) = \left(\frac{e^{-|\kappa_u|s_0}}{e^{(k-\kappa_u)u/2}}\right) \frac{1+\cot^2\pi(\tilde{u}-\tilde{c}_u)}{\left[\kappa_u + \epsilon_u\left(1-|\kappa_u|s_0\right)\cot\pi(\tilde{u}-\tilde{c}_u)\right]^2}\ , \tag{2.51}$$

$$G_v(v,k) = \left(\frac{e^{-|\kappa_v|s_0}}{e^{-(k-\kappa_v)v/2}}\right) \frac{1+\cot^2\pi(\tilde{v}-\tilde{c}_v)}{\left[\kappa_v + \epsilon_v\left(1-|\kappa_v|s_0\right)\cot\pi(\tilde{v}-\tilde{c}_v)\right]^2}\ , \tag{2.52}$$

where $\kappa_u = \kappa(u/2)$ and $\kappa_v = \kappa(-v/2)$, utilizing the notation (2.44).

Now suppose there are multiple blocks, all matched to their neighbors according to the prescription of section 2.5.3. Further, suppose without loss of

generality that one of the blocks has the parameters $\tilde{c}_u = \tilde{c}_v = 0$. Since all blocks must have been shifted by integer values of $\Delta\tilde{c}$, it follows from the periodicity $\cot(x+\pi) = \cot x$ that in *every* block the metric coefficients are

$$G_u(u,k) = \left(\frac{e^{-|\kappa_u|s_0}}{e^{(k-\kappa_u)u/2}}\right) \frac{1+\cot^2\pi\tilde{u}}{\left[\kappa_u + \epsilon_u\left(1-|\kappa_u|s_0\right)\cot\pi\tilde{u}\,\right]^2}\ , \tag{2.53}$$

$$G_v(v,k) = \left(\frac{e^{-|\kappa_v|s_0}}{e^{-(k-\kappa_v)v/2}}\right) \frac{1+\cot^2\pi\tilde{v}}{\left[\kappa_v + \epsilon_v\left(1-|\kappa_v|s_0\right)\cot\pi\tilde{v}\,\right]^2}\ . \tag{2.54}$$

All metric dependence on the shift parameters has been eliminated.

It remains to implement the limit $r \to r_i$. In any block bordering a horizon radius $r = r_i$, it is easy to see from their definitions that the coordinate limits have a standard pattern, depending on the sign of $k_i = f'(r_i)$. Suppose that $\mathrm{sgn}(k_i) = \pm 1$. Then in any block bordering r_i, one finds $F(r) \to \mp\infty$ and $u \to \pm\infty$ and $v \to \mp\infty$. As a result, one finds the important result that as $r \to r_i$, either $\kappa(u/2) = k_i$, or $\kappa(-v/2) = k_i$, or both. By using the free parameter $k = k_i$, the limiting value can now be evaluated.

Suppose that two blocks B_A and B_B are joined along a line of constant $\tilde{y}$, as in section 2.5.3. In both blocks, $|y| \to \infty$ near the horizon, and the limits of the preceding paragraph are such that $\kappa_y = k_i$. Then letting $k = k_i$, one finds

$$G_y(y,k_i) = \left(e^{-|k_i|s_0}\right)\ \frac{1+\cot^2\pi\tilde{y}}{\left[k_i + \epsilon_y\left(1-|k_i|s_0\right)\cot\pi\tilde{y}\,\right]^2}\ , \tag{2.55}$$

which obtains the limit

$$G_y(y,k_i) = k_i^{-2}\ \ e^{-|k_i|\,s_0} \tag{2.56}$$

when $r = r_i$, since $\cot^2\pi y = 0$ there. The limit (2.56) is independent of block

parameters, and thus automatically equal in both blocks, ensuring that $G_y(y, k_i)$ is positive and continuous across the horizon.

Meanwhile, at horizon points, the coordinate x parameterizing the horizon remains finite. On the horizon, the corresponding metric factor becomes

$$G_x(x, k_i) = \left(\frac{e^{-|k_i| s_0}}{e^{\pm (k_i - \kappa_x) x/2}} \right) \frac{1 + \cot^2 \pi \tilde{x}}{\left[\kappa_x + \epsilon_x \left(1 - |\kappa_x| s_0 \right) \cot \pi \tilde{x} \right]^2} , \tag{2.57}$$

where $\pm$ corresponds to $x = u$ and $x = v$ respectively. This expression holds on both sides of the horizon, in both blocks B_A and B_B, and is strictly positive. Since the matching conditions ensure that $\epsilon_x^A = \epsilon_x^B$, the function (2.57) is equal on both sides of the horizon for all x such that $\tilde{x}_A(x) = \tilde{x}_B(x)$ (which also implies $\kappa_x^A = \kappa_x^B$). Near horizon vertices, where all transformations $h(s)$ have the same exponential factor, and in the bulk of blocks, where $h(s) = s$, this matching is guaranteed. However, when both $|u/2| > s_0$ and $|v/2| > s_0$ near $|t| \to \infty$, then $h(s)$ may be different in the neighboring blocks for the relevant direction, yielding a discontinuity. By choosing s_0 large, the neighborhood affected by this is exception may be made arbitrarily small. Thus at all horizon points, except near $|t| \to \infty$, the function $G_x(x, k_i)$ is positive and continuous across the horizon. At a horizon vertex point, the limit (2.56) applies to both x and y, for all surrounding blocks, and the metric is, again, continuous.

To summarize, utilizing (2.55) and (2.57), the metric in a neighborhood of any horizon point or vertex point at $r = r_i$ can be written

$$ds^2 = - \left(\frac{4\pi^2}{e^{-k_i c}} \right) \frac{|f(r)|}{e^{k_i F(r)}} \; G_y(y, k_i) \, G_x(x, k_i) \, d\tilde{u} \, d\tilde{v} + r^2 \, d\Omega^2 . \tag{2.58}$$

Every factor in the coefficient of $-d\tilde{u}d\tilde{v}$ has by been shown to be positive and

continuous as a function of $(\tilde{x}, \tilde{y})$ in this neighborhood, except in arbitrarily small neighborhoods where $|t| \to \infty$. Thus, except for the polar coordinate singularity at $r = 0$, and except for the above-noted $|t| \to \infty$ exception, the global metric is continuous and strictly positive everywhere. Our goal of obtaining non-degenerate continuous global Penrose coordinates extending across an arbitrary number of horizons has been achieved.

Given the analyticity of the radial dependence in the metric (see (2.14)), one might hope to give a coordinate system which extends the full metric analytically across horizons. Indeed, this is possible by simply choosing a suitable $h(s)$. However, a trade-off has to be made. If analyticity at the horizons is retained, either differentiability of the interior metric, simplicity of $h(s)$, or simplicity of the diagram appearance must be sacrificed. An example of the latter case may be seen in figure 2.19(b). Since there is no physically motivated benefit to retaining analyticity, we give it up.

2.13 Appendix: More properties of SSS spacetimes

For convenience, we collect here some geometrical formulae for a four-dimensional SSS spacetime. Let the metric function be written

$$f(r) = 1 - \frac{2\,m(r)}{r}\ . \tag{2.59}$$

We imply no restriction whatsoever on the function $m(r)$. This is simply a very useful way to write the metric function. It is only sometimes appropriate to interpret $m(r)$ as the total mass inside radius r. Useful derived quantities include

the shell mass

$$\mu(r) = m'(r) \tag{2.60}$$

(see (2.63) and below) which determines the Einstein tensor, and the function

$$\eta(r) = \left(\frac{2\,m(r)}{r} - \frac{4\,m'(r)}{3} + \frac{r\,m''(r)}{3} \right) , \tag{2.61}$$

which controls the Weyl tensor.

Orthonormal basis

We define an orthonormal basis $\hat{e}_a$ in each block. Where $f(r) > 0$ define $\hat{e}_0 = \sqrt{f(r)^{-1}}\,\partial_t$ and $\hat{e}_1 = \sqrt{f(r)}\,\partial_r$. Where $f(r) < 0$ define $\hat{e}_0 = \sqrt{-f(r)}\,\partial_r$ and $\hat{e}_1 = \sqrt{-f(r)^{-1}}\,\partial_t$. And, everywhere, define $\hat{e}_2 = r^{-1}\,\partial_\theta$ and $\hat{e}_3 = (r\,\sin\theta)^{-1}\,\partial_\phi$. In this construction $\hat{e}_0$ is always timelike. Both $\hat{e}_0$ and $\hat{e}_1$ can be continuously extended across horizons, which is why the Einstein tensor in this basis (below) will have no discontinuities associated with the piecewise definition. However the basis cannot be continuously extended, as the extensions of $\hat{e}_0$ and $\hat{e}_1$ would coincide at the horizon. Despite this shortcoming, we often choose to work in this basis for its conceptual and calculational simplicity.

Curvature components in coordinate bases

These quantities were computed with help from the *Mathematica* package *RGTC* [33]. Sign conventions for the curvature tensors are equivalent to those found in Wald [26].

In the (t, r, θ, ϕ) coordinate basis, the nonzero Christoffel symbols are $\Gamma^t_{rt} = \Gamma^t_{tr} = -\Gamma^r_{rr} = \frac{f'}{2f}$ and $\Gamma^r_{tt} = \frac{f'f}{2}$ and $\Gamma^r_{\theta\theta} = (\sin\theta)^{-2}\,\Gamma^r_{\phi\phi} = -rf$ and $\Gamma^\theta_{r\theta} = \Gamma^\theta_{\theta r} =$

$\Gamma^{\phi}_{r\phi} = \Gamma^{\phi}_{\phi r} = \frac{1}{r}$ and $\Gamma^{\theta}_{\phi\phi} = -\sin\theta\cos\theta$ and $\Gamma^{\phi}_{\theta\phi} = \Gamma^{\phi}_{\phi\theta} = \cot\theta$.

The Riemann tensor has the symmetries $R_{abcd} = -R_{abdc} = -R_{bacd} = R_{badc}$ and $R_{abcd} = R_{cdab}$ and $R_{abcd} + R_{acdb} + R_{adbc} = 0$ [12]. Using the symmetries, all nonzero components of R_{abcd} are generated in the coordinate basis by $R_{trtr} = \frac{f''}{2}$ and $R_{t\Omega t\Omega} = \frac{rff'}{2}$ and $R_{r\Omega r\Omega} = -\frac{rf'}{2f}$ and $R_{\theta\phi\theta\phi} = r^2\,\sin^2\theta\,(1-f)$, where $R_{a\theta b\theta} = R_{a\Omega b\Omega}$ and $R_{a\phi b\phi} = (\sin^2\theta)(R_{a\Omega b\Omega})$.

The Weyl tensor has the same symmetries as the Riemann tensor above. Using the symmetries, all nonzero components of C_{abcd} are generated in the coordinate basis by $C_{trtr} = -\frac{\eta}{r^2}$ and $C_{t\Omega t\Omega} = \frac{\eta f}{2}$ and $C_{r\Omega r\Omega} = -\frac{\eta}{2f}$ and $C_{\theta\phi\theta\phi} = \eta\,r^2\sin^2\theta$, where $C_{a\theta b\theta} = C_{a\Omega b\Omega}$ and $C_{a\phi b\phi} = (\sin^2\theta)(C_{a\Omega b\Omega})$.

For calculations involving null curves and surfaces, it is often useful to also know the covariant derivative in null coordinate systems.

In double null coordinates with metric $ds^2 = -f(r)\,dudv + r^2\,d\Omega^2$, the relevant Christoffel symbols can be evaluated by the chain rule on r and $f(r)$. The nonzero components are $\Gamma^{u}_{uu} = -\Gamma^{v}_{vv} = -\frac{f'}{2}$ and $\Gamma^{u}_{\theta\theta} = -\Gamma^{v}_{\theta\theta} = (\sin\theta)^{-2}\;\Gamma^{u}_{\phi\phi} = -(\sin\theta)^{-2}\;\Gamma^{v}_{\phi\phi} = r$ and $\Gamma^{\theta}_{u\theta} = \Gamma^{\theta}_{\theta u} = \Gamma^{\phi}_{u\phi} = \Gamma^{\phi}_{\phi u} = -\frac{f}{2r}$ and $\Gamma^{\theta}_{v\theta} = \Gamma^{\theta}_{\theta v} = \Gamma^{\phi}_{v\phi} = \Gamma^{\phi}_{\phi v} = \frac{f}{2r}$ and $\Gamma^{\theta}_{\phi\phi} = -\sin\theta\cos\theta$ and $\Gamma^{\phi}_{\theta\phi} = \Gamma^{\phi}_{\phi\theta} = \cot\theta$.

Meanwhile, in the EF coordinate basis (with metric (2.3)), the nonzero Christoffel symbols are, by direct computation, $\Gamma^{r}_{rw} = \Gamma^{r}_{wr} = -\Gamma^{w}_{ww} = \frac{f'}{2\epsilon}$ and $\Gamma^{w}_{\theta\theta} = (\sin\theta)^{-2}\;\Gamma^{w}_{\phi\phi} = \frac{r}{\epsilon}$ and $\Gamma^{r}_{ww} = \frac{f'f}{2}$ and $\Gamma^{r}_{\theta\theta} = (\sin\theta)^{-2}\;\Gamma^{r}_{\phi\phi} = -rf$ and $\Gamma^{\theta}_{r\theta} = \Gamma^{\theta}_{\theta r} = \Gamma^{\phi}_{r\phi} = \Gamma^{\phi}_{\phi r} = \frac{1}{r}$ and $\Gamma^{\theta}_{\phi\phi} = -\sin\theta\cos\theta$ and $\Gamma^{\phi}_{\theta\phi} = \Gamma^{\phi}_{\phi\theta} = \cot\theta$.

Matter content, curvature scalars, and energy conditions

The Einstein tensor in the orthonormal basis $\hat{e}_a$ (defined above) is given by

$$G^a{}_b = 8\pi \begin{pmatrix} -\rho & 0 & 0 & 0 \\ 0 & p_1 & 0 & 0 \\ 0 & 0 & p_2 & 0 \\ 0 & 0 & 0 & p_3 \end{pmatrix} = 8\pi \begin{pmatrix} -\rho & 0 & 0 & 0 \\ 0 & -\rho & 0 & 0 \\ 0 & 0 & p_\Omega & 0 \\ 0 & 0 & 0 & p_\Omega \end{pmatrix} , \tag{2.62}$$

where

$$\rho = \mu/4\pi r^2 \qquad\qquad p_\Omega = -\mu'/8\pi r \ . \tag{2.63}$$

Thus, $\mu = m'(r)$ may always be interpreted as proportional to the mass of a thin shell at radius r. When μ is constant, density diffuses naturally as $1/r^2$, and there is no transverse pressure.

The curvature scalars are

$$K_0 \equiv R = 16\pi\,(\rho - p_\Omega) \tag{2.64}$$

$$K_1 \equiv R_{ab}R^{ab} = 128\pi^2\,(\rho^2 + p_\Omega^2) \tag{2.65}$$

$$K_2 \equiv C_{abcd}C^{abcd} = 12\,\eta^2/r^4 \tag{2.66}$$

$$K_3 \equiv R_{abcd}R^{abcd} = K_2 + 2\,K_1 - (1/3)\,K_0^2 \ . \tag{2.67}$$

The basis $\hat{e}_a$ diagonalizes $G^a{}_b$, with one timelike and three spacelike eigenvectors. The corresponding eigenvalues are the negative of the density $-\rho$ (timelike) and the principal pressures p_i (spacelike). It is well known that in this case, the classical energy conditions take on simple forms [10]. In particular, the null energy condition amounts to $\rho + p_i \geq 0$. For us, $\rho + p_1 = 0$ always, and the remaining

NEC constraint is equivalent to $2\mu \geq r\mu'$. The weak energy condition amounts to the NEC plus the constraint $\rho \geq 0$, which for us becomes $\mu \geq 0$. The flux energy condition of [34] amounts to $\rho^2 - p_i^2 \geq 0$ in the diagonalized case. Again, the SSS case trivially saturates $\rho^2 - p_1^2 = 0$, and the remaining constraint is equivalent to $4\mu^2 \geq r^2 \mu'^2$.

Trapped surfaces

A closed spacelike surface S is called *future trapped* (*past trapped*) if its mean curvature vector $H^a \equiv -\,\theta^+\,(k_-)^a - \,\theta^-\,(k_+)^a$ is everywhere future-directed timelike (past-directed timelike) on S [19]. In this expression, the $k_\pm$ are future-directed null vectors, each orthogonal to S, normalized by $(k_+)_a(k_-)^a = -1$. The $\theta^\pm$ are the corresponding future null expansions; they can be defined by

$$\theta^\pm \equiv -\,\gamma^{AB}(k_\pm)_\mu\, e^\nu_A\, \nabla_\nu\, e^\mu_B,$$

where e^μ_A is a basis on the tangent space T_pS of S, and γ^{AB} is the inverse of the induced spatial metric on S.

In an SSS spacetime, the sphere $(t, r, \theta, \phi) = (t_0, r_0, \theta, \phi)$, contained within a block I_j, is a closed trapped surface if and only if $f(r_0) < 0$. This is proved by direct calculation of the mean curvature vector of the sphere at SSS block points. It is simplest to work in double-null block coordinates (u, v, θ, ϕ), in terms of which the metric is (2.7). Since S is a surface of constant coordinates, its tangent space is spanned by the coordinate basis $e^\mu_\theta = \delta^\mu_\theta$ and $e^\mu_\phi = \delta^\mu_\phi$, and the induced metric γ_{AB} has line element $ds^2 = r_0^2\; d\theta^2 + r_0^2 \sin^2\theta\; d\phi^2$. A pair of mutually normalized null vectors orthogonal to S is given by $(k_+)^\mu = (|f|/2)^{-1/2}\; \delta^\mu_v$ and $(k_-)^\mu = \mathrm{sgn}(f)\,(|f|/2)^{-1/2}\; \delta^\mu_u$. With this setup, the expansions simplify to $\theta^\pm =$

$-(k_\pm)_\mu \left(\gamma^{\theta\theta} e^\nu_\theta \nabla_\nu e^\mu_\theta + \gamma^{\phi\phi} e^\nu_\phi \nabla_\nu e^\mu_\phi\right) = -(k_\pm)_\mu \left(\gamma^{\theta\theta}\, \Gamma^\mu_{\theta\theta} + \gamma^{\phi\phi}\, \Gamma^\mu_{\phi\phi}\right)$. Thus we obtain $\theta^+ = \mathrm{sgn}(f)\sqrt{2|f|/r_0^2}$ and $\theta^- = -\sqrt{2|f|/r_0^2}$. The mean curvature H^a is timelike if and only if $\mathrm{sgn}(\theta^+) = \mathrm{sgn}(\theta^-) \neq 0$, which implies that S is trapped if and only if $f(r_0) < 0$. Additionally, it is always true that $\theta^- \leq 0$. Thus when S is trapped, S is future-trapped (past-trapped) if and only if $k_\pm$ as defined above are both future-directed (past-directed). This completes the proof of the desired result.

Cartesian coordinates near the origin

In a neighborhood of $r = 0$ (contained in I_0), one can naively make the transformation from (t, r, θ, ϕ) into the cartesian coordinates $(t, \vec{x})$, according to the standard spherical coordinate transformation, such that $r^2 = \vec{x} \cdot \vec{x}$. The metric becomes

$$ds^2 = -f(r)\, dt^2 + d\vec{x}^2 + \left(\frac{2\, m(r)}{r^3\, f(r)}\right) (\vec{x} \cdot d\vec{x})^2 \tag{2.68}$$

which can be used to study the limit as $r \to 0$, as seen below.

Singularity

The metric may be either *singular* or *nonsingular* at the origin. If $m(r)$ has a Laurent series expansion about $r = 0$ then the following are equivalent:

1. M is called *nonsingular* at the origin;
2. $m(r) = \sum_{k=0}^{\infty} c_k\, r^{\,k+3}$ as $r \to 0$;
3. $f(r) = 1 + \mathcal{O}(r^2)$ as $r \to 0$;
4. Curvature scalars K_0, K_1, K_2, K_3 all finite at origin;
5. Cartesian metric has a finite limit as $r \to 0$;

6. M contains the $r = 0$ axis as a set of points, and is geodesically complete there

   (i.e. all geodesics terminating there can be extended);

Proof. By definition $(i) \leftrightarrow (ii)$, and trivially $(ii) \leftrightarrow (iii)$. Direct calculation shows $(ii) \leftrightarrow (iv)$ and $(ii) \leftrightarrow (v)$. Then $(v) \rightarrow (vi)$ and $(vi) \rightarrow (iv)$ by existence of normal neighborhoods [35], assuming sufficient differentiability.

Evidently if an SSS spacetime is nonsingular at the origin, then $f(0) = 1$, the axis $r = 0$ is a timelike curve, and to quadratic order the dominant behavior as $r \rightarrow 0$ is either flat, de Sitter, or Anti de Sitter.

Chapter 3

Understanding black hole evaporation using explicitly computed Penrose diagrams

This chapter is based on the article "Understanding black hole evaporation using explicitly computed Penrose diagrams" by Joseph Schindler, Anthony Aguirre, and Amita Kuttner [2].

Abstract

Rigorously computed Penrose diagrams are plotted for a semiclassical model of black hole formation and evaporation, in which black holes form by the accretion of infalling spherical shells of matter and subsequently evaporate by emitting spherical shells of Hawking radiation. The method allows arbitrary interior solutions of the form $ds^2 = -f(r)\,dt^2 + f(r)^{-1}\,dr^2 + r^2\,d\Omega^2$, including singular and nonsingular models. Matter dynamics are visualized by explicitly plotting proper

densities and pressures in the diagrams, as well as by tracking the location of trapped surfaces and energy condition violations. The most illustrative model accurately approximates the standard time evolution for black hole thermal evaporation; its time dependence and causal structure are analyzed by inspection of the rigorous diagram. The resulting insights contradict some common intuitions and assumptions, and we point out some examples in the literature with assumptions that do not hold up in our more detailed model. Based on the new diagrams, we argue for an improved understanding of the Hawking radiation process, propose an improved definition of "black hole" in the presence of evaporation, and suggest some implications regarding information preservation and unitarity.

3.1 Introduction

The discovery that black holes (BHs) theoretically evaporate [5, 36, 37, 38] in apparently thermal radiation has raised a number of fundamental questions over the years, chief among them the issue of how to reconcile such evaporation with unitary evolution that preserves information, and how to reconcile descriptions of a BH by an infalling observer with those of an exterior observer.

We contend that a full understanding of these issues can greatly benefit from a more detailed understanding of the spacetime structure of an evaporating black hole. Accordingly, in this work we provide a well-defined class of spacetimes representing a semiclassical model of BH formation and evaporation, and construct explicitly computed Penrose diagrams for these models using the formalism recently developed in [1].

Our model corresponds to spherical BHs which form by accreting infalling spherical null shells of matter, and evaporate by emitting spherical null shells of

Hawking radiation from near the horizon (notably, the emission location is fixed by energy conservation considerations). Interior metrics including both singular and nonsingular centers are within the scope of our methods. In the most detailed version of the model, continuous time evolution for both the accretion and evaporation processes is approximated by the use of many shells.

The basic structure of the model is motivated by its similarity to renormalized stress tensors usually associated with the evaporation process [39]. It is quite similar in spirit to the models first presented by Hiscock [40, 41] and Hayward [42], and our more sophisticated diagrams may be roughly thought of as numerically calculated versions of the diagram that Hayward originally sketched (although his and our models do differ slightly). By plotting Penrose diagrams for this model in a way that accurately represents both the global and local causal structure of the exact four-dimensional geometry, we are able to attain a more detailed view of the structure of an evaporating BH metric than was previously possible.

Many aspects of the "true" spacetime for an evaporating BH remain unknown. There are many proposals for the BH end state [43, 44, 45], and questions have been raised about in what regimes evaporation dominates the dynamics [46], and about the general applicability of classical spacetimes in describing quantum effects. Nonetheless, BH evaporation appears to be a phenomenon which probably can occur, and for now seems likely to dominate if the environment is sufficiently cold. If so, one expects evaporation from astrophysical masses down to near the Planck scale, at which point semiclassical arguments fail and many alternatives seem plausible.

But while the physical relevance of BH evaporation may be up for debate, its importance in the literature certainly is not — its study has spawned some famous questions [37, 47, 48], and reasoning about these questions almost invariably draws

on assumptions about classical spacetime diagrams.

Our intention here is to investigate a simple, concrete model, which hopefully captures most generic aspects of an evaporating BH spacetime, and for which explicit Penrose diagrams can be attained. At least away from the singularity (or away from the nonsingular Planck-density core), our spacetimes should provide a reasonably advanced model of epochs where the dynamics is dominated by accretion or thermal evaporation.

We use the new diagrams to address, within the context of our model, some persistent questions about BH spacetimes:

- Can a BH form in a finite time as viewed by a distant observer? *(Answer: Yes.)*

- Of the many types of horizon associated with BH spacetimes (event, apparent, trapping, Killing, etc.), which has physical meaning in terms of the BH boundary? (*Answer: The invariant apparent horizon defined by [49], which is the boundary of a distinguished subset of the trapped region of spacetime, and which here basically coincides with $r = 2m$ with a time-dependent mass.*[1]*)*

- What is the causal structure of the apparent horizon? *(Answer: The (outer) apparent horizon is timelike during evaporation, and spacelike during accretion.)*

- Within the context of a purely classical model, does it make sense to think of Hawking radiation as being emitted from a certain location? And if so,

[1]We call this just the "apparent", or in certain contexts "trapping", horizon, although its definition is slightly different than the traditional apparent or trapping horizons (see later sections and appendix). Its intersection with spatial hypersurfaces is an apparent horizon in the traditional sense, and it acts as the boundary of the physically important part of the trapped region, so the terminology is sufficiently unambiguous.

where? *(Answer: Yes, from just outside the apparent horizon, which during evaporation is a timelike surface.)*

- In evaporating nonsingular ("regular") BH models, in terms of causal structure: Where exactly are the regions of high density and pressure, where are energy conditions violated, and where are the inner and outer horizons relative to the core? *(Answer: See diagrams.)*

- Is it possible to escape the trapped region if the BH is evaporating? *(Answer: Yes, but it requires very good timing. Falling too far past the apparent horizon ensures your destruction in the singularity or (in nonsingular models) core.)*

At least within our model, these questions (as well as others we consider) have clear, unambiguous answers.

We also apply these diagrams to the analysis of some broader questions: What is the proper definition of a BH? What is the correct interpretation of the Hawking radiation mechanism? Can self-consistent models of BH evaporation be achieved within semiclassical gravity? Is information preserved during BH evolution? The discussion of these and other questions is taken up in the later sections of the paper.

The traditional spacetime diagram for an evaporating BH is depicted in Fig. 3.1. It is essentially the outline of a Schwarzschild BH (formed by collapse) attached to Minkowski space in an unspecified way. There are a few reasons to be wary of this diagram, and to think it may benefit from a more formal treatment.

First, the traditional diagram is ambiguous about what spacetime it is meant to represent — it does not correspond to any particular model of BH evolution. The mechanism of evaporation is left unspecified, and the nature of point B (where

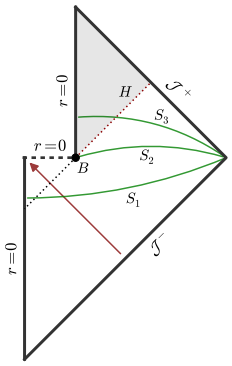

Figure 3.1: (Color online). Conventional Penrose diagram of an evaporating black hole. The hole forms via the infall of null dust (red arrow) and forms an event horizon (black dotted). At some point the black hole evaporates, leaving Minkowski space. Such a diagram usually does not represent any spacetime — the mechanism of evaporation is left ambiguous, and the nature of point B is totally unclear. In the obvious classical-spacetime interpretations of this diagram, however, point B must be considered a naked singularity that creates a Cauchy horizon H (red dotted), raising questions about the applicability of this diagram for analyzing potentially unitary BH evaporation. Below, we attempt to eliminate these ambiguities by constructing Penrose diagrams for well-defined spacetime models of BH evolution.

all physics of the evaporation process is hidden) is totally unclear. Since a sketch like this inherently captures no more information than the assumptions put into creating it, it is difficult to learn anything from such a diagram.

Second, any reasonable translation of the traditional diagram to a classical spacetime has a naked singularity and corresponding Cauchy horizon; this can be shown both in simple examples and on general grounds.[2] This appears to have been noticed at least by Hawking [36] and Birrell and Davies [51] from the beginning, but is forgotten in most modern discussions. In particular, many discussions of the information preservation problem (see for instance [47] for a highly referenced example) make essential use of supposed Cauchy surfaces within this diagram, including surfaces on both sides of the evaporation event. But if the spacetime underlying the diagram has a naked singularity and is not globally hyperbolic, no such Cauchy surfaces can be assumed to exist. Because of this hidden assumption of unpredictability, the usefulness of such a diagram in analyzing possibly unitary BH evaporation must be called into question.

Recognizing these shortcomings, and that evaporation may profoundly change the character of the BH spacetime diagram, a number of studies have suggested improved diagrams that more easily allow an interpretation in which information is preserved [42, 52, 53, 54, 55, 56, 57, 58, 44, 43, 59]. These form a useful background for investigating BH evaporation and related issues, and we build most directly on the work of Hayward [42], who has provided the most minimal and generic model.

[2] In the simplest rigorous interpretation of the standard diagram, where the BH is annihilated by an incoming spherical null shell (for example as in Fig. 3.2a), a point must be excised from the final Minkowski space for gluing to be topologically allowed near B, which creates a Cauchy horizon. The general argument relies on theorems of Geroch [50] — since the domain of dependence of a surface is globally hyperbolic, the assumption that the region beyond H is determined by S_1 contradicts continuity of the past and future volumes within a globally hyperbolic space.

By extending this type of model to a form in which explicit Penrose diagrams can be attained, we explore the structure of these improved models while resolving the ambiguity and hidden assumptions inherent to hand drawn diagrams. The new diagrams (Figs. 3.4–3.7) are simultaneously both Penrose diagrams and exact coordinate diagrams, allowing a detailed picture of the exact geometry. A discussion of the diagram formalism, and an explanation of some key aspects of interpreting the new diagrams, is provided in Section IV.

3.2 Shell model of black hole formation and evaporation

We model the process of black hole formation and evaporation according to the following assumptions:

(i) The black hole is non-rotating and spherically symmetric.

(ii) The process is quasistatic, allowing dynamical evolution to be modeled by a sequence of equilibrium BH solutions joined across null shells of matter (such null shells may represent either truly light-like radiation, or highly accelerated timelike matter).

(iii) The equilibrium black hole solutions locally have the form $ds^2 = -f(r)\,dt^2 + f(r)^{-1}\,dr^2 + r^2\,d\Omega^2$.

(iv) Stellar collapse and mass accretion is modeled by a sequence of ingoing spherical null matter shells, incident from infinity.

(v) Hawking radiation is modeled by pairs of spherical null matter shells. Each pair consists of an outgoing positive-mass shell and ingoing negative-mass

shell. Each pair nucleates at a fixed radial distance $l_{\rm ev}$ outside the apparent horizon, with both shells propagating toward the future. Nucleation points violate the DTR relation (an equation related to energy conservation, see appendix), but the amount of violation is arbitrarily small in the $l_{\rm ev} \to 0$ limit. If $l_{\rm ev} \approx l_{\rm pl}$, tiny DTR violations may be considered small quantum fluctuations. In this sense, in our semiclassical model, energy conservation forces Hawking radiation to be emitted from just outside the horizon.

This model is a slightly generalized discrete approximation to that proposed originally by Hayward [42], and the evaporation mechanism agrees, heuristically, with the classic calculation by Davies, Fulling, and Unruh of the stress tensor for a quantum scalar field in the presence of a static BH [39]. We construct spacetimes applying this model, and their corresponding Penrose diagrams, by the methods of [1]. It is assumed that physically realistic models are achieved by first taking the limit $l_{\rm ev} \to l_{\rm pl}$ at each shell of Hawking radiation, then taking the continuous (many-shell) limit.

The simplest example of this approach, in which formation and evaporation each occur in a single burst, is depicted schematically in Fig. 3.2 for both singular and nonsingular interior cases; the exact diagrams will be given later. More realistic models are obtained by using an arbitrarily large number of shells and piecewise regions to approximate the desired smooth dynamics.

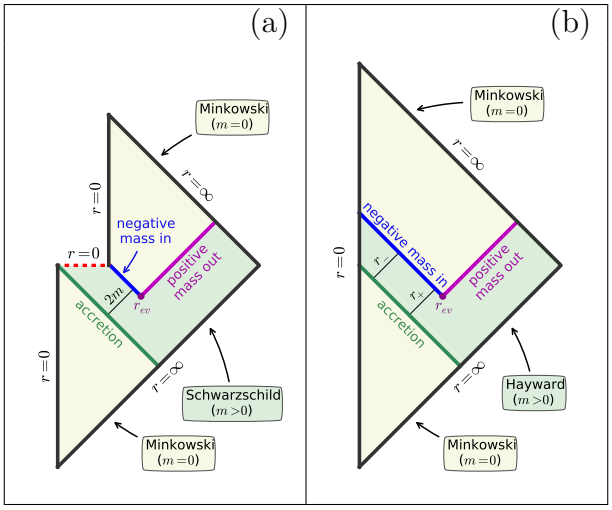

Figure 3.2: (Color online). Schematic illustration of Penrose diagrams for the shell model in simple cases. (a) The simplest singular case: a Schwarzschild black hole forms by collapse of a spherical null shell, and evaporates by emitting a single burst of Hawking radiation, which nucleates at a radius $r_{\rm ev} = r_{\rm hor} + l_{\rm ev}$ just outside the apparent horizon at $r_{\rm hor} = 2m$. (b) The simplest nonsingular case: a Hayward black hole (see below) forms and evaporates in the same way.

3.3 Matter Content of Shell Models with Schwarzschild or Hayward Interior

A benefit of explicit diagrams is that matter dynamics during the formation and evaporation processes can be quantitatively tracked. We are concerned with four quantities:

(i) The proper density and pressures of the bulk (equilibrium) spacetime, defined (up to a sign) as eigenvalues of $G^{\mu}{}_{\nu}/(8\pi)$. For metrics of form (3.1) these include a density ρ, a transverse pressure $p_t = -\rho$, and an angular pressure p_Ω. Also useful is the mass function $m(r)$ defined by $f(r) = 1-2m(r)/r$.

(ii) The location of trapped surfaces in the bulk spacetime, as characterized by the trapped spheres region (see appendix). Trapped spheres occur where

$f(r) < 0$ in the metric (3.1), and the trapped spheres region is bounded by trapping/apparent horizons where $f(r) = 0$ (see appendix).

(iii) The location and magnitude of energy condition (EC) violations in both the bulk spacetime and on the null shells, quantified by the EC violation functions χ_{NEC}, χ_{WEC}, and χ_{FEC} (see appendix).

(iv) The local surface density σ of null shells, which is proportional to the mass jump $[m(r)]$ across the shell (see appendix). The proportionality is positive (negative) for a shell which is radially ingoing (outgoing) towards the future.

A detailed general analysis of the matter content for models of the present type is given in the appendix.

Our setup allows for a variety of models of the black hole interior; any metric of the "strongly spherically symmetric" form

$$ds^2 = -f(r)\,dt^2 + f(r)^{-1}\,dr^2 + r^2\,d\Omega^2 \tag{3.1}$$

is allowed. Metrics of this type can be either singular or nonsingular at $r = 0$ (for definition and properties see appendix). Nonsingular models have the advantage that all matter is made explicit in the stress tensor, whereas singular solutions contain a matter contribution hidden in the singularity. Although classical theorems do predict singularity formation in gravitational collapse [60], nonsingular solutions are thought to arise in effective semiclassical approximations if quantum gravitational effects regulate curvature at the Planck scale. Nonsingular solutions often violate classical energy conditions, but since quantum field theories are well known to do the same, this is not a major defect [61].

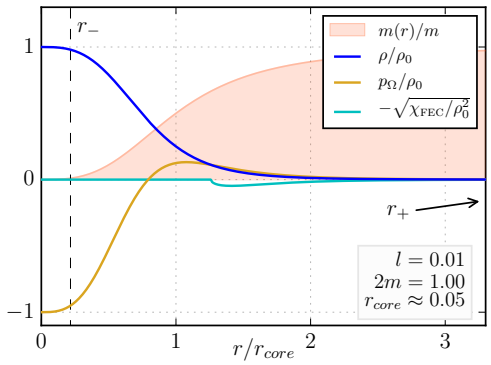

Figure 3.3: (Color online). Matter content of the Hayward spacetime. Density and pressure are maximized at $r = 0$, with maximum density $\rho_0 = \frac{3}{8\pi l^2} = m/\left(\frac{4}{3}\pi r_{core}^3\right)$. The FEC violation function $\chi_{\rm FEC}$ (see appendix) shows non-negligible violations occur near the core surface; NEC and WEC are violated at negative-mass shells in the dynamic model, but not here in the bulk. The plot shows a small BH, but is mostly parameter-independent: increasing m pushes the horizons at $r_- \approx l$ (dashed) left and at $r_+ \approx 2m$ (off scale) right, with no other effects. Spheres are trapped surfaces for all $r_- < r < r_+$, which we call the trapped spheres region.

A number of common metrics are of the form (3.1), including

Minkowski	$f(r) = 1,$
de Sitter	$f(r) = 1 - r^2/L^2,$
Anti de Sitter	$f(r) = 1 + r^2/L^2,$
Schwarzschild	$f(r) = 1 - 2m/r,$
Reissner-Nordstrom	$f(r) = 1 - 2m/r + Q^2/r^2,$
Hayward	$f(r) = 1 - 2mr^2/(r^3 + 2ml^2),$

among others. We limit for now our consideration to two simple cases: Schwarzschild (singular) and Hayward (nonsingular) interiors.

We take the Schwarzschild metric to model BHs containing a singularity. As is well known, the matter content is trivial: the spacetime contains a vacuum everywhere outside the singularity at $r = 0$. Trapped spheres occur in the interval

$0 < r < 2m$, with a horizon located at $r = 2m$. For two Schwarzschild solutions of mass parameter $m_\pm = m \pm \Delta m/2$ joined at a null shell, the mass jump $[m(r)] = \Delta m$ is a constant, and ingoing (outgoing) positive-mass shells increase (decrease) mass toward the future. There are no EC violations.

Black holes with nonsingular interior we model by the Hayward metric, with

$$f(r) = 1 - \frac{2mr^2}{r^3 + 2ml^2}. \tag{3.2}$$

Density, pressures, and energy condition violations associated with this metric are shown in Fig. 3.3.

This metric has parameters l and m; l determines the proper density measured at the core and defines the length scale on which curvature is regulated by quantum gravitational effects, while m determines the black hole mass measured by a distant observer. In our models, l is held fixed at a small value, while only m varies across shells. Physically, one assumes that $l \approx l_{\rm pl}$, and that $2m \gg l$ except in the final moments of evaporation.

When $2m \gg l$, a radial slice of Hayward spacetime is split into three intervals by horizons at

$$r_- \approx l \qquad \text{(inner horizon)},$$
$$r_+ \approx 2m \qquad \text{(outer horizon)},$$

with trapped spheres occuring in the interval

$$r_- < r < r_+ \qquad \text{(trapped spheres region)}.$$

The matter distribution describes an extremely dense (Planck scale density)

core of length scale

$$r_{\rm core} = (2ml^2)^{1/3}, \tag{3.3}$$

which (except in the final moments of evaporation) obeys $l \ll r_{\rm core} \ll 2m$. It is thus useful to think of the following regions:

$$\begin{aligned} r &\ll r_{\rm core}, \quad && \text{Quantum Gravity Core,} \\ r &\approx r_{\rm core}, \quad && \text{Core Surface,} \\ r &\gg r_{\rm core}, \quad && \text{Nearly Schwarzschild Vacuum.} \end{aligned}$$

The core contains a homogeneous distribution of extreme density and pressure (Ricci curvature $\sim l^{-2}$), with metric closely approximating de Sitter. Far away from the core, the metric closely approximates the traditional Schwarzschild vacuum (Ricci curvature vanishes like $(r/r_{core})^{-6}$). The core surface is characterized by a rapid change in density and pressure accompanied by EC violations. It is satisfying that the core extends outside the inner trapping horizon: despite the lack of a singularity, trapped matter is doomed to quantum gravity decomposition.

When Hayward regions of mass parameter $m_\pm = m \pm \Delta m/2$ are joined across a null shell junction, the resulting mass jump is

$$[m(r)] = \Delta m \, \frac{\left(\frac{r^3}{2|\Delta m| l^2}\right)^2}{\left(\frac{r^3}{2|\Delta m| l^2} + \frac{m}{|\Delta m|}\right)^2 - 1} \, , \tag{3.4}$$

which develops monotonically from zero at $r = 0$ to Δm at $r \to \infty$ for small $\Delta m/m$. Far from $r = 0$, this closely approximates the Schwarzschild case, with a constant mass jump Δm. Near $r = 0$, the shell mass gradually approaches zero over lengths of order $(2|\Delta m| l^2)^{1/3}$, as the shell is absorbed into (or generated by) the quantum gravity region.

It is often convenient to describe spacetimes of the form (3.1) in double-null Eddington-Finklestein coordinates (u, v) defined by

$$\begin{aligned} du &= dt - f(r)^{-1}\, dr, \\ dv &= dt + f(r)^{-1}\, dr. \end{aligned} \tag{3.5}$$

An integration constant in each coordinate acts as an unphysical overall time translation. For asymptotically flat cases, the coordinate v runs along past null infinity (at constant $u = -\infty$), while u runs along future null infinity (at constant $v = \infty$).

How generic is the Hayward metric for describing nonsingular BHs? If we restrict to the form (3.1), very generic: assuming the topology of a stellar-collapse BH, so that $r \to 0$ is included in the spacetime, the asymptotic behaviors as $r \to 0$ and $r \to \infty$ are fixed by physical considerations (nonsingularity, monotonic density, approximately Schwarzschild), so the only freedom in $f(r)$ involves the transition to vacuum at the core surface. Since details of the mass profile at the core surface have no important effect on causal structure (no additional horizons are introduced without a drastic change), the exact form of $f(r)$ is not important. On the other hand, there does exists a freedom to generalize (3.1) by including a redshift factor $\alpha(r)$ such that

$$ds^2 = -\alpha(r)^2 f(r)\, dt^2 + f(r)^{-1}\, dr^2 + r^2\, d\Omega^2, \tag{3.6}$$

while maintaining the same qualitative picture. Including this redshift factor leaves the proper density unchanged, but alters the curvature scalars and proper pressures, in addition to modifying proper times measured by fixed-radius observers. The possibility of including a redshift factor seems physically admissible

(so long as care is taken to make sure it introduces no undesirable effects), and is worth further consideration; one interesting application of this approach was given recently in [62]. While we do not include the metric (3.6) in our full analysis (it is outside the scope of our algorithm for generating Penrose diagrams), we do not expect the omission to have a major effect on the resulting diagrams, since the redshift factor does not significantly alter the causal structure.

In what follows, the matter content that has been described throughout this section will be plotted in spacetime diagrams to visualize the flow of matter during BH formation and evaporation.

3.4 Diagram formalism

The new diagrams presented here (Figs. 3.4–3.7), which are constructed using the methods developed in [1], may look somewhat strange to those used to only outlines and sketches. A few comments are in order.

The diagrams are obtained by directly finding a global, compact, double-null coordinate system for the spacetime — in this sense they are not just Penrose diagrams, but also exact spacetime coordinate diagrams.[3] This allows all aspects of the exact four-dimensional geometry to be captured in the diagram, including both the global and local (interior) causal structure. No conformal information is

[3]The usefulness of the direct coordinate approach to causal diagrams was always made clear by Carter [63, 64] and others (e.g. [65]), but is not always made explicit in modern treatments, which sometimes put more emphasis on conformal mappings following Penrose's original method [66, 67]. But the conformal transformation aspect of Penrose diagrams is actually slightly misleading in four dimensions, since it is common to construct diagrams for spacetimes which are neither conformally flat nor conformally related to anything interesting (see [68]). It is only the two-dimensional diagram plane (normal to the symmetry directions) which is necessarily conformally flat. The coordinate diagram approach is more in the spirit of Carter than Penrose, and it would be justified to alternately call these Penrose-Carter diagrams, but that name is longer and less traditional. For more details about the theory of these diagrams, see [1].

thrown away. Each point in the diagram represents a spherical symmetry surface, and, because of the symmetry, it makes sense to discuss the exact Riemann curvature (as well as anything derived from it, like proper densities and pressures) and exact geometry at any point of the diagram. We make use of this to precisely plot the matter content, trapped surfaces, and other features within the diagram. That these coordinate diagrams simultaneously act as Penrose diagrams, correctly portraying the causal structure in the usual way, is ensured within our formalism [1].

Given any spacetime, there exists the freedom to deform it by arbitrary conformal transformations without disrupting the causal structure. Consequently, there is sometimes assumed to be a corresponding freedom to conformally distort Penrose diagrams. But while it is true that conformal deformations preserve causal structure of the diagram, such deformations do not preserve the geometry of the spacetime which is supposed to be represented. Since we are interested in exactly representing the full spacetime geometry (and not merely conformally related spacetimes), arbitrary conformal distortions to the diagram cannot be allowed.

Despite this restriction, there remains a large amount of freedom to distort the diagram by change of coordinates. In particular, any change of coordinates which acts conformally on the metric[4] yields another valid diagram. In practice, this freedom amounts to separately deforming the U and V coordinates (which are some null coordinates defining the diagram) by any monotonic functions.

While the freedom to deform Penrose diagrams is well known, it is not widely recognized just how different a set of valid deformations can make a diagram ap-

[4]That is, when restricted to the two-dimensional diagram plane (see footnote 3) it alters the metric only by an explicit conformal factor. This preserves the causal structure of the coordinate system [1].

pear. We will see in Fig. 3.5 that three causally equivalent diagrams paint what, at first glance, appear to be three very different pictures of the same spacetime. The key point in reconciling the apparent difference is that in any single diagram, some features are squished beyond recognition. This is unavoidable, since evaporating BH spacetimes contain a number of length/time scales (Planck scale, horizon scale, formation timescale, evaporation timescale, and in nonsingular models: core scale) which can be drastically different.

For instance, in any model where the BH has a macroscopic mass, the Planck scale, horizon scale, and evaporation timescale (and in nonsingular models, the core size) are all extremely different. Any individual diagram will only clearly represent one of these scales at a time (the rest being squished into points lines and edges). Gaining a clear understanding of the complete causal structure therefore requires the use of multiple diagrams. By carefully inspecting and comparing a few, the full story can be pieced together.

While allowing more general (non-coordinate) conformal transformations in the diagram plane would, in a strictly pointwise-causal-structure sense, allow more scales to be depicted simultaneously by ignoring distance information, it would also (as discussed above) destroy the exact representation of the four-dimensional geometry which is essential to our analysis. This implies a lesson about sketching diagrams: If one wishes to accurately depict details of the internal structure, the class of allowed diagram deformations may be more restricted than naively assumed.

For more details on how these diagrams are constructed, a more general formalism for the analysis of Penrose diagrams (including, for example, a strict definition of what a Penrose diagram is), and further discussion of the relation between Pen-

rose diagrams and conformal transformations, consult [1][5].

3.5 Diagrams for simple models

Explicitly computed diagrams are shown in Fig. 3.4 for the simple models depicted schematically in Fig. 3.2. The parameters were chosen to emphasize certain qualitative aspects, but are not particularly realistic (see Fig. 3.5 for an improved model). The simple models capture most qualitative features of the more detailed diagrams, and several features in particular are worth noting.

Immediately apparent is the similar location of the Schwarzschild singularity and the Hayward core surface (this coincidence is generic, see [1]); the two surfaces almost exactly coincide. The intersection of the singularity with timelike $r = 0$ corresponds to the point B in Fig. 3.1, about which questions were raised in the introduction. From a technical perspective, this point creates a Cauchy horizon in Fig. 3.4a since topological matching conditions require that B be excised from the final Minkowski space. It is probably more physical, however, to examine the nature of point B by looking at the corresponding point in Fig. 3.4b. Clearly, a surface like S_2 of Fig. 3.1, terminating at the point corresponding to B, is not a Cauchy surface in the regularized spacetime. At least to the extent that the singularity cuts off an unknown semiclassical spacetime, this shows on physical grounds that B should be considered a naked singularity. This picture is likely generic to nonsingular extensions of the Schwarzschild solution, as the causal structure of the core does not depend on details of the metric. While the spacetime of Fig. 3.4b is globally hyperbolic, the above analysis has an important

[5]The methods of [1] have been implemented in a software module `xhorizon` for Python, which is under development by the authors and available under a free open source license at https://github.com/jcschindler01/xhorizon.

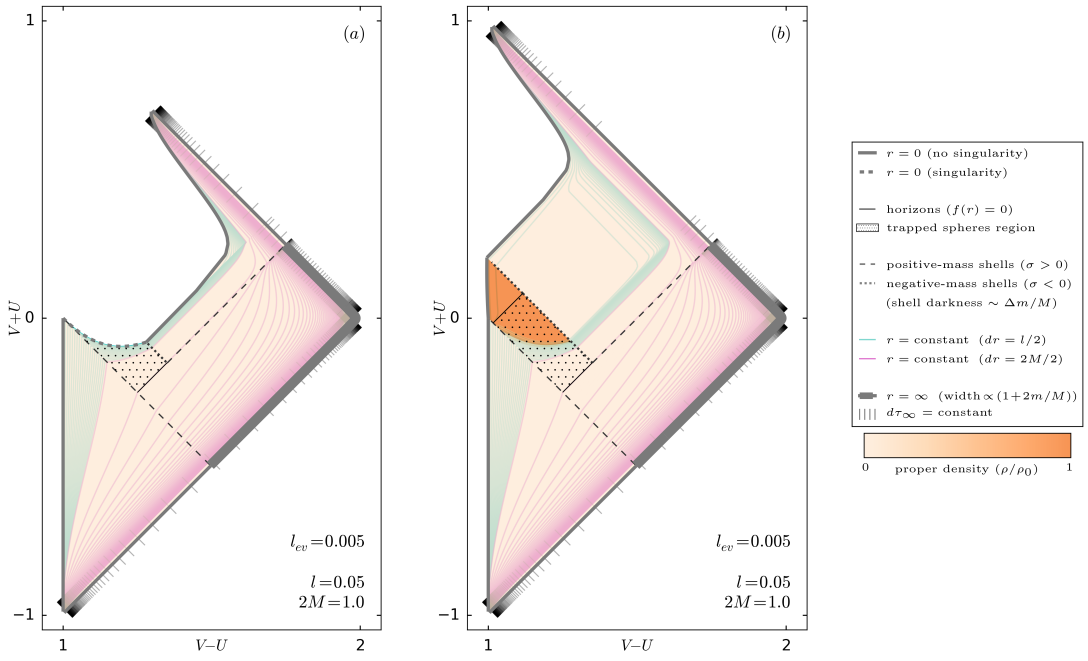

Figure 3.4: (Color online). Penrose diagrams for (a) singular and (b) nonsingular black holes which form by accreting a single shell of infalling matter and evaporate by emitting a single blast of Hawking radiation (see Fig. 3.2 for an illustrative schematic). Parameters are chosen to illustrate qualitative features, but the time evolution and relative length scales are not realistic (see Fig. 3.5 for improved model). Positive-mass (accretion and outgoing Hawking radiation, gray dashed) and negative-mass (ingoing Hawking radiation, gray dotted) shells separate the spacetime into piecewise regions, with Hawking radiation nucleating at a tiny radial distance l_{ev} outside the horizon of the region to its past. In diagrams with many shells, shell masses are indicated by grayscale darkness (darkness proportional to $1+2\,\Delta m/M$). The curvature cutoff length scale l (which has physical significance only in Hayward regions) is held fixed across all regions, while the mass parameter m (which in every region determines the gravitational mass measured by a distant observer) varies. [Caption continued on next page...]

Figure 3.4: [...Caption continued from previous page.] The total mass M is the maximum value of m in any region, and locally m is visualized by the linewidth of the conformal boundary at $r = \infty$ in each region (linewidth proportional to $1 + 2m/M$). Tick marks (gray) along $r = \infty$ mark off equal increments of proper time for an infinitely distant observer at constant radius (i.e. constant increments of du and dv along null infinity). The trapped spheres region (black dot-hatch fill), bounded by horizons (black) where $f(r) = 0$, contains closed trapped spheres. Background coloring is determined by the local proper density ρ (orange color scale) scaled by the maximum density $\rho_0 = 3/(8\pi l^2)$. The Hayward core is clearly visible as a dark orange region in the density plot, and the core surface almost exactly corresponds to the singularity location in the Schwarzschild case. Notably, distant observers near future null infinity begin to observe Hawking radiation at the same moment they see the infalling accretion shell fall through its own horizon. Lines of constant radius are shown at small ($dr = l/2$, teal) and large ($dr = 2M/2$, magenta) length scales; even where they appear bundled or strongly kinked, they do in fact remain continuous. One strange-looking feature of this diagram is the appearance of a set of wiggly kinks and a few stray tick marks to the future (measured along future infinity) of the final evaporation shell, before the very stretched out area; this is an artifact of the unrealistic parameters, and in more realistic models these kinks and tick marks all coincide with the final shell. Coordinates V and U defining the axes are basically arbitrary null global coordinates, defined further in [1]. The same visualization scheme described here is used in all examples below.

consequence: the spacetime of Fig. 3.4a is not.

A natural question to ask about an evaporating BH is whether it's possible to escape after falling through the apparent horizon. Formally, *do there exist timelike curves intersecting the trapped region but avoiding the core or singularity?* According to our shell model, the answer is yes, as is evident from Fig. 3.4. Indeed, as seen even more clearly in Fig. 3.5, during evaporation the apparent horizon forms a timelike surface of decreasing radius, despite being locally null within each piecewise region. For an observer who barely crosses the horizon, it's possible to wait for the horizon to "evaporate past," allowing an escape. Nonetheless, all timelike observers in the trapped region are radially infalling, and will eventually be doomed to destruction in the core if the black hole is long-lived relative to their ability to accelerate.

Tick marks along null infinity in Fig. 3.4 represent constant intervals $du = const$ and $dv = const$ along future and past null infinity respectively. Aside from specifying equal increments of proper time for distant observers, these ticks are useful for analyzing particle creation by the spacetime in quantum field theoretic computations. In the standard analysis, in and out vacuum modes are associated with the u and v coordinates, and the thermal Hawking flux is associated with an infinite phase buildup found by comparing dv increments to traced-back du increments at past null infinity [36]. Noting that the tick marks have an additive opacity (so that darker marks actually show many superimposed ticks), it's clear that some approximation to the usual phase buildup effect is present in both Fig. 3.4 and the subsequent examples.

While the simple single-burst models capture many aspects of the more realistic diagrams, they also differ in certain respects. Most importantly, realistic models have four very different length scales, corresponding to $l_{\rm pl}$, $r_{\rm core}$, M, and

the BH lifetime $\tau_{\rm ev}$ (where l and $l_{\rm ev}$ are both on the $l_{\rm pl}$ scale). As a consequence, more realistic diagrams tend to have very sharply kinked features, and features can be clearly portrayed only for one length scale at a time, with other features relegated to lines, bundles, and corners. Another difference between Fig. 3.4 and more advanced models is quite noticeable: as also described in the caption, the separation (measured along future infinity) between kinks in the lines $r = const$ and the final evaporation shell is an artifact of the unrealistic parameters of Fig. 3.4. In Fig. 3.5 and other realistic models, all diagram features associated with the final step of evaporation coincide with the final shell.

3.6 Diagrams for a nonsingular model with more realistic time evolution

A more detailed model is attained by approximating continuous time evolution with a large number of shells and piecewise regions. A diagram of this type, constructed based on a Hayward interior of fixed curvature cutoff length scale l, is presented in Fig. 3.5. Its parameters, justification, and implications are discussed below. While we have chosen here to work with a nonsingular model, all the diagrams can be translated to the Schwarzschild case by simply replacing the core surface with a singularity and ignoring the interior region (see [1] for why this is valid).

The desired time evolution is specified by a pair of mass functions $m_u(u)$ and $m_v(v)$ describing the mass as a function time measured by distant observers at future and past null infinity, respectively. The mass functions are mutually

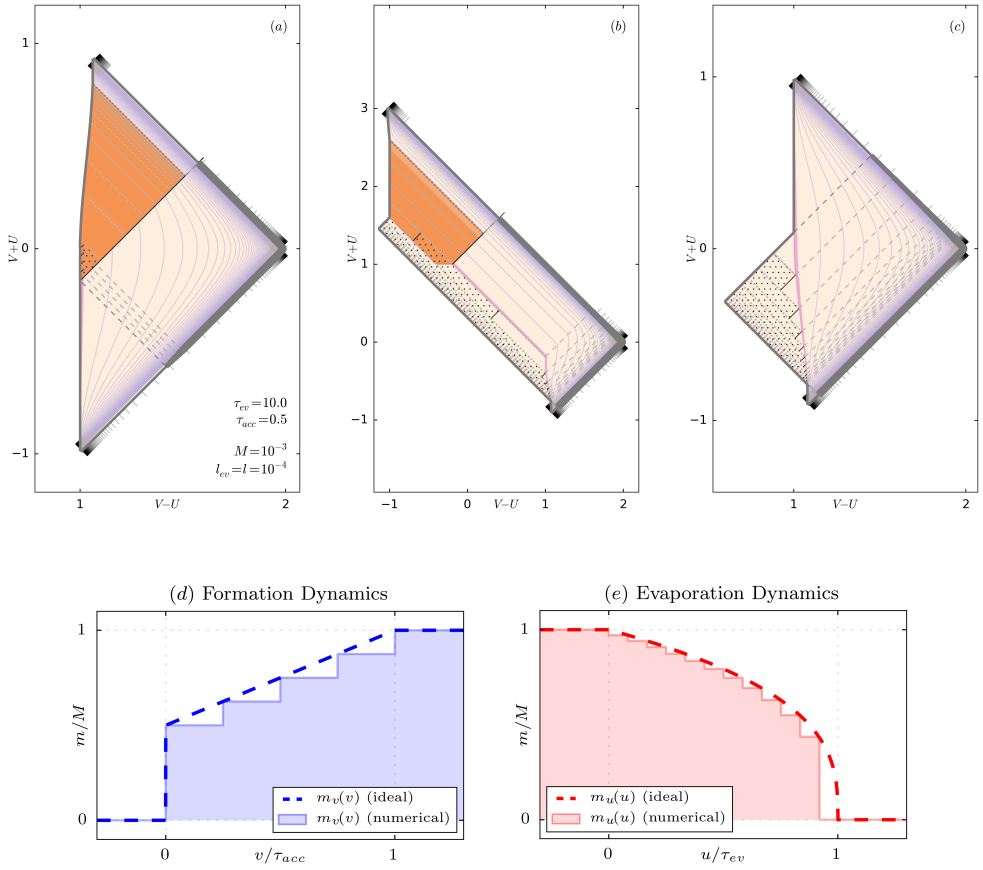

Figure 3.5: (Color online). Penrose diagrams for a nonsingular Hayward black hole which forms gradually then evaporates by slowly emitting thermal radiation with a standard time dependence (see (3.8-3.10)). The visualization scheme and associated legend are the same as in Fig. 3.4. As discussed in Section IV, these diagrams accurately capture both global and local (interior) structure, since they are constructed by directly finding a compact global double-null coordinate system for the spacetime. Although the three diagrams depicted in (a,b,c) appear vastly different, they all are derived from exactly the same spacetime — they have strictly the same causal structure, and are related by conformal transformations in the UV plane. [Caption continued on next page...]

Figure 3.5: [...Caption continued from previous page.] These "conformal" transformations are induced by coordinate transformations, so no geometric information is lost, see Section IV. While the conformal freedom in Penrose diagrams is well known, it is not widely recognized how drastically different these transformations can make the spacetime appear, or that no single diagram will clearly depict the various widely different timescales of BH evolution (formation, evaporation, Planck scale) simultaneously. Inevitably, in any diagram, some features will be squished beyond recognition; hence the need to compare multiple diagrams to gain a full understanding of the spacetime. Here, different transformations are used to highlight features (a) during accretion, (b) during evaporation, and (c) near the end of evaporation. In comparing the causal structure between them, note that some lines appearing null are only nearly null, and that some features are hidden by being very squished. For example in (a), the entire evaporation process (which includes important timelike features visible in (b,c)) is squished into a tiny, seemingly null, line. Similarly, parts of the high density region (orange) in (b), and all of the high density region in (c), are squished and hidden behind the future part of the nearly null segment of $r = 0$. The important qualitative features of these diagrams are summarized in Section VIII. Parameters were chosen to be as realistic as numerically allowed, providing a strong hierarchy of the formation, evaporation, and interior length/time scales (an overall scale factor is irrelevant). Since the BH length scales are so small compared to the evaporation rate, lines $r = const$ at $2M$ (magenta) and smaller length scales are very close together and each appear as a single bundle; an additional set of $r = const$ lines has been added with spacing $dr = \tau_{\rm ev}/20$ (faint purple) to display larger scales. Although some lines of constant radius may seem discontinuous, they are in fact just strongly kinked; their continuity can be confirmed by gradually adjusting the parameters from less extreme values. For example, faint purple lines approaching the evaporating horizon in (a) do not disappear, but closely hug the horizon in a bundle until reappearing in the far future region. The opacity of the tick mark near the moment of evaporation in (a) shows that many tick marks have piled up there; this is the phase pileup usually associated with Hawking radiation in particle creation calculations. The same phase pileup can be observed in (b,c); in all cases one expects interesting results wherever the dv ticks are very mismatched with traced-back du ticks. Panels (d,e) confirm that the numerically generated dynamics closely approximate the desired behavior.

independent outside the requirement

$$m_u(-\infty) = m_v(\infty) = M, \tag{3.7}$$

where M represents the total maximum mass of the BH.

The function $m_v(v)$ defines dynamics for the process of BH formation and accretion. The correct form is determined by astrophysical processes, and is of little interest to us here. As a rough estimate, we assume the BH accretes half its total mass in an initial burst at $v = 0$, then accretes the remainder linearly until a time $v = \tau_f$ when it is fully formed:

$$m_v(v) = \begin{cases} 0, & v < 0, \\ M\left(\frac{1}{2} + \frac{1}{2}\frac{v}{\tau_f}\right), & 0 < v < \tau_f, \\ M, & \tau_f < v. \end{cases} \tag{3.8}$$

Inspection of the diagrams reveals that during accretion, the outer horizon where $f(r) = 0$ is spacelike.

The function $m_u(u)$, meanwhile, defines the dynamics for BH evaporation. It is chosen to respect the thermal evaporation rate

$$\frac{dm}{du} \propto -m^{-2} \tag{3.9}$$

arising from blackbody radiation calculations in a Schwarzschild spacetime [69].

In particular, we choose

$$m_u(u) = \begin{cases} M, & u < 0, \\ M\left(1 - \frac{u}{\tau_{\rm ev}}\right)^{1/3}, & 0 < u < \tau_{\rm ev}, \\ 0, & \tau_{\rm ev} < u. \end{cases} \tag{3.10}$$

The location of $u = 0$ is set by the requirement that Hawking pairs nucleate just outside the horizon; a distant observer sees evaporation begin at the same moment they see the infalling shells fall through their own horizon. Once evaporation begins, the horizon is timelike.

While more realistic than the single-shell case, this is still only a toy model, meant to capture the commonly considered, highly idealized, case where an initially large spherical BH evaporates entirely by emitting blackbody radiation. The true spacetime of an evaporating BH is expected to differ in many ways, including corrections to the time dependence due to temperature-dependent emission effects and due to deviations from the Schwarzschild metric, as well as more intractable differences (like the necessity of including charge and rotation). Moreover, it seems likely that once an evaporating BH approaches the Planck scale its dynamics may be greatly modified. But in the absence of a widely accepted model for the BH end state, continuing Schwarzschild blackbody evaporation until the BH's disappearance seems like a conservative option. In any case, regardless of these details, this model should help attain an accurate qualitative picture of any BH emitting roughly thermal Hawking radiation during part of its lifespan.

Choosing a sequence of shells approximating the ideal accretion dynamics is trivial, but approximating the evaporation dynamics is slightly more involved. We consider the shell approximation successful if both $m_u(u)$ and $m_v(v)$ are reasonably

well approximated, with all evaporation shells nucleating at a fixed radial distance $l_{\rm ev}$ outside the apparent (outer) horizon r_+ of the region to its past (a basic assumption of our shell model). During evaporation, each shell nucleation point is defined by its coordinates (u, v, r) and (u', v', r') in the past and future regions containing it. Any two of (u, v, r) determine the third, and the radii $r = r'$ measured on each side must be equal. Regions between evaporation shells are characterized by their mass m and duration (du, dv) measured by observers at future and past null infinity. A suitable sequence of shell parameters is specified as follows. As a first estimate, we sample values at equal intervals of $u \in (0, \tau_{\rm ev})$ from the continuous dynamics

$$\begin{aligned} m(u) &= M\Big(1 - u/\tau_{\rm ev}\Big)^{1/3}, \\ r(u) &= 2\,m(u) + l_{\rm ev}, \\ v(u) &= u + 2\,F_S\Big(r(u), m(u)\Big), \end{aligned}$$

where $F_S(r, m) = r + 2m \ln\left|\frac{r}{2m} - 1\right|$ is a tortoise function [1] for a mass m Schwarzschild metric, yielding a sequence (m_i, u_i, v_i) of mass parameters and shell coordinates. The parameters thus obtained would be exact for a continuously evolving Schwarzschild spacetime, but are not quite consistent with our discretized (and possibly non-Schwarzchild) model; this is corrected by adjusting the u_i values to ensure that nucleation points lie exactly $l_{\rm ev}$ outside the outer apparent horizon. This process determines the discrete dynamics up to an overall time translation. One might expect that the small adjustment of u_i always leads to a valid approximation of the ideal dynamics, but in practice the method can break down if the BH mass and lifetime are not mutually consistent.[6] Whether the approximation

[6]Page has shown based on quantum and thermodynamic analysis that for an evaporating

was successful can be checked empirically; Figs. 3.5d–3.5e demonstrate that the desired continuous dynamics was correctly attained for the spacetime of Fig. 3.5.

Three different diagrams are needed to visualize different aspects of the spacetime in Fig. 3.5, due to the presence of vastly different timescales in the problem. Each panel corresponds to a different (conformally related) coordinate transformation in the UV plane, depicting the process as "viewed" from one of three different times. (The exact form of the coordinate transformations is determined by which region is used as the "seed" for a chain of shell matching transformations.) Together, they paint an intuitive picture. Early observers see the BH accrete mass, forming a BH with a long-lived nearly null horizon, behind which lies the dense core (space between the horizon and core exists but is squished away in this diagram). Intermediate-time observers looking far into the past see the outer surface of accretion shells shrouded by a horizon, with sparse Hawking radiation to their past and a final evaporation blast in their future. And late time observers simply see Hawking radiation emitted from a timelike horizon. The detail view of Fig. 3.6 emphasizes observers near the horizon at early times, and shows clearly the horizon transitioning from spacelike to timelike as accretion gives way to evaporation.

In the following section, we will see that a similar model can be extended to include cosmological models with nonzero background curvature.

Schwarschild BH one expects

$$\left(\frac{\tau_{\rm ev}}{t_{\rm pl}}\right) = A\left(\frac{M}{m_{\rm pl}}\right)^3,$$

where $A \sim 1000$ is a unitless constant determined by physical considerations [69]. (The precise value of A depends on various factors since the proportionality constant in the evaporation rate is, in less idealized cases, temperature dependent.) Our model seems to work well unless the nominal evaporation time is much shorter than dictated by this relation, with the Planck scale set by $l_{\rm ev}$ (in geometric units $l_{\rm ev} = l_{\rm pl} = t_{\rm pl} = m_{\rm pl}$). Since our model is purely geometric, the reason this relation must be enforced is not trivial.

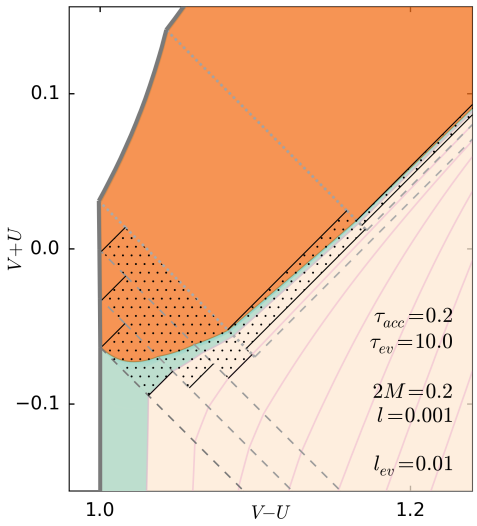

Figure 3.6: (Color online). Detail view of horizon and core dynamics during formation and the early stages of evaporation, for a spacetime similar to Fig. 3.5 but with somewhat less realistic parameters (in the sense that the mass and lifetime are not mutually consistent). Although the parameters are less realistic, the features depicted are qualitatively accurate. Details like these are not visible in more quantitatively accurate diagrams, where the extreme hierarchy of length and time scales prevents accretion and evaporation features from being depicted simultaneously. Compare to the region where accretion shells meet the core in Fig. 3.5a. Note that the apparently teal region is in fact a bundle of closely spaced lines of constant radius just outside the core.

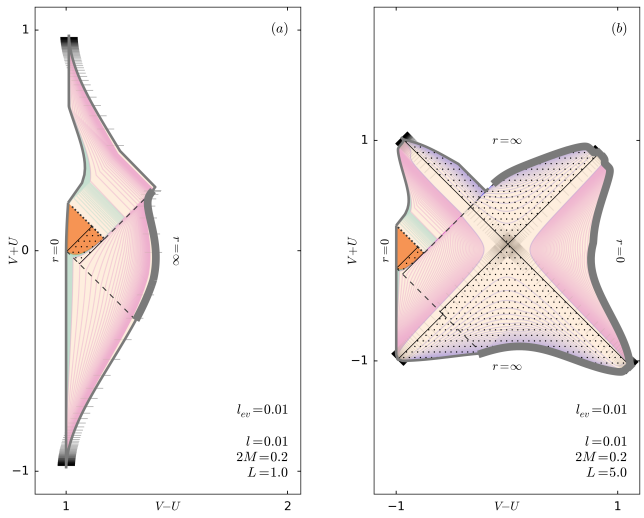

Figure 3.7: (Color online). Penrose diagrams for single-burst shell models with (a) negative and (b) positive background curvature, with metrics (3.11) corresponding to the Hay-AdS and Hay-dS BH spacetimes. Parameters were chosen for maximum visibility of qualitative features. Density color scale here depicts $\rho - \rho_{\rm bg}$, with constant background density $\rho_{\rm bg} = \pm 3/(8\pi L^2)$ (positive for dS). In (b), an additional set of lines $r = const$ (faint purple) have been added with spacing $dr = L/2$ to depict larger length scales. Note that, in addition to BH trapping, the dS case includes cosmological trapped regions having nothing to do with the BH. Tick marks no longer correspond to proper time, but still represent equal increments of du and dv. Notably, inspecting the tick marks shows that the phase pileup typically associated with Hawking radiation is still present in the u and v coordinates, even without the assumption of asymptotic flatness.

3.7 Diagrams including background curvature

While many discussions of BH evaporation assume, for simplicity, an asymptotically flat exterior, it is also interesting to consider BHs evaporating in alternative cosmologies. We therefore provide, in this section, Penrose diagrams for nonsingular BHs evaporating within asymptotically de Sitter (dS) and Anti de Sitter (AdS) spacetimes. Let us suppose, for both dS and AdS cases, that the background curvature is characterized by a length scale L such that $l \ll 2m \ll L$ (l and m being parameters of a Hayward metric, see above). That is, the black hole is small compared to background curvature length scales.

A nonsingular BH in a background of constant curvature may be described by (3.1) with

$$f(r) = 1 - \frac{2mr^2}{2ml^2 + r^3} \pm \frac{r^2}{L^2}, \tag{3.11}$$

which we refer to as the Hay-AdS (+) and Hay-dS (−) metrics. By fixing l and L while varying m across shells, we can construct single-burst forming and evaporating black hole models analogous to the flat space version of Fig. 3.4b. The results are depicted in Fig. 3.7.[7]

Having constructed single-burst models, the question arises of how to properly add continuous time dependence. Assuming $2m \ll L$, the spacetime is nearly asymptotically flat on length scales much smaller than L, and there is a class of observers, similar to distant Schwarzschild observers, for whom $2m \ll r_{\text{obs}} \ll L$ and $f(r) \approx 1$. It seems reasonable to assume that these nearly-asymptotically-flat observers should measure the usual thermal dependence, in which case the

[7]Maximally extending BH metrics in a dS background generically leads to an infinite chain of BHs and asymptotic infinities. To avoid this issue we modify the Hay-dS spacetime to transition to pure dS space far away from the BH. The transition occurs inside the cosmological horizon on the side of dS with no BH, and has no important effects.

earlier prescription in terms of $m_u(u)$ and $m_v(v)$ carries over unmodified. For a cosmologically-sized BH, however, how the detailed structure would look is less clear.

3.8 What is a black hole?

The causal structure encoded in these diagrams invites us to revisit a subtle question: *What is a black hole?* A number of authors, most famously Hawking [70], have already argued that the traditional global definitions (e.g. in terms of an event horizon) are not useful when evaporation is taken into account — and we will make a more detailed case for this proposition below. While the natural context for defining black holes is quantum gravity, to the extent that BHs have a semiclassical spacetime description, a general relativistic definition should be possible. To motivate an improved definition, let us review some of the features of the spacetime of Fig. 3.5:

(i) The spacetime has no event horizon, and is globally hyperbolic.

(ii) A distant external observer sees collapsing matter fall through its own apparent horizon in a finite amount of (the observer's) proper time. At the same moment the observer sees this crossing occur and the apparent horizon form, they begin to receive Hawking radiation (compare Figs. 3.4b, 3.5a, 3.6). In general, distant observers see Hawking radiation if and only if they are looking back at the apparent horizon.

(iii) Hawking radiation is emitted from a timelike surface (Fig. 3.5c). The emission surface is just barely outside the apparent horizon, which itself is also a timelike surface in the continuous limit (Fig. 3.5c).

(iv) The part of the diagram intuitively considered "part of the BH" consists of the trapped region and core. The trapped region is "trapped" in the sense that all future-directed curves are radially ingoing. The core is an ultradense quantum gravity plasma.

(v) During evaporation, the outer boundary of the trapped region is a timelike apparent horizon (Fig. 3.5c). During formation, a spacelike portion of the apparent horizon occurs inside the infalling matter (Fig. 3.6). External observers previous to the emission of any Hawking radiation see the apparent horizon as a nearly null surface in the future (Fig. 3.5a); in order to receive Hawking radiation, such observers must go "around the corner" to where the horizon appears timelike.

(vi) Some trapped observers, who have just barely fallen in, can escape the BH without intercepting the core by accelerating out of the trapped region during evaporation. Others, who have fallen too far in already, are doomed to destruction in the core. This "region of no escape" is quantified by the past domain of dependence of the core (the location of which can be inferred from Fig. 3.5b). The core surface is spacelike, while the boundary of the doomed region is null.

(vii) The inner boundary of the trapped region (the inner horizon) lies entirely within the core; it is timelike during accretion and spacelike during evaporation (Fig. 3.6). In the final moments of evaporation, the inner horizon, core surface, and outer horizon all come together.

(viii) The core maintains a constant Planck scale density. As the BH mass changes over time, the core, which for large BHs is significantly larger than Planck

scale in radius, adjusts in size to accommodate the total mass.

(ix) The proper time experienced at $r = 0$ within the core (to the extent that it corresponds to the classical value) is of the same order of magnitude as the BH lifetime experienced by distant observers. However, this could potentially be modified by altering the Hayward metric to include a redshift factor (see discussion surrounding (3.6)).

(x) Time evolution starting from initial data in the distant past and proceeding through the process of BH formation, accretion, and evaporation down to the Planck scale (including the emission of the majority of the Hawking radiation) can be described by a continuous family of Cauchy surfaces entirely to the past of the (quantum gravity) core (this is seen most clearly in Fig. 3.5c), on which semiclassical physics should apply. Evolution beyond the final moment of evaporation, when the BH disappears entirely, involves evolving Cauchy surfaces through the core, and requires a quantum gravitational description.

Inspired by the above observations, we propose a definition which depends on only local quantities and is consistent with all common black hole models: *A black hole is a future-trapped region surrounding and feeding into an ultra-dense core.*[8] Both the core and trapped region should be considered a part of the BH; one might propose to call this a *core and shroud* definition. Insofar as a singularity acts as a placeholder for a dense point mass, this definition includes both singular and nonsingular models.

[8]The phrase "feeding into" signifies that the inner future boundary of the trapped region lies on or within the core, and the phrase "surrounding" implies that the core lies within future light-sheets [71] of the relevant closed trapped surfaces. Recall also that the trapped region is "trapped" in the sense of trapped surfaces, not of "no escape."

This definition departs from tradition, by focusing on the trapped region and trapping (also called apparent, see appendix for definitions) horizon, rather than the region of "no escape to infinity" and corresponding event horizon. The traditional "event horizon" definition has several disadvantages. Most importantly, the location of an event horizon (which is typically defined as the boundary of the past of future infinity) is determined by the entire future history of the BH, and cannot be determined by any local data. Thus, even when it is clear that a "BH-like object" locally exists, the presence or absence of a BH by the traditional definition depends strongly on the BH end state (for example whether the BH later accretes additional mass, and whether the final dynamics are dominated by evaporation, remnant outcomes [43], mass inflation instability [45], or a bounce [44]). In contrast, the location of a core and trapped region can be determined by local data in a finite time.

Moreover, even without invoking nonsingular models, it's not clear that rotating or charged BHs form an event horizon at all when evaporation is taken into account. For example, the naive translation of Fig. 3.1 to a Reissner-Nordstrom metric leads to a naked singularity with no event horizon (such a diagram looks similar to Fig. 3.2b, see, e.g., [72, 73]). One possible rebuttal, that BHs should discharge and spin down before evaporating, is not very convincing, since spacelikeness of the Schwarzschild singularity is unstable to even continuously small perturbations of the charge and rotation parameters. If nonsingular models are adopted, then charged and (presumably, see [74]) rotating BHs have the same basic causal structure as the Hayward metric, and, as in Fig. 3.5, would exhibit no event horizon in our simple model. General nonsingular solutions should be expected to have a causal structure which is stable under perturbations of the rotation and charge, and to alleviate the pathologies of the interior Kerr-Newman metrics.

In the new definition, some conceivable BHs (which may or may not actually exist in nature), like the Schwarzschild BH of Fig. 3.4a, have an event horizon, while others do not. In the simplest case with an event horizon, where a Schwarzschild BH forms quickly then slowly evaporates without disturbance, the null event horizon is just barely inside the timelike trapping horizon (this fact can be inferred from Figs. 3.4–3.5, and checked numerically); the horizons nearly coincide. In other cases, for example if the BH forms, evaporates for some amount of time, then later accretes more mass, the event horizon and trapping horizon can be widely separated.

In any case, at least in our semiclassical model, energy conservation by the DTR relation forces Hawking radiation to be emitted from just outside locations where $f(r) = 0$ (in the Schwarzschild metric, $r = 2m$), so that Hawking radiation emission is directly tied to the boundary of the trapped spheres region. The boundary of the trapped spheres region is also the trapping/apparent horizon (see appendix), so the radiation can be thought of as emanating from the trapping horizon.

In any semiclassical model like our shell model, therefore, the Hawking radiation emission points must not be tied to the event horizon if they are to conserve energy. For instance, in the second case above, where a Schwarzschild BH forms, evaporates for some amount of time, then later accretes more mass, *the early Hawking radiation would be emitted from far inside the event horizon.* Such radiation would not make it to infinity, but could still be observable to distant observers for an arbitrarily long time before the second accretion event takes place. This observation provides further evidence that the trapping horizon is a more physical candidate than the event horizon to describe the BH boundary, motivating the new definition.

As discussed in the appendix, our trapped spheres region is the spherically symmetric special case of the more general "trapping nucleus," which is a special essential subset of the trapped region. The boundary of the trapping nucleus is, in general, the trapping/apparent horizon. It was previously argued from a trapped surfaces perspective (see appendix and [49]) that the trapping nucleus and its boundary provide the most reasonable definition for a BH and its horizon. The above observation about energy conservation in our shell model acts as a physically independent check supporting this hypothesis, making it likely that in similar but not-spherically-symmetric semiclassical models, Hawking radiation emission would need to come from just outside the trapping nucleus to conserve energy. Also, the nucleus is likely easier for an observer to identify than the full trapped region, since the nucleus consists of relatively trivial trapped surfaces and its boundary is marginally trapped.

While the nonsingular BH of Fig. 3.5 does not have an event horizon or region of no escape, the past domain of dependence of the core, which might be called the "doom region," plays a similar role. Any observer crossing into the doom region will inescapably be crushed into the ultra dense quantum gravity core before being emitted in the Hawking radiation. Notice that the boundary of the doom region in Fig. 3.4b almost exactly coincides with the event horizon in Fig. 3.4a, a phenomenon that holds generally when a Schwarzschild metric is replaced by Hayward. In this context, the singularity theorems show that doom regions are generic: matter which collapses through its own trapping horizon will inevitably continue collapsing until quantum gravitational effects kick in, forming a core and associated doom region.

By focusing on the properties of a BH as an actual compact object that can form and exist at a finite time, the new definition allows a broader and more

useful class of objects to be called BHs, like evaporating charged, rotating, and nonsingular metrics, BH-like objects which later bounce or form a remnant, and collapsed stars whose exact metric and eventual end state is unknown. In turn, this allows the study of when certain pathologies of BH metrics, like singularities, event horizons, and Cauchy horizons, do and do not arise. Defining BHs (which we fundamentally know to exist only as compact astrophysical objects) by insisting on their worst pathologies is one reason that questions of unitarity and information preservation during evaporation have remained unresolved.

3.9 Towards a self-consistent evaporation model

Significant attention has been given recently to the question of self-consistent BH evaporation models (related examples include [75, 76, 77, 78, 79]). Typically the idea is to postulate an evaporating BH spacetime, treat it as a fixed background for a quantum field theory, and show that a renormalized stress tensor for the field theory matches the background curvature — or at least find some evidence that the field theory and background are compatible. It is our hope that the present diagrams, especially Fig. 3.5, can help inform this effort.

In particular, for example, the model presented here suggests an improvement to the recent interesting calculation by Frolov and Zelnikov, who have studied the quantum radiation from an evaporating modified Hayward metric [78, 79]. They found, in addition to the Hawking radiation, an unwanted burst of radiation emanating from the inner horizon. Moreover, the burst was found to be at least partially mitigated by certain changes to the metric. Our model suggests even further changes to the metric. Specifically, time-dependence in this study was included only by virtue of a function $m(v)$ depending on the time parameter at

past null infinity, which was assumed to have the usual thermal-evaporation time dependence. This has two drawbacks. First, it is observers at *future* null infinity, *receiving* the Hawking radiation, who should measure the correct thermal time dependence — not those in the past. That is, it is $m(u)$, not $m(v)$, that should be thermal during evaporation. And second, using only $m(v)$ implicitly assumes that evaporation occurs by absorption of negative mass shells *incident from infinity*, when they should rather be incident from near the horizon. A more physical metric would include a more complicated time dependence, depending on both u and v simultaneously. The proposed change is drastic enough to hope that, coupled with an expeditious choice of redshift function, it could help the model approach self-consistency.

Related to the study of self-consistent models, and to the unwanted energy outburst discussed above, is the phenomenon of mass inflation, in which large amounts of gravitational energy are converted into mass by the collision of null shell perturbations in a BH [45].

The cause of mass inflation can be understood as follows. Consider the shell collision depicted in Fig. 3.8. Two spherical null shells, each of mass Δm, collide, with initial and final Schwarzschild masses m and M respectively. If the collision occurs *outside* the BH horizon, where future-directed shells come in a radially-ingoing/radially-outgoing pair, then the requirement that all shells have positive mass ensures that $|M - m| < \Delta m$. This makes sense since an ingoing (outgoing) positive-mass shell will increase (decrease) the mass of a Schwarzschild region to its future, so that the shell masses roughly cancel out in the final state. But if the collision occurs *inside* the black hole, both incident shells are radially ingoing: they both contribute positively to the final mass. Working out the associated constraints shows that in this case, even when all shell masses are positive, the

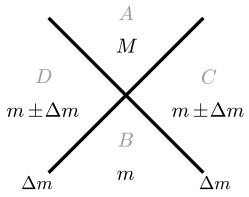

Figure 3.8: Two spherical null shells colliding in a spherically symmetric spacetime. Gray lettering indicates the standard labelling of each region in DTR calculations (see appendix). Black lettering describes an example: Two shells, each of mass Δm, collide, in an initial Schwarzschild spacetime of mass $m_B = m$. Assuming A, B, C, D are all Schwarzschild spacetimes, the masses m_C and m_D are fixed by shell junction conditions, with signs determined by whether each shell is radially ingoing (+) or outgoing (−) towards the future. The final mass $m_A = M$ is determined by the DTR relation. Assuming all shells (both initial and final states) have a positive mass, mass inflation can occur only if both shells are radially ingoing — for instance, inside the trapped region of a BH. Otherwise, restricting to positive-mass shells ensures that $|M - m| \leq \Delta m$.

final mass M can be arbitrarily large. When both incident shells are ingoing and the collision occurs near $f(r) = 0$ (i.e. near a horizon), application of the DTR relation (see appendix) shows that even very small incident masses will lead to an unbounded increase in M: this allows the mass inflation.

There is an open question of whether mass inflation at the inner horizon creates an instability which significantly alters the dynamics or interior metric [80]. Our model suggests a few more remarks on this topic.

First, the mass inflation instability is often associated with a part of the inner horizon, the "outgoing" inner horizon [80], which does not actually exist in evaporating BH spacetimes like ours or Hayward's. This outgoing horizon, which acts as the Cauchy horizon in simple collapse models, is the part of the inner horizon approached by right-directed (in the standard diagram, see Fig. 1 of [81]) null rays in an eternal charged or nonsingular BH metric. (These rays are technically ingoing despite the nomenclature.) This part of the horizon exists in the eternal

metric, but is cut off by an incoming negative-mass shell in our Fig. 3.2b, and cut off by the smooth evaporation process in Hayward's model. The evaporating models also have no Cauchy horizon for the same reason. While it is not impossible for a right-going shell in our model to approach the inner horizon, such shells typically emanate directly from an earlier part of the same inner horizon, and do not intersect the "outgoing" part of the horizon as usually assumed.

This is not an argument that mass inflation does not occur. But it does lead to a delicate situation. It is common to study mass inflation within the causal structure of an eternal BH spacetime where the outgoing inner horizon exists (for a clear example see [82]). But if an evaporating spacetime is assumed, some of the assumptions underlying these calculations may break down. On the other hand, it has previously been argued both that mass inflation does not depend on the long term future [80], and that evaporation should fail to prevent mass inflation once corrections to the Schwarzschild evaporation rate are taken into account [82], possibly circumventing the issue we are raising. However since both still make the assumption described, the resolution may or may not be definitive.

Second, if curvature is assumed to be regulated by a Planck scale density cutoff, then in nonsingular models with sufficiently low charge and rotation (like the Hayward metric), the entirety of the inner horizon is hidden far within the quantum-gravity-dominated core. Any calculations based on semiclassical physics near the inner horizon must therefore be called into question in these cases. Further, if the result of mass inflation is meant to be the development of an extreme density at the inner horizon [81], it is not clear that any such higher density could be reached. This disrupts the interpretation of mass inflation in static nonsingular cases (as in, e.g. [82]). On the other hand, it is possible that rotating and charged nonsingular BHs have an inner horizon extending outside the core [74],

so the issue still must be dealt with unless there is a sufficient mechanism for discharge/spin-down.

3.10 Possible implications for the physics of black hole evaporation

The questions we feel it natural to ask about BH evaporation can change drastically depending on what spacetime diagrams are used. In the traditional diagram, for example, it's natural to ask: *Is there a unitary transformation connecting the quantum states at future and past null infinity?* But in the nonsingular evaporation diagrams presented above, which have been constructed to be globally hyperbolic, it's almost obvious that such a transformation ought to exist between any two Cauchy surfaces not intersecting the ultra-dense quantum gravity region (where it doesn't seem safe to assume known physics applies). These new diagrams, on the other hand, raise a different fundamental question: *What is the nature of the negative-mass shells?*

A global, phenomenological, and ultimately unfulfilling answer to the latter question already exists. As shown most clearly by Davies, Fulling, and Unruh (DFU), quantum field theories yield an ingoing negative energy flux in a renormalized stress tensor near the horizon when a BH is present [39]. Clearly, the presence of this ingoing negative flux (and of our ingoing negative-mass shells) is a phenomenon of quantum field theory in curved spacetime. But the calculation is global. Can this phenomenon be understood as a local process? How should the negative flux be interpreted physically?

Suppose we answer these questions with a bold but simple interpretation: that

the negative-mass shells represent normal matter propagating out from the core on non-future-directed (i.e. past-directed or spacelike) trajectories.[9]

With a little justification, this seems like a reasonable claim. It is well known that quantum field theories (QFTs) violate, by small amounts, the classical energy conditions, including energy conditions intended to prevent the non-causal transfer of energy [61]. The fact that these theories violate the energy conditions is closely tied to the faster-than-causal spreading of relativistic wavepackets in the one-particle sector of QFT [83, 84]. In this sense, energy condition violations are related to a small amplitude for QFT particles to propagate, or in a probability interpretation "tunnel," faster than light. For there to be a non-negligible probability of escape from the core by this process, wavepackets must spread beyond the trapping radius, so that escaping field modes have wavelength on the order of the BH size. As the BH gets smaller, the amount of non-causal propagation needed to escape is reduced, and the process becomes more probable, so evaporation speeds up. Normally the non-causal propagation is overwhelmed by much more likely causal propagation, but a BH makes escape by causal propagation impossible.[10]

In case of the DFU stress tensor, energy conditions are violated due to an ingoing flux of negative mass into the horizon, which, in this picture, would correspond to a non-future-directed transfer of energy out from the BH core. While it's not unusual for QFTs to violate energy conditions, what's unusual about BH

[9] A classical connection between negative mass and non-future-directed propagation is fostered by calculating the energy flux vector $F^\mu = -T^{\mu\nu}\, t_\nu$ relative to a timelike observer for a uniform dust of density ρ with velocity u^μ and stress tensor $T^{\mu\nu} = \rho\, u^\mu u^\nu$. Both $\rho < 0$ and $u^2 > 0$ lead to non-future-directed energy flux.

[10] It must be noted that using any language of "particles" (or even "quanta") is extremely dangerous in this context, due to the many well-known ambiguities surrounding QFT particles in curved spacetime [51]. The field picture must be given conceptual priority. If not taken too literally, however, particle language can sometimes provide a useful heuristic. When we use the particle terminology here, it is mainly to make connection with standard language of the literature.

evaporation, in this picture, is that non-future-directed propagation dominates the dynamics. (In Fig. 3.5, this refers to matter being carried out on the negative mass shells, instead of emerging through the future boundary of the core.) The fundamental question, then, is shifted to one that more directly implicates the paradoxical nature of BH evaporation: *Why does matter escape from the core exclusively, or at least primarily, on non-causal trajectories?*

The answer to this question might be more straightforward than it seems. As discussed already, even under normal circumstances QFTs violate energy conditions in ways that may allow energy to locally propagate on non-causal trajectories. If the lightcone of some matter is blocked by a strong space-and-time-dependent potential barrier, can causal propagation be significantly depressed? If so, could the small energy-condition-violating flux add up to a significant transfer of mass outside the lightcone? And does the BH core metric (specifically, the rapidly changing metric where the extremely dense core meets the future post-evaporation vacuum, see Fig. 3.5) act as such a barrier when coupled to a quantum field? (Alternately,[11] could this process be a phenomenon of quantum gravity?) These questions have not yet, to the authors' knowledge, been addressed; they

[11]In the semiclassical model we are suggesting, $\langle T_{\mu\nu} \rangle$ corresponds to a scenario where matter exits the core on spacelike trajectories, as opposed to propagating directly through the future boundary of the core. One way to make sense of this may come from quantum gravity. Consider, heuristically, a path integral formulation for the complete quantum gravitational system, and consider some tunnelling calculation where a nonsingular BH tunnels into an evaporated state at a later time. What paths (in some quantum gravity configuration space) contribute to this process? There are some paths where matter in the core propagates timelike while the metric remains static — these paths correspond to a purely classical evolution, but don't contribute to the tunneling process, because they only contribute to an "eternal BH" configuration of the metric. That is, paths with timelike matter propagation in the core correspond to classical scenarios where matter sits in the core forever, not situations where matter leaves the core and the BH evaporates. Among paths where the metric looks like an evaporating BH, it's possible that paths with spacelike propagation are less suppressed than other off-shell contributions, for example less suppressed than configurations that drastically violate Einstein's equation. If this were the case, one could think of quantum gravity as creating a quantum correlation between BH evaporation in the metric, and spacelike propagation in the matter fields.

should be.

This line of reasoning is open to an obvious criticism: The presence of a Hawking flux depends (in curved-spacetime quantum field theory calculations) only on the presence of the horizon, and therefore cannot depend on physics in the core. This is an important observation, but, although it may seem so at first glance, it is not especially damning to the interpretation. Actually, the only details of core physics relevant to this discussion are two assumptions already implicit in singular BH models: that once an apparent horizon forms, gravitational collapse to a singularity (core) is inevitable; and that future-directed propagation out of the singularity (core) is not allowed. Moreover, if BH evaporation is truly unitary, the matter emitted in Hawking radiation should be, in some sense, "the same" matter that formed the BH in the first place. This point is almost always neglected in discussions of particle creation by a horizon.

The key to reconciling the fact that the Hawking flux depends only on the presence of the horizon, and the fact that matter emitted in Hawking radiation should come from the core, is self-consistency between the background spacetime and the quantum field theoretic stress tensor. This is closely tied to the question of why BH horizons supposedly evaporate, while Rindler horizons (for accelerating observers in flat space) do not.

In the Rindler vacuum, the renormalized semiclassical stress tensor $\langle T_{\mu\nu} \rangle$ bears no resemblance whatsoever to the Einstein tensor of the flat background metric [85]; it should not, therefore, be regarded as a solution of the joint matter-gravitational field equations. But in BH evaporation, the renormalized stress tensor for the in-vacuum closely resembles the Einstein tensor of our shell model.[12]

[12]Statements like these are ambiguous when there is ambiguity in the stress tensor renormalization scheme. For the present qualitative purposes, suppose the field equations aren't satisfied unless some reasonable renormalization scheme is shown to produce a stress tensor equivalent

One can imagine an iterative process, where the background spacetime is perturbed to approach the renormalized QFT stress tensor at each step, converging on a self-consistent model of an evaporating BH spacetime coupled to the matter field. Starting such a process from a non-evaporating BH spacetime in the usual in-vacuum, one obviously expects the horizon to start evaporating during the iterations due to the ingoing negative flux. But there is no reason to think that this should be the only effect, or that an initially vacuum region of spacetime should be empty when the process converges. (Note that "initially" here refers to iterations, not to time.) Presumably, assuming some usual in-vacuum state, the presence of the BH horizon is *not only* sufficient to predict Hawking-like radiation, *but it is also sufficient* to predict the existence of a core which forms and then evaporates.

How does this observation apply to Rindler horizons in Minkowski space, and cosmological horizons in de Sitter? Let's look closer at the analogy. First of all, from a non-technical standpoint, it makes no sense for either of those horizons to generically emit radiation,[13] since both of the spacetimes are homogeneous — every point in de Sitter spacetime lies on a cosmological horizon. More technically, the emission or not of radiation, and the evaporation or not of the horizon,

to the metric.

[13]This is separate from, but often confused with, the question of radiation experienced by an accelerating particle detector. Particle detector calculations (see [51] for review) like the famous results of Unruh [86] and Gibbons and Hawking [87] do not deal with objective radiation existing in the spacetime and quantum state, but rather with the coupling a of a local detector to a quantum field. This conceptual distinction was made very clear, for example, by Padmanabhan and Singh [88]. The excitations of such a detector should be attributed to a combination of two effects: the difference between the global quantum state (perhaps a global "vacuum") and an observer's local inertial vacuum (that is, some state with no particles in modes defined by an observer's local inertial frame); and the observer's acceleration relative to that frame. Davies and others have suggested a useful paradigm: that the detection of particles due to acceleration be thought of as a form of "vacuum friction" [89, 90]. The relation of particle detector calculations to thermal emission by a horizon is evident only in special cases, where constant acceleration or a particular choice of positive frequency modes creates a useful analogy.

depends on the quantum state. This is obvious, but there is a key point missing from standard discussions of this issue. States where the renormalized stress tensor is highly mismatched from the background Einstein tensor *are probably never realized*, since they are not likely to be solutions of the joint matter-gravity field equations (whatever that means in quantum gravity). Yes, there are states where Rindler, cosmological, or other Killing horizons emit radiation. But they are not solutions of the joint equations of motion unless an iterative process is performed to match the background metric with the stress tensor. Perhaps these states converge to BH solutions, perhaps to something else, or perhaps they don't converge at all. Either way, in the special case of Rindler, cosmological, etc. horizons, the first iteration step is likely to drastically change the qualitative picture and call the horizon interpretation into question. In contrast, iteration towards self-consistency in the BH case reinforces the qualitative picture of a BH evaporating while emitting Hawking radiation. The BH case, unlike the other cases, appears to admit a *self-consistent* picture of an evaporating horizon.

It seems likely that, starting from an evaporating nonsingular spacetime like Fig. 3.5, the iterative process described above has at least a pretty good chance to converge to something reasonable, given the qualitative similarity between the DFU stress tensor and the stress tensor for our shell model. It's not clear that the same can be said for the more traditional spacetime where shell collapse results in an eternal Schwarzschild BH. Would the iteration process ever provide the drastic change in causal structure needed to account for the BH disappearance at the end of evaporation? If not, then performing QFT calculations in a singular non-evaporating background, while useful for gaining general intuition, is useless for obtaining a complete description of the BH evaporation process. To get legitimate candidates for a self-consistent description, QFT should be performed in

spacetimes like Fig. 3.5. Various efforts are making interesting progress in this direction, especially [78, 79], as discussed in previous sections. Moreover, a similar criticism can be applied to some of the firewall arguments: quantum firewall states calculated in a vacuum spacetime are not self-consistent.

There is one more key point which has not been addressed, relating to the fact that the matter in Hawking radiation should be "the same" matter that fell in, and, consequently, relating to self-consistency of the semiclassical BH solutions. In all standard calculations, the matter which falls in to form the BH, and the matter in which the Hawking radiation is present, are regarded as *separate matter fields*. This is implicit when the background metric is assumed, in which case the infalling matter field is non-dynamical. A more conceptually accurate treatment would treat infalling matter as a true quantum field, with this being the only matter field in the problem. Then the true quantum in-state is not an in-vacuum, but a collapsing-star state. One still expects to find the Hawking radiation, but its source and backreaction effect would, presumably, be less mysterious. It may be the case that the standard calculation is appropriately regarded as a perturbation in this scenario. But the consequences of resolving this oversimplification have never been adequately settled.

Setting aside the discussion of its validity, assuming the non-future-directed-trajectory interpretation we have here espoused would lead to the following narrative of BH evolution: A star collapses beyond its Schwarzschild limit, forming a trapped region. Once the trapped region is formed, continued collapse is inevitable until quantum gravity takes over the dynamics, at which point a tiny core of Planck scale density is formed. The future boundary of the core acts, by some currently unknown mechanism associated with the core's extreme density, as a local space-and-time-dependent potential barrier, suppressing causal propa-

gation of matter out of the core, and forcing matter propagation to be dominated by non-causal paths exiting the core through its spacelike outer surface. Thus, having effectively no other option, matter from the core slowly leaks (or "tunnels") out on these non-causal paths, gradually depositing the BH mass at infinity in the form of a Hawking flux. Matter falls in, gets decomposed in the fires of quantum gravity, and, retaining unitarity, eventually comes back out. In terms of relativistic causal structure, in this picture there is no profound difference between a BH and other objects; black holes are unusual only in that much of their interior is empty and contains trapped surfaces, in that their matter is confined to a tiny volume where quantum gravity dominates, and for their low luminosity-to-mass ratio. In this picture, black holes are not that weird.

We are not the first to propose a picture like the one presented throughout this section. As far back as the original discovery of the Hawking effect, similar ideas were invoked in [38], and by various comments of [36, 37] (though the particulars there are rather hazy, especially regarding different types of energy), as well as many others. It has not previously, however, been taken seriously as a semi-local physical description in the context of self-consistent evaporating nonsingular models. These models have the advantage that matter tunneling out has somewhere to come from, with an energy-conserving backreaction.

Whether the above is a useful or accurate story is undecided. It does, at least, seem qualitatively aligned with both the DFU stress tensor and the tunneling picture of Parikh and Wilczek [91] (the key step of which is a tunneling event in which some internal matter crosses the horizon), as well as with [36, 37, 38] as previously noted, and doesn't seem to raise any major philosophical issues. In any case, the most appealing aspect of this description is surely its simplicity.

3.11 Concluding Remarks

Spacetime diagrams invariably have a profound influence on our thinking about relativistic systems, and especially black holes (BHs). The goal of this article is to disrupt an unfortunate status quo: the use of diagrams not tied to any particular spacetime model. Ambiguous hand-drawn diagrams (most perniciously those attempting to depict BH formation and evaporation in a single picture) too often reflect the biases of the artist, and result in misleading intuitions — for example that Hawking radiation emanates from (just outside) a null event horizon, or that external observers take an infinite proper time to see infalling matter fall in. False intuitions like these can lead to incorrect or circular reasoning about subtle questions. To clarify these issues, we have argued for the use of well-defined models in which verifiable claims can be made. Our "shell model," as it has been dubbed above, presents an attempt at a simple and minimal concrete model for BH formation and evaporation, which seems to capture most generic aspects of the problem, and for which Penrose diagrams can be explicitly obtained. Based on the results, we have argued for an improved definition of the term "black hole," and proposed a more straightforward interpretation of the mechanism of Hawking radiation. While we make no claim of the absolute veracity of our shell model, we do hope it brings to light some new questions about the BH evaporation process, and stimulates a more concrete and physically grounded discussion.

3.12 Appendix: Matter content of Shell Models: General Case

Numerically computing Penrose diagrams allows the distribution and flow of matter to be quantitatively visualized in the diagram, assuming Einstein's equation $G_{\mu\nu} = 8\pi T_{\mu\nu}$. There are two contributions to the matter content: matter associated with the shells, and matter associated with the quasistatic equilibrium solutions.

3.12.1 Quasistatic Contribution

First we consider the matter associated with the equilibrium solutions. For our purposes, all such solutions take a metric of the form

$$ds^2 = -f(r)\,dt^2 + f(r)^{-1}\,dr^2 + r^2\,d\Omega^2\,, \tag{3.12}$$

where $f(r)$ is an arbitrary function called the *metric function*. Metrics of this type can be either singular or nonsingular at the origin. A number of equivalent conditions for singularity are given by [1, app. E]; here it suffices to say that the metric is *nonsingular* whenever $f(r) = 1 + \mathcal{O}(r^2)$ as $r \to 0$, a condition which implies finiteness of curvature scalars, geodesic completeness, and existence of a Cartesian metric, in a neighborhood of the origin [1]. Although classical theorems predict singularity formation in gravitational collapse [60], nonsingular solutions are thought to arise in effective semiclassical approximations if quantum gravitational effects regulate curvature at the Planck scale. Our method applies to both singular and nonsingular models; nonsingular models have the advantage that all matter is made explicit in the stress tensor, whereas singular solutions

contain a matter contribution hidden in the singularity.

Curvature. A detailed anaylsis of the matter content for metrics of the form (3.12) was carried out in [1]. The following is a summary of those results. To expedite the analysis, it is best to define a *mass function* $m(r)$ by

$$f(r) = 1 - 2\,m(r)/r, \tag{3.13}$$

and define an orthonormal basis $\hat{e}_a$ by

$$\begin{aligned}
\hat{e}_0 &= \begin{cases} \sqrt{f(r)^{-1}}\;\partial_t & , f(r) > 0, \\ \sqrt{-f(r)}\;\partial_r & , f(r) < 0, \end{cases} \\
\hat{e}_1 &= \begin{cases} \sqrt{-f(r)}\;\partial_r & , f(r) > 0, \\ \sqrt{f(r)^{-1}}\;\partial_t & , f(r) < 0, \end{cases} \\
\hat{e}_2 &= r^{-1}\;\partial_\theta, \\
\hat{e}_3 &= (r\sin\theta)^{-1}\;\partial_\phi\,.
\end{aligned} \tag{3.14}$$

In this basis $\hat{e}_0$ is always timelike. Both $\hat{e}_0$ and $\hat{e}_1$ can be continuously extended across the horizons where $f(r) = 0$, but the full basis cannot, since the extensions of $\hat{e}_0$ and $\hat{e}_1$ would coincide at the horizon. In this $\hat{e}_a$ basis, the Einstein tensor is diagonalized, with components

$$G^a{}_b = 8\pi\;\mathrm{diag}(-\rho, -\rho, p_\Omega, p_\Omega), \tag{3.15}$$

where

$$\rho = \frac{m'(r)}{4\pi r^2}, \qquad p_\Omega = -\frac{m''(r)}{8\pi r}. \tag{3.16}$$

Physically, this amounts to a proper density ρ, a transverse pressure $p_t = -\rho$, and an angular pressure p_Ω. The common curvature scalars follow, as

$$\begin{aligned} K_0 &\equiv R = 16\pi\,(\rho - p_\Omega), \\ K_1 &\equiv R_{ab}R^{ab} = 128\pi^2\,(\rho^2 + p_\Omega^2), \\ K_2 &\equiv C_{abcd}C^{abcd} = 12\,\eta^2/r^4, \\ K_3 &\equiv R_{abcd}R^{abcd} = K_2 + 2\,K_1 - (1/3)\,K_0^2, \end{aligned} \tag{3.17}$$

with $\eta = 2\,m(r)/r - 4\,m'(r)/3 + r\,m''(r)/3$. Contributions to the curvature from a singularity, if one exists, are included in K_2, and $f(r) \equiv 1$ if and only if $K_1 = K_2 = 0$ everywhere. A complete specification of the Riemann and Weyl curvature components, in addition to Christoffel symbols, may be found in [1].

Energy conditions. Nonsingular black hole solutions often violate classical energy conditions—this is one way to evade the singularity theorems [60]. One approach to this situation is to take both the nonsingular metric and its energy condition violations seriously, assuming they provide useful insight about the physical mechanism of evaporation. Although classically unorthodox, this approach is appealing since quantum field theories are already well known to predict energy condition violations [61]. Regardless of one's view on this matter, it is useful to keep track of where and by how much energy conditions are violated in a given solution. We concern ourselves here with the null (NEC), weak (WEC), and flux (FEC) energy conditions, defined by [61]

$$\begin{aligned} &\text{(NEC)} \quad G_{ab}\,k^a k^b \geq 0 \ \text{ for all null } k^a, \\ &\text{(WEC)} \quad G_{ab}\,t^a t^b \geq 0 \ \text{ for all timelike } t^a, \\ &\text{(FEC)} \quad -G^a{}_b\,t^b \ \text{ causal for all timelike } t^a. \end{aligned} \tag{3.18}$$

The WEC ensures timelike observers measure locally positive mass density, with the NEC as its null limit; the FEC ensures no timelike observer measures a spacelike energy flux. Given the diagonalized Einstein tensor (3.15), these reduce to the simple inequalities [61]

$$\begin{array}{ll} \text{(NEC)} & \rho + p_\Omega \geq 0, \\ \text{(WEC)} & \text{NEC plus } \rho \geq 0, \\ \text{(FEC)} & \rho^2 - p_\Omega^2 \geq 0. \end{array} \tag{3.19}$$

The degree to which these conditions are violated is quantified by the functions

$$\begin{aligned} \chi_{\text{NEC}} &= -\min(\rho + p_\Omega, 0), \\ \chi_{\text{WEC}} &= -\min(\rho, 0), \\ \chi_{\text{FEC}} &= -\min(\rho^2 - p_\Omega^2, 0), \end{aligned} \tag{3.20}$$

called the *energy condition violation functions*. These functions are the obvious extensions of the above inequalities, but their physical status as quantifiers requires some clarification. They are justified as follows. Consider observers associated with a null velocity k_a and a normalized timelike velocity t_a, and the flux vector $F^a = -G^a{}_b\, t^b$ relative to t^b (note that the FEC is equivalent to $-F_a F^a \geq 0$). One then finds that

$$\begin{aligned} G_{ab}\, k^a k^b &= ((k_2)^2 + (k_3)^2)\ (\rho + p_\Omega), \\ G_{ab}\, t^a t^b &= ((t_2)^2 + (t_3)^2)\ (\rho + p_\Omega) + \rho, \\ -F_a F^a &= ((t_2)^2 + (t_3)^2)\ (\rho^2 - p_\Omega^2) + \rho^2. \end{aligned} \tag{3.21}$$

Thus, for a given observer, the functions χ_{NEC} and χ_{WEC} quantify the amount of measured negative mass density, and the function χ_{FEC} quantifies the spacelike-ness

of the energy flux. Interestingly, when $\rho > 0$, only observers with large angular momentum will observe strong energy condition violations. This quantification scheme is in line with the standard definitions for semiclassical energy conditions [61], which usually amount to enforcing a small positive bound on our energy condition violation functions.

Trapped surfaces, horizons. An important characteristic of black hole spacetimes is the existence of closed trapped surfaces (see [92] for a useful review); their existence is associated with the trademark "inevitability" of black hole collapse. Naively, in applying the theory of trapped surfaces to study black holes, one basically wants to identify the region containing trapped surfaces and determine its boundary. The boundary of the trapped region in spacetime is sometimes called a "trapping horizon," while the boundary of the region of trapped surfaces contained entirely within a spatial slice is often called an "apparent horizon." These naive definitions capture the right essential spirit, but fall somewhat short at a technical level, mainly due to the possibility of strangely shaped trapped surfaces and the associated issue of "clairvoyance" [92]. Fortunately, an illuminating and thorough discussion of these issues, and their application to black hole spacetimes, has been carried out by Bengtsson and Senovilla [49]. They have determined that the trapped region, which is unreasonably global due to clairvoyance, contains an essential and physically relevant subregion called "the core of the trapped region," which we refer to here as the *trapping nucleus* (to distinguish it from the entirely unrelated "matter core" in the Hayward metric). The trapping nucleus is defined as a minimal region which, if removed from the spacetime, eliminates all trapped surfaces. That is, any trapped surfaces in spacetime can be blamed on the nucleus, even if they extend outside it. This definition is especially vindicated by the fact

that the boundary of the trapping nucleus is a unique (modulo some technicalities, see [49]) surface in spacetime foliated by traditional apparent horizons. It is on this trapping nucleus that we focus our attention in defining the black hole horizon: we shall refer to the boundary of the trapping nucleus interchangeably as the *trapping horizon* or *apparent horizon*, depending on context. Intersecting this horizon with a spatial surface yields an apparent horizon in the traditional sense. Bengtsson and Senovilla have argued that the trapping nucleus and its boundary provide the best trapped-surfaces definition of a black hole and horizon.

Trapped spheres. Following [49], an arbitrary spherically symmetric spacetime can be expressed in the Eddington-Finklestein form

$$ds^2 = -e^{2\beta}\,(1 - 2m/r)\,dv^2 + 2e^{\beta}\,dv\,dr + r^2\,d\Omega^2, \tag{3.22}$$

where $m = m(v, r)$ and $\beta = \beta(v, r)$. Expressed this way, the trapping nucleus (see above) is the set $r < 2m$ and its boundary is $r = 2m$. In our shell model, these correspond to the set $f(r) < 0$ and its boundary $f(r) = 0$. This nucleus is precisely the region in which spheres about the origin of spherical symmetry are trapped [1, 49]. To avoid unfamiliar terminology, we refer to this region (which is both the trapping nucleus and the set of points where the sphere (t_0, r_0, Ω) is a closed trapped surface) in the main text as the *trapped spheres region*. If there were no spherical symmetry, we would instead simply focus on the more general trapping nucleus for equivalent purposes.

Trapping and horizons: summary. The trapped region surrounding a black hole has an indispensable interior subset called the trapping nucleus, whose boundary is the apparent (also called trapping) horizon. In our shell model, the trapping

nucleus exactly coincides with the trapped spheres region $f(r) < 0$, so that the apparent horizon is exactly at $f(r) = 0$. For metrics with a nearly-Schwarzschild exterior of mass m_0, this implies the apparent horizon is almost exactly at $r = 2m_0$.

3.12.2 Shell Contribution

The junction hypersurface connecting two properly matched piecewise-defined regions of spacetime in general corresponds to a thin shell of matter. This is described technically by a distributional contribution to the stress tensor of the joint spacetime. For the purposes of this article, we consider shells arising from the junction of spacetimes of the form (3.12) along radial null hypersurfaces (excluding the horizon-matching case where $f(r) = 0$ everywhere). The stress tensor for this setup was calculated in [1] by application of the null shell formalism of Barrabes and Israel [93]. The result is most concisely described using local Eddington-Finklestein coordinates in a neighborhood of the junction shell, defined as follows. Consider a local patch M_0 of the joint spacetime, which is separated into a past region M_- and future region M_+ by the null junction hypersurface Σ, with metric functions $f_\pm(r)$ in the two regions. As shown in [1], it is possible to choose a joint coordinate system (w, r, Ω) on M_0, such that the shell Σ is defined by the level set $w = 0$, and such that the metric is

$$ds^2 = -f(r)\,dw^2 - 2\epsilon\,dw\,dr + r^2\,d\Omega^2, \tag{3.23}$$

where the parameter

$$\epsilon = \begin{cases} -1 \text{ if } \partial_r \text{ is past-directed,} \\ +1 \text{ if } \partial_r \text{ is future-directed,} \end{cases} \tag{3.24}$$

is a constant indicating whether the shell Σ is ingoing ($\epsilon = -1$) or outgoing ($\epsilon = +1$) towards the future, and the metric function

$$f(r) = \begin{cases} f_-(r), & w < 0, \\ f_+(r), & w > 0, \end{cases} \tag{3.25}$$

is defined piecewise on $M_\pm$. Let

$$n^\mu = \epsilon \, (\partial_r)^\mu \tag{3.26}$$

be a future-directed null vector both normal to and tangential to Σ, let the mass functions $m_\pm(r)$ be defined according to (3.13), and define the *mass jump* $[m(r)]$ by

$$[m(r)] = m_+(r) - m_-(r). \tag{3.27}$$

With this setup, the distributional component of the stress tensor on the shell obtains the simple expression

$$T_\Sigma^{\mu\nu} = \sigma \, n^\mu n^\nu \, \delta(w), \tag{3.28}$$

where

$$\sigma = (-\epsilon) \, \frac{[m(r)]}{4\pi r^2} \, . \tag{3.29}$$

The coefficient σ may be thought of as the surface energy density of the shell, up to an arbitrary normalization factor associated with the null vector n^a. The sign of σ is physically meaningful: timelike observers measure a positive energy density at the shell if and only if $\sigma > 0$. It is therefore sensible to say that shells with $\sigma < 0$ have *negative mass*, while shells with $\sigma > 0$ have *positive mass*. The

sign of σ is a local property, and in principle (in physically unusual cases) a single shell may have positive and negative mass at different points.

Energy conditions. The shell stress tensor (3.28) is easily analyzed in terms of the energy conditions (3.18) above. For an arbitrary causal vector u^a such that $u_a u^a \leq 0$,

$$\begin{aligned} T_{\mu\nu}u^\mu u^\nu &= \sigma\,(-n_\nu u^\nu)^2\,\delta(w), \\ -T^\mu{}_\nu u^\nu &= \sigma\,(-n_\nu u^\nu)\,n^\mu\,\delta(w). \end{aligned} \tag{3.30}$$

Thus the WEC and NEC are violated if and only if $\sigma < 0$. Since the flux vector $F^\mu = -T^\mu{}_\nu u^\nu$ is always null, the FEC is not particularly meaningful in this context. It is worth noting, however, that if u^μ is future-directed (implying $n_\mu u^\mu \leq 0$), then F^μ is future-directed if and only if $\sigma > 0$. These considerations support the above notion that $\sigma > 0$ corresponds to normal matter, while $\sigma < 0$ corresponds to exotic matter.

3.12.3 Energy Conservation and DTR

Local energy conservation, of the form $\nabla_\mu T^{\mu\nu} = 0$, is automatically guaranteed at points where the metric is smooth, and along properly matched shell junctions [93]. At points where shells collide, for example at Hawking radiation nucleation points in the above model, energy conservation must be independently verified by checking an equality called the DTR (Dray-'t Hooft-Redmount) relation [93]. In case of two radial null shells colliding at radius r_0, separating spacetime into four regions (each of the form (3.12)) labeled A, C, B, D clockwise from noon (see Fig. 3.8), the DTR relation reads [1]

$$f_A(r_0)f_B(r_0) - f_C(r_0)f_D(r_0) = 0. \tag{3.31}$$

To quantify violations of energy conservation, we therefore define the *DTR violation function*

$$\chi_{\text{DTR}} = |f_A(r_0)f_B(r_0) - f_C(r_0)f_D(r_0)|, \tag{3.32}$$

so that energy conservation is equivalent to $\chi_{\text{DTR}} = 0$.

Applied to the Hawking radiation nucleation points, at which $f_B(r) = f_C(r) = f_D(r)$, this yields

$$\chi_{\text{DTR}} = |f_A(r_0) - f_B(r_0)|\,|f_B(r_0)|. \tag{3.33}$$

Assuming that the shells carry a finite amount of mass, and that the nucleation radius r_0 is a finite radial distance l_{ev} outside the horizon where $f_B(r) = 0$, it follows that both terms above are finite, so

$$\chi_{\text{DTR}} > 0, \tag{3.34}$$

and energy conservation is violated at nucleation points.

Although the DTR relation is not satisfied at the Hawking radiation nucleation points, the violation is arbitrarily small in the physically relevant limits of the model. In particular, in the limit $l_{\text{ev}} \to 0$ in which nucleation points approach the horizon radius, the factor $|f_B(r_0)| \to 0$ while the other remains finite, so that

$$\chi_{\text{DTR}} \to 0. \tag{3.35}$$

Physically, it is likely that this limit should be taken only down to the Planck scale, so that $l_{\text{ev}} \approx l_{\text{pl}}$, in which case one would interpret the violation of energy conservation to represent a small quantum fluctuation. Since energy conservation is restored in the physically relevant limits of the model, the model remains a

useful approximation to physically realistic spacetimes.

References

[1] J. C. Schindler and A. Aguirre. Algorithms for the explicit computation of Penrose diagrams. *Class. Quant. Grav.*, 35(10):105019, 2018, 1802.02263.

[2] Joseph C. Schindler, Anthony Aguirre, and Amita Kuttner. Understanding black hole evaporation using explicitly computed Penrose diagrams. 2019, 1907.04879.

[3] B. P. Abbott et al. Observation of Gravitational Waves from a Binary Black Hole Merger. *Phys. Rev. Lett.*, 116(6):061102, 2016, 1602.03837.

[4] Kazunori Akiyama et al. First M87 Event Horizon Telescope Results. I. The Shadow of the Supermassive Black Hole. *Astrophys. J.*, 875(1):L1, 2019, 1906.11238.

[5] S. W. Hawking. Black hole explosions. *Nature*, 248:30–31, 1974.

[6] R. Penrose. Republication of: Conformal treatment of infinity. *General Relativity and Gravitation*, 43:901–922, March 2011.

[7] R. Penrose. Zero rest-mass fields including gravitation: Asymptotic behaviour. *Proceedings of the Royal Society of London A: Mathematical, Physical and Engineering Sciences*, 284(1397):159–203, 1965, http://rspa.royalsocietypublishing.org/content/284/1397/159.full.pdf.

[8] Brandon Carter. Complete analytic extension of the symmetry axis of kerr's solution of einstein's equations. *Phys. Rev.*, 141:1242–1247, Jan 1966.

[9] Martin Walker. Block Diagrams and the Extension of Timelike Two-Surfaces. *Journal of Mathematical Physics*, 11(8):2280–2286, 1970.

[10] S. W. Hawking and G. F. R. Ellis. *The Large Scale Structure of Space-Time (Cambridge Monographs on Mathematical Physics)*. Cambridge University Press, 1973.

[11] Andrew J.S. Hamilton. *General Relativity, Black Holes, and Cosmology*. Unpublished. Online at `http://jila.colorado.edu/~ajsh/courses/astr3740_17/texts.html`.

[12] Jerry B Griffiths and Jiří Podolskỳ. *Exact space-times in Einstein's general relativity*. Cambridge University Press, 2009.

[13] Sean A. Hayward. Formation and evaporation of nonsingular black holes. *Phys. Rev. Lett.*, 96:031103, Jan 2006.

[14] R. Geroch, E. H. Kronheimer, and R. Penrose. Ideal points in space-time. *Proceedings of the Royal Society of London A: Mathematical, Physical and Engineering Sciences*, 327(1571):545–567, 1972, http://rspa.royalsocietypublishing.org/content/327/1571/545.full.pdf.

[15] Piotr T. Chrusciel, Christa R. Olz, and Sebastian J. Szybka. Space-time diagrammatics. *Phys. Rev.*, D86:124041, 2012, 1211.1718.

[16] John C. Graves and Dieter R. Brill. Oscillatory character of reissner-nordström metric for an ideal charged wormhole. *Phys. Rev.*, 120:1507–1513, Nov 1960.

[17] Robert M. Wald. The thermodynamics of black holes. *Living Reviews in Relativity*, 4(1):6, 2001.

[18] Jose M. M. Senovilla. Trapped surfaces. *Int. J. Mod. Phys.*, D20:2139, 2011, 1107.1344.

[19] Ingemar Bengtsson and Jose M. M. Senovilla. The Region with trapped surfaces in spherical symmetry, its core, and their boundaries. *Phys. Rev.*, D83:044012, 2011, 1009.0225.

[20] C. Barrabès and W. Israel. Thin shells in general relativity and cosmology: The lightlike limit. *Phys. Rev. D*, 43:1129–1142, Feb 1991.

[21] Tevian Dray and Gerard 't Hooft. The effect of spherical shells of matter on the schwarzschild black hole. *Communications in Mathematical Physics*, 99(4):613–625, Dec 1985.

[22] Ian H. Redmount. Blue-sheet instability of schwarzschild wormholes. *Progress of Theoretical Physics*, 73(6):1401, 1985.

[23] C. Barrabès and P. A. Hogan. *Singular Null Hypersurfaces in General Relativity: Light-Like Signals from Violent Astrophysical Events*. World Scientific Publishing Co, 2003.

[24] M. D. Kruskal. Maximal extension of schwarzschild metric. *Phys. Rev.*, 119:1743–1745, Sep 1960.

[25] Dieter R Brill and Sean A Hayward. Global structure of a black hole cosmos and its extremes. *Classical and Quantum Gravity*, 11(2):359, 1994.

[26] Robert M Wald. *General relativity*. Chicago Univ. Press, Chicago, IL, 1984.

[27] Walter Thirring. *A Course in Mathematical Physics 1 and 2: Classical Dynamical Systems and Classical Field Theory*. Springer, 1992.

[28] Bernard F. Schutz. *Geometrical Methods of Mathematical Physics*. Cambridge University Press, 1980.

[29] Deane Montgomery and Hans Samelson. Transformation groups of spheres. *Annals of Mathematics*, 44(3):454–470, 1943.

[30] Brian C. Hall. *Lie Groups, Lie Algebras, and Representations: An Elementary Introduction (1st Ed.)*. Springer, first edition, 2003.

[31] Sean Carroll. *Spacetime and Geometry: An Introduction to General Relativity*. Pearson, 2003.

[32] S. Weinberg. *Gravitation and Cosmology: Principles and Applications of the General Theory of Relativity*. July 1972.

[33] S. Bonanos. Capabilities of the Mathematica Package 'Riemannian Geometry and Tensor Calculus'. In K. D. Kokkotas and N. Stergioulas, editors, *Recent Developments in Gravity*, pages 174–182, 2003.

[34] Prado Martín-Moruno and Matt Visser. Semiclassical energy conditions for quantum vacuum states. *Journal of High Energy Physics*, 2013(9):50, 2013.

[35] Barrett O'Neill. *Semi-Riemannian Geometry With Applications to Relativity*. Academic Press, 1983.

[36] S. W. Hawking. Particle Creation by Black Holes. *Commun. Math. Phys.*, 43:199–220, 1975. [,167(1975)].

[37] S. W. Hawking. Breakdown of Predictability in Gravitational Collapse. *Phys. Rev.*, D14:2460–2473, 1976.

[38] J. B. Hartle and S. W. Hawking. Path Integral Derivation of Black Hole Radiance. *Phys. Rev.*, D13:2188–2203, 1976.

[39] P. C. W. Davies, S. A. Fulling, and W. G. Unruh. Energy Momentum Tensor Near an Evaporating Black Hole. *Phys. Rev.*, D13:2720–2723, 1976.

[40] William A. Hiscock. Models of Evaporating Black Holes. *Phys. Rev.*, D23:2813, 1981.

[41] W. A. Hiscock. Models of Evaporating Black Holes. II. Effects of the Outgoing Created Radiation. *Phys. Rev.*, D23:2823–2827, 1981.

[42] Sean A. Hayward. Formation and evaporation of regular black holes. *Phys. Rev. Lett.*, 96:031103, 2006, gr-qc/0506126.

[43] Carlo Rovelli and Francesca Vidotto. Planck stars. *Int. J. Mod. Phys.*, D23(12):1442026, 2014, 1401.6562.

[44] Hal M. Haggard and Carlo Rovelli. Quantum-gravity effects outside the horizon spark black to white hole tunneling. *Phys. Rev.*, D92(10):104020, 2015, 1407.0989.

[45] Eric Poisson and W. Israel. Inner-horizon instability and mass inflation in black holes. *Phys. Rev. Lett.*, 63:1663–1666, 1989.

[46] Pierre Martin-Dussaud and Carlo Rovelli. Evaporating black-to-white hole. 2019, 1905.07251.

[47] Leonard Susskind, Larus Thorlacius, and John Uglum. The Stretched horizon and black hole complementarity. *Phys. Rev.*, D48:3743–3761, 1993, hep-th/9306069.

[48] Ahmed Almheiri, Donald Marolf, Joseph Polchinski, and James Sully. Black Holes: Complementarity or Firewalls? *JHEP*, 02:062, 2013, 1207.3123.

[49] Ingemar Bengtsson and Jose M. M. Senovilla. The Region with trapped surfaces in spherical symmetry, its core, and their boundaries. *Phys. Rev.*, D83:044012, 2011, 1009.0225.

[50] Robert P. Geroch. The domain of dependence. *J. Math. Phys.*, 11:437–439, 1970.

[51] N. D. Birrell and P. C. W. Davies. *Quantum Fields in Curved Space*. Cambridge Monographs on Mathematical Physics. Cambridge Univ. Press, Cambridge, UK, 1984.

[52] Abhay Ashtekar and Martin Bojowald. Black hole evaporation: A Paradigm. *Class. Quant. Grav.*, 22:3349–3362, 2005, gr-qc/0504029.

[53] Gary Horowitz, Albion Lawrence, and Eva Silverstein. Insightful D-branes. *JHEP*, 07:057, 2009, 0904.3922.

[54] Sabine Hossenfelder and Lee Smolin. Conservative solutions to the black hole information problem. *Phys. Rev.*, D81:064009, 2010, 0901.3156.

[55] Sabine Hossenfelder, Leonardo Modesto, and Isabeau Premont-Schwarz. A Model for non-singular black hole collapse and evaporation. *Phys. Rev.*, D81:044036, 2010, 0912.1823.

[56] Anthony Aguirre, Sean M. Carroll, and Matthew C. Johnson. Out of equilibrium: understanding cosmological evolution to lower-entropy states. *JCAP*, 1202:024, 2012, 1108.0417.

[57] Christopher R. Stephens, Gerard 't Hooft, and Bernard F. Whiting. Black hole evaporation without information loss. *Class. Quant. Grav.*, 11:621–648, 1994, gr-qc/9310006.

[58] Yasunori Nomura, Jaime Varela, and Sean J. Weinberg. Black Holes, Information, and Hilbert Space for Quantum Gravity. *Phys. Rev.*, D87:084050, 2013, 1210.6348.

[59] Daniele Malafarina. Classical collapse to black holes and quantum bounces: A review. *Universe*, 3(2):48, 2017, 1703.04138.

[60] S. W. Hawking and G. F. R. Ellis. *The Large Scale Structure of Space-Time*. Cambridge Monographs on Mathematical Physics. Cambridge University Press, 2011.

[61] Prado Martin-Moruno and Matt Visser. Classical and semi-classical energy conditions. *Fundam. Theor. Phys.*, 189:193–213, 2017, 1702.05915.

[62] Tommaso De Lorenzo, Costantino Pacilio, Carlo Rovelli, and Simone Speziale. On the Effective Metric of a Planck Star. *Gen. Rel. Grav.*, 47(4):41, 2015, 1412.6015.

[63] Brandon Carter. Complete Analytic Extension of the Symmetry Axis of Kerr's Solution of Einstein's Equations. *Phys. Rev.*, 141:1242–1247, 1966.

[64] B. Carter. The complete analytic extension of the reissner-nordström metric in the special case e2 = m2. *Physics Letters*, 21(4):423 – 424, 1966.

[65] M. D. Kruskal. Maximal extension of Schwarzschild metric. *Phys. Rev.*, 119:1743–1745, 1960.

[66] R. Penrose. Conformal treatment of infinity. *Gen. Rel. Grav.*, 43:901–922, 2011. [,565(1964)].

[67] R. Penrose. Zero rest mass fields including gravitation: Asymptotic behavior. *Proc. Roy. Soc. Lond.*, A284:159, 1965.

[68] Piotr T. Chrusciel, Christa R. Olz, and Sebastian J. Szybka. Space-time diagrammatics. *Phys. Rev.*, D86:124041, 2012, 1211.1718.

[69] Don N. Page. Particle Emission Rates from a Black Hole: Massless Particles from an Uncharged, Nonrotating Hole. *Phys. Rev.*, D13:198–206, 1976.

[70] S. W. Hawking. Information Preservation and Weather Forecasting for Black Holes. 2014, 1401.5761.

[71] Raphael Bousso. A Covariant entropy conjecture. *JHEP*, 07:004, 1999, hep-th/9905177.

[72] Yasuhito Kaminaga. A Dynamical Model of an Evaporating Charged Black Hole and Quantum Instability of Cauchy Horizons. *Class. Quant. Grav.*, 7:1135–1162, 1990.

[73] Maulik K. Parikh and Frank Wilczek. Global structure of evaporating black holes. *Phys. Lett.*, B449:24–29, 1999, gr-qc/9807031.

[74] Alexander Burinskii, Emilio Elizalde, Sergi R. Hildebrandt, and Giulio Magli. Regular sources of the Kerr-Schild class for rotating and nonrotating black hole solutions. *Phys. Rev.*, D65:064039, 2002, gr-qc/0109085.

[75] Hikaru Kawai, Yoshinori Matsuo, and Yuki Yokokura. A Self-consistent Model of the Black Hole Evaporation. *Int. J. Mod. Phys.*, A28:1350050, 2013, 1302.4733.

[76] Hikaru Kawai and Yuki Yokokura. A Model of Black Hole Evaporation and 4D Weyl Anomaly. *Universe*, 3(2):51, 2017, 1701.03455.

[77] Pisin Chen, William G. Unruh, Chih-Hung Wu, and Dong-Han Yeom. Pre-Hawking radiation cannot prevent the formation of apparent horizon. *Phys. Rev.*, D97(6):064045, 2018, 1710.01533.

[78] Valeri P. Frolov and Andrei Zelnikov. Quantum radiation from a sandwich black hole. *Phys. Rev.*, D95(4):044042, 2017, 1612.05319.

[79] Valeri P. Frolov and Andrei Zelnikov. Quantum radiation from an evaporating nonsingular black hole. *Phys. Rev.*, D95(12):124028, 2017, 1704.03043.

[80] Andrew J. S. Hamilton and Pedro P. Avelino. The Physics of the relativistic counter-streaming instability that drives mass inflation inside black holes. *Phys. Rept.*, 495:1–32, 2010, 0811.1926.

[81] Eric Poisson and W. Israel. Internal structure of black holes. *Phys. Rev.*, D41:1796–1809, 1990.

[82] Raúl Carballo-Rubio, Francesco Di Filippo, Stefano Liberati, Costantino Pacilio, and Matt Visser. On the viability of regular black holes. *JHEP*, 07:023, 2018, 1805.02675. [JHEP18,023(2020)].

[83] B. Rosenstein and M. Usher. Explicit illustration of causality violation: Non-causal relativistic wave-packet evolution. *Phys. Rev. D*, 36:2381–2384, Oct 1987.

[84] Ian H. Redmount and Wai-Mo Suen. Path integration in relativistic quantum mechanics. *Int. J. Mod. Phys.*, A8:1629–1636, 1993, gr-qc/9210019.

[85] P. Candelas and D. Deutsch. On the vacuum stress induced by uniform acceleration or supporting the ether. *Proc. Roy. Soc. Lond.*, A354:79–99, 1977.

[86] W. G. Unruh. Notes on black hole evaporation. *Phys. Rev.*, D14:870, 1976.

[87] G. W. Gibbons and S. W. Hawking. Cosmological Event Horizons, Thermodynamics, and Particle Creation. *Phys. Rev.*, D15:2738–2751, 1977.

[88] T. Padmanabhan and T. P. Singh. Response of an Accelerated Detector Coupled to the Stress - Energy Tensor. *Class. Quant. Grav.*, 4:1397–1407, 1987.

[89] P. C. W. Davies. Quantum vacuum friction. *J. Opt. B*, 7:S40–S46, 2005.

[90] A. Manjavacas and F. J. García de Abajo. Thermal and vacuum friction acting on rotating particles. *Phys. Rev. A*, 82:063827, Dec 2010.

[91] Maulik K. Parikh and Frank Wilczek. Hawking radiation as tunneling. *Phys. Rev. Lett.*, 85:5042–5045, 2000, hep-th/9907001.

[92] Jose M. M. Senovilla. Trapped surfaces. *Int. J. Mod. Phys.*, D20:2139, 2011, 1107.1344.

[93] C. Barrabes and W. Israel. Thin shells in general relativity and cosmology: The Lightlike limit. *Phys. Rev.*, D43:1129–1142, 1991.